國立中山大學材料與光電科學學系

博士論文

多種二元金屬玻璃之結構相變與週期變形機制之原子模擬研究

Atomic Simulations on Phase Transformation and Cyclic Deformation Mechanisms in Various Binary Metallic Glasses

研究生：羅友杰 撰

指導教授：黃志青 博士

中華民國 九十八 年 七 月

國立中山大學研究生學位論文審定書

本校材料與光電科學學系博士班

研究生羅友杰（學號：D943060014）所提論文

多種二元金屬玻璃之結構相變與週期變形機制之原子模擬研究
Atomic Simulations on Phase Transformation and Cyclic Deformation Mechanisms in Various Binary Metallic Glasses

經本委員會審查並舉行口試，符合博士學位論文標準。

學位考試委員簽章：

高伯威　　謝克昌

陳正隆　　王雲哲

黃志青

指導教授　黃志青

系主任/所長　謝克昌

致謝

十年寒窗無人問，是古今讀書人共有的心路歷程，這六年來從碩士到博士研究結束，真是相當漫長的路。首先感謝這四年來擔任我研究指導者角色的黃志青教授，老師是一位專業學術涵養豐富、知識廣博，待人處事的手腕與身段都相當令人推崇也讓人折服的傑出學者。我要深深感謝您在我研究遇到瓶頸，有時脾氣暴躁甚至在想法上跟您有所衝突時，您的耐心跟愛始終看照著我，四年來真是辛苦您了。同時感謝本所謝克昌教授、高伯威教授、化學系陳正隆教授、成大土木王雲哲教授，當任學生口試委員時，仔細聆聽並用心給予學生許多寶貴建議，讓學生的論文得以充實完整，成就一本有參考價值的學術論文，因此在此對老師們致上最高謝意。

接著感謝碩士班的指導者朱訓鵬教授，朱老師是中山機械系令人讚賞，學術期刊量史無前例的豐盛，人際關係廣闊，拼勁充滿的年輕老師，是常人所不能及的。感謝您在我念博士班期間，不吝借我使用那些貴重的計算電腦叢集，讓需要沈重計算負擔的工作能順利完成。同時要感謝朱老師研究室一直以來的同學及歷任學弟妹，你們對我的關懷與體貼是很大的幫助。這些人有王中鼎博士、李文頡博士、張鈞奕博士、猛雄、勝輝、阿禾、阿耀、阿娟、文賢、暐霖、泓翔、小欽、幸蓉、家紘、鼎威、根凰。我真的很開心與你們一起渡過這些日子。

黃老師的研究團隊是相當優秀的，這些人有洪子祥博士、張志溢博士、賴炎暉博士與陳海明博士、周鴻昇以及名哲跟浩然，相當感謝你們四年來不斷的參與討論跟合作。研究室未來棟梁的碩陽、柚子、哲男、大豪、阿官、顗任、逸志、捲捲跟婷婷，你們都是我親愛的學弟妹，你們是研究室的未來。感謝鄭宇庭博士，跟你一起合作相處的日子，一起參加英文辯論比賽，真是開心。張育誠博士，我要特別感謝你，沒有你一路的幫忙跟支持，我恐怕早就被迫出局了！李敬仁博士，在最後一年，你回到實驗室來，使整個

研究團隊越發完整。2009 世運期間，因為有你，所以我們可以一起去看開幕去看球賽，共享高雄人的光榮與驕傲。

另外，這四年來有不少老師陸陸續續在適當的時候給我幫忙。我要感謝遠在美國的廖凱輝教授、聶台岡教授、Morris 教授、李莫教授以及李巨教授，感謝老師們不吝指導我研究上的知識與觀念，我很感謝！陳維仁博士、黃爾文博士、莊志彬博士都曾參與過討論，並給予相當寶貴的建議！開物老師一家人，小杰、馨慧、小玲也給我許多美好的回憶與照顧，感謝你們。最後是 D.Frenkel 和 B.Smit 教授，若是沒有你們合著的那本書，我肯定半途放棄，屍沈無涯學海了。

最後要感謝身邊一直關心我的好友跟親人。台南成大的楊安政學長，我對你的感激，你知道的。吳清吉學長和煜聰、伯父、伯母，你們是我在南部的家人，我愛你們！施依姿，我感謝人生有你這樣的朋友。行政大樓第一美女史麗伶大姐，感謝您這六年來的關懷與照顧。渚晴暉老師、楊天祥老師、陳國聲老師、陳碧燕老師、楊建民老師，感謝你們在大學時期教授我治學及人生觀念、是我生命的燈塔與警鐘，我愛你們！李若彤（靜怡），人生中能有妳為良師益友是一種幸福。李大哥、邱婉筑（瑞柳）夫婦、李典蓉、李尚儒，是我在高雄的家人，我愛你們！深深感謝我的奶奶 羅江碧雲女士、父親 羅嘉仁先生、母親 蔡月鳳女士、以及所有親人，你們是我最大的依靠！最後，有許多許多好朋友來不及提了，也謝不完。所以我要感謝主！也感謝有你們一路相伴。在博士班最後一年，我親愛的叔叔 羅嘉賢先生，同時也是我乾爹，他在今年四月因病早逝，回想過去他對我的關愛，我沒有報答的機會，僅以這本論文紀念他對我的支持，一位奉公守法的台中市政府公務員。

羅友杰 謹誌
於中山大學材料與光電科學學系
中華民國九十八年七月

Content

List of Tables

List of Figures

Abstract

The bulk metallic glasses (BMGs) are potential metallic materials due to their interesting properties, such as the high strength, high elastic strain limit, and high wear/corrosion resistance. Over the past four decades, a variety of studies have been done on the characteristics of the mechanical, thermodynamic properties of such category of metallic materials, but there still remain many questions about basic deformation mechanisms and their microstructures so far. Molecular dynamics (MD) simulation can provide significant insight into material properties under the atomic level and see a detailed picture of the model under available investigation in explaining the connection of macroscopic properties to atomic scale. MD simulation is applied to study the material properties and the deformation mechanisms in various binary metallic glasses and intended to examine the feasibility of MD simulation to compare the experimental results obtained in our laboratory over the past few years.

The gradual vitrification evolution of atom mixing and local atomic pairing structure of the binary Zr-Ni, Zr-Ti alloys and pure Zr element during severe deformation at room temperature is traced numerically by molecular dynamic simulation. It is found that the icosahedra clusters will gradually develop with the increasing of disorder environment of alloys in the Zr-Ni, Zr-Ti systems, forming amorphous atomic packing. Other compound-like transition structures were also observed in transient in the Zr-Ni couple during the solid-state amorphization process under severe plastic deformation. The crystalline pure Zr can be vitrified in the simulation provided that the rolling speed is high enough and the rolling temperature is maintained at around 300 K.

On the other hand, the effective medium theory (EMT) inter-atomic potential is

employed in the molecular dynamics (MD) simulation to challenge the study of the diffusion properties in the Mg-Cu thin films. The transition of local structures of Mg-Cu thin films is traced at annealing temperatures of 300, 413, and 500 K. Furthermore, the simulation results are compared with the experimental results obtained from the transmission electron microscopy and X-ray diffraction. The gradual evolution of the local atomic pairing and cluster structure is discussed in light of the Mg and Cu atomic characteristics.

Lately, the progress of the cyclic-fatigue damage in a binary Zr-Cu metallic glass in small size scale is investigated using classical molecular-dynamics (MD) simulations. The three-dimensional Zr-Cu fully amorphous structure is produced by quenching at a cooling rate 5 K/ps (ps = 10^{-12} s) from a high liquid temperature. The Nose-Hoover chain method is used to control the temperature and pressure to maintain a reasonable thermodynamic state during the MD-simulation process, as well as to bring the imposed cyclic stress on the subsequent simulation process. Both the stress- and strain-control cyclic loadings are applied to investigate the structural response and free-volume evolution. The overall structure would consistently maintain the amorphous state during cyclic loading. The plastic deformation in simulated samples proceeds via the network-like development of individual shear transition zones (STZs) by the reversible and irreversible structure-relaxations during cyclic loading, dislike the contribution of shear band in large-scale specimens. Dynamic recovery and reversible/irreversible structure rearrangements occur in the current model, along with annihilation of excessive free volumes. This behavior might be able to retard the damage growth of metallic glass and enhance their fatigue life.

中文摘要

金屬玻璃具有高強度、高彈性應變極限、甚好的抗腐蝕能力等特殊性質，因此被視為是具有應用潛力的金屬材料。過去四十年來，已經有許多的學習專注在這一類金屬玻璃的機械性質、熱力學性質上面，但仍然有許多關於基本的變形機制與微結構的問題尚未釐清。分子動力學可以為原子尺度的材料性質提供一個明顯的洞悉力，亦即提供我們一個原子結構細節的圖像去瞭解材料的微觀性質。分子動力學在此論文被用來學習多種二元金屬玻璃合金的材料性質與變形機制，並且試圖去探討將它與本研究室的實驗結果相互印證的可能性。

本研究的第一部份是用分子動力學來模擬鋯鎳、鋯鈦等二元合金、以及純鋯元素在室溫下以應力誘導方式使其逐漸玻璃化過程中，其原子混和與局部結構的轉變機制。研究發現二十面體的原子團簇會伴隨著鋯鎳、鋯鈦合金系統內的無序環境增加而逐漸發展，形成非晶型的原子堆積。同時也觀察到當施予劇烈塑性變形而發生固態非晶化過程時，在鋯鎳系統中出現疑似介金屬化合物的過渡結構。模擬結果亦顯示，當滾壓速度夠快同時環境溫度被控制在 300 K 左右時，結晶的純鋯元素理論上可以被非晶化。

研究的第二部份，採用等效介質理論所發展的鎂銅勢能函數去學習鎂銅薄膜介面間的擴散性質。在 300、413 以及 500 K 等不同溫度探討鎂銅薄膜介面的局部結構轉變，並將模擬結果與電子顯微鏡、X-Ray 繞射的實驗結果作比對。依照鎂銅原子特性來討論局部原子配對與團簇結構的演變行為。

最後一個部分是以分子動力學研究二元鋯銅金屬玻璃在小空間尺度下的週期性疲勞損壞的過程，藉由適當的冷凝速率 5K/ps 由高溫急速冷卻至室溫以產生一個三維空間的鋯銅金屬玻璃模型。並採用 Nose-Hoover chain 方法來控制模擬時系統的溫度、壓力，

使其維持在合理的熱力學狀態，並用來控制週期變形時系統應力狀態。同時使用應力控制、應變控制兩種模式來學習結構反應行為與自由體積的演變。研究結果顯示，在週期變形的過程中，結構始終被維持在非晶態。塑性變形的發展乃是藉由可逆與不可逆結構鬆弛行為，由個別的剪變形區帶（shear transition zone）開始逐漸形成網狀連結發展所貢獻，與在大空間尺度下是由剪帶（shear band）所貢獻而成的機制有所不同。動態回復與可逆/不可逆的結構重組行為不斷發生在本模型中，同時伴隨著多餘自由體積的消除。這個行為也許能夠阻止金屬玻璃的疲勞損害並增加他們的疲勞週期。

Chapter 1 Introduction and motivation

1-1 Introduction

The development of metallic industry always plays a very important role in the history of human beings. Most of the metallic elements exiting in the nature are present with crystalline structures which are the most stable structures with the lowest energy state, but sometimes they can be made by various ways into metastable amorphous solid forms, such as rapid quenching techniques [1-5], mechanical alloying [6-10], accumulative roll bonding [11-16], and vapor condensation [17]. The characteristics of the mechanical, thermodynamic properties of such category of metallic materials are very similar to ceramic glasses, and thus they are also called as metallic glasses.

Over the past four decades, a considerable number of studies have been done on the BMGs due to their high yield strength, relatively high fracture toughness, low internal friction, as well as better wear and corrosion resistance [18-20]. Although bulk metallic glasses (BMGs) are one of such species of materials which are considered to be high potential for the industrial applications, the insufficient plastic deformation at room temperature is still the Achilles' hell for the industrial applications regardless of its highly scientific worth.

In general, metallic glasses (MGs) are disordered materials which lack the periodicity of long range ordering in the atom packing, but the atomic arrangement in amorphous alloys is not completely random as liquid. In fact, many scholars believe that amorphous structures are composed of short range ordering, such as icosahedra clusters or other packing forms related to the intermetallic compounds that would form in the corresponding equilibrium phase diagram [21, 22]. The short range order is identified as a structure consists of an atom and its nearest neighbors perhaps two or three atom distance. Recently, it has also been focused more attention on the study of medium range order, which is viewed as a new ordering range between short range order and long range order in the amorphous structure [23]. When an amorphous structure is achieved by quenching, it may be composed of icosahedral local short-range ordering, network-forming clusters medium-range ordering, and other unidentified-random local structures [23, 24], that is, a complex association in their topology. How to build the atomic structural model in BMGs and how to fill three dimension spaces with these local structural units are still important problems although only limited research has been reported so far.

Due to the difference in the structural systems between metallic glasses and crystalline alloys, it has an unusual performance on the mechanical properties [25-28]. For example, most metallic glasses exhibit evident brittle behavior under a uniaxial tensile test, but sometimes give very limited plastic behavior before failure by means of shear-band propagation. Also, BMGs can perform a large global plasticity through the generation of multiple shear bands during unconfined or confined compression test. Activities of shear band are viewed as the main factor on the plastic deformation of BMGs.

Despite a wealth of investigations, many questions about shear bands and their microstructures are still unclear so far. For instance, how does a shear band initiate in the MG and develop mature shear band from its embryo, how do shear bands interact with each other, and how would the shear band develop in a composite surroundings such as interactions with embedding crystals? These issues not only depend on the effect of temperature but are also related to the strain rate and other else. The width of a typical shear band is around 10^1-10^2

nm, and the size scale used to define the structures of metallic glasses is within 1-3 nm.

The studies in the microstructures of metallic glasses in this shortest length scale by electron-microscopy such as X-Ray, scanning electron microscope (SEM) or Transmission electron microscopy (TEM) are usually excellent and interesting, but they are relatively less in the theoretic models either in the statistic or continuum simulation computing than those in experiments. Through the studies of simulation methods to compare with experimental data, such as electron scattering data and pair distribution functions, it is expected to be able to investigate the shear-band mechanisms and the microstructures of BMGs in depth. Also, a completely theoretic model could be built up due to the combination of computing model and experiments, not only to explain the current experimental phenomena but also to predict the probative behavior in the future.

Molecular dynamics (MD) simulation is one of important simulation methods provided significant insight into material properties under the atomic level. The major advantage of MD simulations is to see a detailed picture of the model under available investigation, and so they have been very instrumental in explaining the connection of macroscopic properties to atomic scale [29]. For instances, MD simulation has been carried out successfully in the studies of various metallic systems such as point defect movement [30], dislocation mechanisms [31, 32], and grain-boundary structures in polycrystalline materials [33-36] in recent years. However, a number of limitations in the simulations will also be confronted, while simulations are treated as key insights in the study.

Generally, there are three limitations in the current MD simulation, namely the availability of MD potential, time-scale limitations, and the limit on the system size. Two of the later can be alleviated in the promotion of computer efficiency and by adding the parallelization techniques in program, but the former is still challenged on the accuracy of material specificity and on the development for the multicomponent system, especially for the BMGs. In this thesis, the MD simulation is applied to study the material properties and the deformation mechanisms in various binary metallic glasses. It is intended to examine the feasibility of MD simulation and to compare the experimental results obtained in our laboratory over the past few years. The work is divided into three parts.

1-2 Motivation

In the first part, the MD simulation is adopted to model the phase transition from nanocrystalline to amorphous in the Zr based intermetallic alloys during accumulative roll bonding (ARB) process. The ARB method is one of solid-state vitrification methods which could force the atoms of adopted elements to diffuse in a solid state under low temperatures in order to produce the amorphous materials in bulk form without the limitation of cooling rates.

According to our previous ARB experimental studies at ambient temperature [37-39] of binary Zr based alloys made by ARB, the grain size of the ARB specimen was gradually refined down to ~2 nm, such nanocrystals would disappear in the matrix and form the complete amorphous phase upon subsequent ARB passes. The role played by the short range ordering, such as icosahedra, or other packing forms related to the intermetallic compounds during solid-state vitrification is still not well understood. The motivation of this part is to study the atomic structure evolution of the Zr based binary alloys (Zr-Ni, Zr-Ti), even extending to the pure Zr metal finally, during the repeated ARB strain-and-stack procedure. The gradual evolutions of atom mixing and local atomic crystal structure of the binary alloys are traced numerically by the radial distribution function (RDF) and the Honeycutt-Anderson

(HA) pair analysis technique.

In the second part, the MD simulation is used to challenge the study of the diffusion properties between incoherent interfaces of the binary metallic glasses. In this part of MD study, there is no stress involved, thus excluding the dynamic deformation of materials; only the thermal effect is considered. The multi-layer sputtered Mg-Cu thin film, which is meaningful and interesting to explore the structure transition from the pure Mg and pure Cu crystalline thin layers to the mixed amorphous phase during post-sputtering annealing. A composite multi-layer consisting of hexagonal closed-packed (HCP) structure (Mg atoms), face-centered cubic (FCC) structure (Cu atoms), and amorphous structure (mixed with Mg and Cu) is examined during thermal annealing at a suitable temperature [40, 41].

Finally, in order to explore the feasibility of MD simulation in dynamic deformation of MGs, the progress of the cyclic-fatigue damage in a binary Zr-Cu metallic glass in small size scale is investigated. Compared with the literatures on the study of deformation mechanisms of BMGs under compression or even tension monotonic testing, there remain much fewer reports on the fatigue behavior, especially at the atomic scale. As well known, the concepts of free volume and shear transition zones (STZs) are viewed as the main defects and basic deformation units in the metallic glasses. Free volumes and STZs are also relevant to the fatigue damage mechanism of BMGs. The shear band formation and propagation usually go along with the local increase of free volumes and crack sites within BMGs due to the weakness in the shear bands or shear-off steps [42, 43], subsequently leading a fracture and fatigue damage. It follows that, if we can reduce the free volumes in BMGs, the plastic deformation and fatigue damage might be retarded and the fatigue life might be extended. However, the theoretical model and basic fatigue-damage mechanism in fatigue behavior of BMGs still need further exploration. The aim of the final part on this dissertation is to examine the relationship between the variation of free volume and the basic development of shear deformation events under cyclic loading in small size scale, and to further understand the mechanism of deformation retardation under cyclic-loading process.

The following Chapter 2 discusses some aspects of the background and theory of BMGs such as the development, mechanical properties, plastic deformation mechanisms, fatigue behavior, and structural topology of BMGs. Chapter 3 introduces the fundamental background of MD simulation methods, including the fitting of the interatomic potential and basic concept of ensembles in MD. Chapter 4 describes the theory and simulation model applied in this work. The results of simulation models are presented in Ch. 5 and are further discussed in Chapter 6. Chapter 7 is for the final conclusions.

Chapter 2 Background and Literature Review of metallic glasses

2-1 The development of metallic glasses

In 1960, Klement et al. [44] developed the first metallic glasses of $Au_{75}Si_{25}$ by the rapid quenching techniques for cooling the metallic liquids at very fast rates of 10^5-10^6 K/s. Their works initiate broad interest quickly among the scientists and engineers because they showed the process of nucleation and growth of crystalline phase could be skipped to produce a frozen liquid configuration. A few years later, the ternary amorphous alloys of Pd-Si-X (X = Ag, Cu or Au) were prepared successfully by Chen and Turnbull [45], and the Pd-T-Si (T = Ni, Co or Fe) ternary amorphous alloys which included the magnetic atoms were also presented soon after [46]. The maximum diameter of these metallic glasses was reached to 1 mm by using the die casting and roller-quenching method. The effects of the alloy systems, compositions and the existence of a glass transition was demonstrated, it leaded to the first detailed studies in the formation, structure and property investigations of amorphous alloys. Because of their fundamental sciences and engineering application potential, metallic glasses have attracted great attention.

The geometry of metallic glasses, however, is limited to thin foils or lines as a result of high cooling rate, which are not easy to find the wide application. How to determine the glass forming ability (GFA) of amorphous alloys and increase the diameter of specimens becomes the important topic in that period. Turnbull and Fisher [47]advanced a criterion to predict the glass forming ability of an alloy. According to his criterion, the reduced glass transition temperature T_{rg}, equal to the glass transition temperature T_g over liquids temperature T_l, or $T_{rg} = T_g/T_l$ is the primary factor. If T_g is larger and T_l smaller, the value of T_{rg} will be higher so that such a liquid can be easily undercooled into a glassy state at a lower cooling rate. Although there are several new criteria proposed following them [48, 49], the T_{rg} has been proved to be useful in reflecting the GFA of metallic glasses including BMGs.

In 1974, the rods of Pd-Cu-Si alloy measuring 1-3 mm in diameter, the first bulk metallic glasses were prepared by Chen [46] using simple suction-casting methods. In 1982, Turnbull's group [50, 51] pushed the diameter of critical casting thickness of the Pd-Ni-P alloys up to 10 mm by processing the Pd–Ni–P melt in a boron oxide flux, and eliminate heterogeneous nucleation. A series of solid state amophization techniques that are completely different from the mechanism of rapid quenching had been developed during this time. For example, mechanical alloying, diffusion induced amorphization in multilayers, ion beam mixing, hydrogen absorption, and inverse melting [52]. The thin films or powders of metallic glasses can be acquired as well by interdiffusion and interfacial reaction when the temperature is just below the glass transition temperature.

In the late 1980s, Inoue's group [53, 54]in Tohoku University of Japan developed many new multicomponent metallic glass systems with lower cooling rates in Mg-, Ln-, Zr-, Fe-, Pd-, Cu-, Ti- and Ni- based systems. They found exceptional glass forming ability in La-Al-Ni and La-Al-Cu ternary alloys system [53]. By casting the alloy melt in water-cooling Cu molds, the cylindrical samples with diameters up to 5 mm or sheets with similar thicknesses were made fully glassy in the $La_{55}Al_{25}Ni_{20}$ alloy, and the $La_{55}Al_{25}Ni_{10}Cu_{10}$ alloy was fabricated later with a diameter up to 9 mm by the same method.

In 1990s, the Inoue group further developed a series of multicomponent Zr-based bulk metallic glasses, such as Zr-Cu-Ni, Zr-Cu-Ni-Al, etc., along with Mg-based, e.g. Mg–Cu–Y and Mg–Ni–Y alloys, all exhibiting a high GFA and thermal stability [55-58]. For one of the Zr-based BMGs, $Zr_{65}Al_{7.5}Ni_{10}Cu_{17.5}$, the critical casting thickness was raised up to 15 mm, and the largest critical casting thickness could reach to 72 mm in the Pd–Cu–Ni–P family[59]. The evolution of such category alloys demonstrated that bulk metallic glass composition were not a laboratory curiosity and could be quite interesting and for promising engineering applications. In fact, the Zr-based bulk metallic glasses found application in the industries just three years after it was invented. The typical bulk metallic glasses systems and the reported years are listed in Table 2-1[20]. Subsequently, a set of empirical rules in order to direct the selection of alloying elements and composition of glass forming alloys have been proposed by Inoue and Johnson as follows[19, 60]:

(1) Multicomponent alloys with three or more elements.

(2) More than 12% atomic radius difference among them.

(3) Negative heat of mixing between constituent elements.

(4) The deep eutectic rule based on the T_{rg} criterion.

These rules provide an important role for the synthesizing of BMGs in the last decade.

However, in the subsequent experiments finding some binary alloys such as Ni-Nb[61], Ca-Al [62] Zr-Ni[63, 64], and Cu-Zr [65-67] etc., BMGs can also be obtained with several millimeters and the best glass formers are not fixed on the eutectics of them, indicating that the above mentioned rules are not the necessary concern in all cases for designing BMGs. Formation mechanism and criteria for the binary BMGs may be distinct from the multicomponent systems. These results suggest that there are many potential forming systems of the metallic glasses to be discovered. On the other hand, these kinds of simple binary systems of BMGs are the very ideal model for studying their characteristics of the deformation mechanism and structure by computer simulation and theorizing.

Recently, many scholars attempt to detect the regulations on the glass forming ability from thermodynamic modeling or statistical mechanics that can help to design the larger size of amorphous alloys in general [49, 53]; others focus on the studies of their mechanical properties and structural topology that can build the structural modeling of BMGs as well as improve their strength and ductility. In future, the trends of investigations of BMGs are not only kept on the experimental competition but also extended into complete modeling of fundamental theory.

2-2 Microstructures in metallic glasses

In 1959, a structural model of dense random packing of hard spheres is first suggested by Bernal [68] to be a simple model for metal liquids, and subsequently indicated by Cohen and Turnbull [69] that this simple model can be also applied to describe the metallic glasses. In 1979, Wang [70] supposed that the amorphous metal alloys may be a special class of the glassy state whose short-range structure is random Kasper polyhedral close packing of soft atoms similar to those in the crystalline counterparts. This short-range structure is described based on a new type of glassy structure with a high degree of dense randomly packed atomic configurations. The density measurements show that the density difference is in the range 0.3~1.0% between bulk metallic glasses and fully crystallized state [71, 72]. There is neither splitting of the second peak nor pre-peak at the lower wave vector as seen in the reduced density function curve of the BMGs [71, 73, 74]. These results confirm that the multicomponent BMGs has a homogeneously mixed atomic configuration corresponding to a high dense randomly packing.

One of the most important topological short range structures developed among glasses and supercooled liquids is the local icosahedral clusters, which are revealed by many simulation studies [75-79]. Figure 2-1 (a) shows a typical fragment of an icosahedron, the central atom forms a fivefold symmetry arrangements with each of its 12 neighbors. In contrast as shown in Fig. 2-1 (b) is a regular fragment of an FCC order, and the same pair will become an HCP order if the bottom close-packed plane is shifted as the same as the top plane. This fivefold symmetry and icosahedral clusters is also detected from the experiments of liquids and metallic glasses [80, 81], even though in an immiscible binary system with positive heat of mixing [77-79]. The binding energy of an icosahedral cluster of 13 Lennard-Jones (LJ) atoms is 8.4% lower than an FCC or HCP arrangement [82]. The critical size for a transition from icosahedral cluster to icosahedral phase is about 8 nm [54]. Icosahedral packing is a basic structural unit in extended amorphous systems, and the existence of icosahedral clusters offer seeds for the precipitation of the icosahedral phase. The icosahedral quasicrystalline phase will precipitate in the primary crystallization process and then transforms to stable crystalline phases when the amorphous alloys is annealing at higher temperatures [83-85].

In recent years, an order effect, called the medium range order, existing over length scale larger than the short range order but not extends to the long range order as crystalline state, has been detected in the some amorphous alloys [86-88]. Figure 2-2 shows a typical high-resolution electron microscopy image of the BCC-Fe medium range order with the sizes around 1-3 nm existing in the Fe-Nb-B amorphous matrix [89]. Although the icosahedral type model gives a sound description on the structure in the short range order of metallic glasses but fails beyond the nearest-neighbor shell. For instance, how can the medium range order be defined with the local structural unit, and how would the local structural units be connected to full three-dimensional space?

Miracle [90] suggested a compelling structural model for metallic glasses based on the dense packing of atomic clusters. An FCC packing of overlapping clusters is taken as the building scheme for medium range order in metallic glasses. Figure 2-3 illustrate his promoted model of medium range order. A reality check for these previous structural concepts was proposed by Sheng et al. [23] with experiments and simulations. They indicate the icosahedral ordering of single-solute-centered quasi-equivalent clusters is an efficient packing scheme, but is not the only type of medium range order. The atomic packing configurations of different binary amorphous alloys are shown in Fig. 2-4. For each one of the metallic glasses, the several types of local coordination polyhedra units are geometrically different, and not identical in their topology and coordination number. They can be considered quasi-equivalent, or cluster-like units for a given glass, supporting the framework of cluster packing. The cluster connection diagrams for the several metallic glasses are shown in Fig. 2-5 to illustrate the specific packing and connection schemes of the quasi-equivalent clusters, through the sharing of edges, faces and vertices. This maybe represents the important question of how the clusters are connected and packed to fill the three-dimensional space, giving rise to the medium range order. It is short range for the packing of clusters, but already medium range from the standpoint of atomic correlation beyond one cluster.

A new insight, imperfect ordered packing, which is closely related to the cooling rate, is exposed on the medium range order embedded in the disordered atomic matrix by selected simulation of high-resolution electron microscopy image [91]. It points out that the packing character of medium range ordering structures can be of two types, i.e. icosahedron-like and lattice-like, and indicates that the solidification from melts or crystallization of metallic glasses is controlled by preferential growth of the most stable imperfect ordered packing. On the other hand, Fan et al. [92-94] proposed a structural model for bulk amorphous alloys based on the pair distribution functions measured using neutron scattering and reverse Monte Carlo simulations. Figure 2-6 shows a refined model of bulk amorphous alloys due to the reverse Monte Carlo method that has a good agreement with the experimental measurement. There are many clusters of imperfect icosahedral and cubic forms extracted from Fig. 2-6.

These clusters are randomly distributed, strongly connected, and result in the space between the clusters. The space between the clusters forms free volume, which provides a degree of freedom for the rotation of the clusters under applied load. This cooperative rotation of clusters forms a layer motion (i.e. shear bands), and plastically deforms the amorphous alloys. This model implies that the mechanical properties, e.g. strength and ductility, are dominated by the combination of the bonding characteristics inside and between these clusters.

2-3 Mechanical properties

Unlike the dislocation mechanisms for plastic deformation in crystalline alloys, the amorphous alloys only allow limited atomic displacements to resist deformation as a result of the glassy structure with a high degree of dense randomly packed atomic configurations, when the applied stress is on the amorphous alloys. Figure 2-7 summarizes the relationship between tensile strength, Vickers hardness and Young's modulus for bulk glassy alloys, and the data on crystalline metallic alloys are also included for comparison [54, 95]. As the figure indicates, the BMGs have higher tensile fracture strength, σ_f of 0.8-2.5 GPa, Vickers hardness H_v of 200-600, and lower Young's modulus E of 47-102 GPa, than ordinary metallic crystals [54]. It is considered that the significant difference in the mechanical properties is due to the discrepancy in the deformation and fracture mechanisms between bulk metallic glasses and crystalline alloys.

It has been widely accepted that shear-band propagation is the major cause affecting the ductility and toughness of the amorphous alloys. Plastic deformation in metallic glasses is generally associated with inhomogeneous flow in highly localized shear bands. When the shear band went through in the metallic glasses, it is often accompanied with locally rising high temperature to influence the shear flow. Figure 2-8 (a) is good evidence from tensile experiments to show that local melting occurs under high strain rate situations through unstable fracture [96]. Even under slower loading rates, a veined fracture surface indicates a decrease in the glass viscosity, as shown in Fig. 2-8 (b). Due to the highly localized nature of flow and the lack of microstructural features in the metallic glass to distract the flow, shear band formation typically leads to catastrophic failure. The strain softening and thermal softening mechanisms are tightly associated with the localization of shear band [97].

Generally speaking, the metallic glasses have high fracture toughness but brittle as well as negligible plasticity. For instance, the Zr-based bulk metallic glasses present high Charpy impact fracture energies ranging from 110-140 kJ/m^2 and high fracture toughness limit [98]. Their fatigue limit is close to those of the crystalline alloys. However, standard stress–strain fatigue tests show that the Vitreloy alloy (commercial Zr-based BMG) has an extremely low resistance to crack initiation and a crack propagates rapidly once it has formed. If this alloy does start to yield or fracture, it fails quickly. Geometrical confinement of shear bands can dramatically enhance overall plasticity.

Furthermore, the plastic yield point of most bulk metallic glasses is located within a small range around $\varepsilon_y = 2\%$ at room temperature [99]. Composite approach is used to enhance the ductility and toughness of metallic glasses in recent fabricating efforts[100]. Figure 2-9 (a) shows the scanning electron microscopy (SEM) backscattered electon image of in situ Zr-Ti-Nb-Cu-Ni-Be composite microstructure, and Fig. 2-9 (b) is the compressive stress strain curve for a cylindrical in situ composite specimen. From Fig. 2-9 (a), a variety of reinforcing crystalline phase consisting of a ductile crystalline Ti-Zr-Nb β-phase, with body-centered cubic (BCC) structure, has been formed in the bulk metallic glass matrix. This bulk metallic glass matrix composite successfully increases the plastic strain to over 8% prior to failure, as shown in Fig. 2-9 (b). Later, a plastic strain of 20% is measured in the

Pt-Cu-Ni-P bulk metallic glasses before failure, as seen in Fig. 2-10 (a). Its behavior is like a typical bulk metallic glasses initially but performs as a perfectly plastic deformation after passing the yielding point of 2%. This Pt-Cu-Ni-P bulk metallic glass has a high Poisson ratio of 0.42, which causes the tip of a shear band to extend rather than to initiate a crack. This results in the formation of multiple shear bands in Fig. 2-10 (b), and is the origin of the large ductility [101].

2-4 Deformation mechanisms

Due to the absence of dislocation and grain boundary structures, the plastic deformation mechanism of metallic glasses is well known as shear-band evolution that deeply associates with the mechanical properties and failure behavior in bulk metallic glasses. A SEM observation showing the shear bands is given in Fig. 2-11. Nevertheless, the shear band is not the basic defect unit in the deformation mechanisms in the metallic glasses under microscopic scale. In the 1960s, Cohen and Turnbull [102] as well as Spaepen [103] suggested a concept of free volume which is considered as vacancy-like defect (Fig. 2-12) in the metallic glasses, and Argon [104] proposed a theoretical model of plastic flow in metallic glasses, termed shear transformation zone (STZ), which is the fundamental shear unit consisting of a free volume site and its close adjacent atoms in amorphous metals.

The concept of free volume

In the conceptual framework of free volume, the mechanical coupling is weak to the surrounding of free volumes, and hence the inelastic relaxation becomes possible by local atom rearrangement, without affecting the surroundings significantly [105]. Thus, free volume regions could be the preferred sites where easy caused the glass structure destabilization by either temperature or applied stresses. The concept of free volume is most frequently used in explaining the deformation behaviors and atomic relaxations in the MGs due to its convenient for measurement (density or enthalpy change), and easy understanding, that is, a necessary open space allowed for shear process to operate. For instance, a simple relationship $\nu_f/\nu_m = \beta \cdot \Delta H$ assumes that enthalpy ΔH is proportional to the variation of the average free volume per atom, ν_f/ν_m [106]. Thus, based on the enthalpy recovery measurements, the reduction of free volume difference via structural relaxation, ν_f/ν_m, was determined.

Also, a free volume exhaustion mechanism was proposed by Yang et al. [107] to explain the interesting fact that propagation of shear bands in metallic glasses can be retarded, with decreasing temperature and shear strains, in the lack of work hardening mechanisms. It is generally thought that the shear bands could form as a result of the movement and accumulation of free volumes (dilatation expansion). Atomic simulations also show that the local free volumes increase in the BMG provides an open space for the movements of atoms and is associated with the localization of shear band, and the shear softening results from the production of excessive free volume in the shear band [108-110].

Despite the successful description on the strain softening, heterogeneous deformation of MGs, and various mechanical properties of experimental observations, the validity of the free volume theory is questionable, and its atomic basis is still being challenged by atomic simulations. One can easy find the ambiguous characteristics that the free-volume sites may initiate plastic deformation and also can be the result of plastic deformation simultaneously, but not the deformation process itself [111]. Besides, the free-volume model has not made clear motion and rearrangement of constitute atoms within shear bands during plastic flow. To clearly identify the “free volumes” is almost impossible either in experiments or simulations that results in the barrier on the building complete physic model so far. Generally, the concept of free volume is successful as a phenomenology but not as a microscopic theory [105].

The model of shear transformation zones

Another well-use defect model extended from free-volume assumption used to explaining the plastic deformation of metallic glasses is STZ model proposed by A. Argon. According to their model, shear deformation takes place by spontaneous and cooperative reorganization of a small cluster of randomly close-packed atoms [112]. An STZ can supply a small increment of shear strain under the action of an applied shear stress [113], and thus creates a localized distortion of the surroundings to accomplish the shear-band formation. A simplified picture of STZ deformation is shown in Fig. 2-13. The size of STZ is predicted among the order of 100 atoms from energetic considerations [114, 115] and is consistent with the model of molecular dynamics simulation in the investigation of Cu-Ti system [116].

Compared with abstract image of free-volume concept, the STZ mechanism is easy to be studied in the atomic models. A number of MD simulation studies by Falk and Langer summarized the crucial features of STZ mechanisms as follows [111, 117]: (a) once a STZ has transformed and relieved a certain amount of shear stress, it cannot transform again in the same direction. Thus, the system saturates and becomes jammed. (b) STZs can be created and destroyed at rates proportional to the rate of irreversible plastic deformation, and plastic flow can take place only when new zones are being created as fast as existing zones are being transformed. (c) The attempt frequency of the transition is tied to the noise in the system, which is driven by the strain rate. The stochastic nature of these fluctuations is assumed to arise from random motions associated with the disorder in the system. (d) The transition rates between jammed and flowing are strongly sensitive to the applied stress. Recently, they also proposed a criterion (effective temperature) that determines which materials exhibit shear bands based on the initial conditions alone, based on their STZ theory [118-120].

Figure 2-14 shows the behavior of the effective temperature as a function of time for a system that localizes and a system that does not localize, Figs. 2-14 (a) and (b) illustrating the two different initial stages, respectively [118]. Their numerical works show that perturbations to the effective temperature grow due to an instability in the transient dynamics, but unstable systems do not always develop shear bands. Nonlinear energy dissipation processes interact with perturbation growth to determine whether a material exhibits strain localization [118]. Other simulation studies in the nature of STZ model are keeping on publish [121] and become worthy of investigating this crucial issue in depth.

Theory of shear banding and shear band model

According to the experimental observations, the width of a shear band is 101-102 nm the same as its offset shear displacement [122, 123], and propagation time of shear bands is about 10^{-5} s [124]. Because shear bands are thin, move fast, and are short-lived, to observe the dynamic evolution of the shear bands in the metallic glasses is highly difficult. Building the atomic scale model of shear band such as the development of a shear band inside a binary bulk metallic glass model, in Fig. 2-15, is very beneficial for studying the shear band mechanism [110]. A simple conceptual quantity excess volume, $\nu_{excess} = \nu_{voro} - \nu_{atom}$ (Fig. 2-16) is used to investigate the relation between the free volume changes and shear localization. They suggested that shear banding results from the volume-expansion-induced mechanical softening [109, 110, 125, 126]. A loop of “local volume increase→local shear softening→large local strain→local volume increase” may be the basic mechanism for deformation and shear banding in MGs. Similar results are observed in the shear-band simulation works of the Mg-Cu systems by Bailey et al. [127], the interactions of the shear bands with the free surfaces as well as with each other result in an initial temperature rise, but the rise of temperature are delayed somewhat with respect to the localization of plastic flow itself.

Shimizu et al proposed an aged-rejuvenation-glue-liquid (ARGL) model, Fig. 2-17, of shear band in BMGs [128]. That is a more complete theoretical model of shear band than that of others so far. They proposed that the critical condition of initiating a mature shear band (MSB) is not the nucleation of embryonic shear band (ESB), but its propagation. The ESB is easy forming in the MGs. However, to propagate an ESB, the far-field shear stress must exceed the quasi-steady-state glue traction stress of shear-alienated glass until the glass transition temperature is approached internally due to frictional heating, at which point ESB matures as a runway shear crack [128], as shown in Fig. 2-18. In contrast, when applied stress is below the glue traction, the ESB does not propagate, become diffuse, and eventually die. At the same time, an incubation length scale l_{inc} is necessary for this maturation for the BMGs, below which sample size-sale shear localization does not happen. The incubation length $l_{inc} \sim \alpha c_v^2 (T_g - T_{env})^2 / \tau_{glue}^2 c_s$, where α is the thermal diffusivity, c_v is its volumetric specific heat, T_{env} is initial temperature, is the c_s shear wave speed. Through the calculation of this form, the l_{inc} is about 10 nm for Zr-based BMGs [128, 129].

Furthermore, it is often questioned whether the shear band mechanisms with regard to metallic glasses is similar to the dislocation mechanisms for crystalline structure, although they are of different definitions. Schuh and Lund [113] found that the plasticity in metallic glasses is consistent with the Mohr-Coulomb criterion by the STZ theory as well as molecular simulation works, and predicted a transition from dislocation-dominated yield processes (following the von Mises criterion) to STZ-dominated yield (following the Mohr–Coulomb criterion) as grain size decreases toward zero for nanocrystalline materials. Ogata et al. [130] simulated the nucleation of local shear transformation zone (STZ) and shear band, under volume-conserving simple shear deformation in molecular dynamics. A significant shear–normal stress coupling which suggests the modified Mohr-Coulomb yield criterion has also been demonstrated. They suggested that the dislocation concept may be applicable to bulk metallic glasses with modifications such as taking into account the structural features of bulk metallic glasses instead of the Burgers vector concept in crystals.

The plastic deformation always accompanies the localized heating within shear band that is an important key-point to result in the strain-softening mechanisms and thermal softening on the fracture surface [131]. Understanding the temperature rise in shear bands can also help to improve the ductility and toughness of the metallic glasses. A substantial increase in temperature will correspond with a drop in viscosity governed by the presence of free volume within the metallic glasses [132]. From the calculation of heat conduction theory and STZ modeling, Yang et al. [133] demonstrated that the temperature of shear bands at the fracture strength is strikingly similar to their glass transition temperature for a number of BMG systems. This offered a new guidline for the expansion of ultra-high strength bulk metallic glasses from their glass transition temperature, density, and heat capacity values. The calculated shear-band temperatures at the fracture strength for nine bulk metallic glasses with six different alloy systems is shown in Fig. 2-19.

2-5 Fatigue properties in BMGs

It is well known that the process of accumulated damage and failure due to cyclic loading is called fatigue. Fatigue is a result of a progressive, localized, and permanent structural-damage behavior when the applied cyclic stresses are under the ultimate tensile strength of the materials. Two categories of fatigue testing are frequently the performed, one is high-cycle fatigue test that the initial deformation is primarily elastic, and the other is low-cycle fatigue test that results in the elastoplastic deformation. The main factors affected fatigue failures are generally the number of loading cycles, stress range, mean stress, and local stress concentrations [105]. The stress-life (S-N) curve shows the amplitude of stress, stress range, or maximum stress versus the number of cycles to failure, N. This curve can present the fatigue life (or fatigue-endurance limit) and fatigue strength of materials. Table 2-2 is a summary of fatigue properties of the Zr-based BMGs and various crystalline alloys from the literatures [134, 135]. An increasing trend of the fatigue-endurance limit with increasing material tensile strength generally occurs in the crystalline materials but not clear in BMGs.

The behavior of fatigue crack growth in BMGs is similar to that of some high-strength alloys, but the behavior of fatigue life is significantly different between them [105]. On the other hand, the fatigue properties of BMGs often reveal discrepancies in the results from different research groups. For instance, the fatigue resistance for BMGs was rated as poor relative to traditional crystalline materials [136, 137], but not all studies are in agreement on this point [42, 43]. The complicating issues in BMGs fatigue properties may be due to the differences in specimen geometry and preparation. The suitably large specimens for testing are always lack in BMGs.

Free volumes and shear bands are also relevant to the fatigue damage mechanism of BMGs. The shear band formation and propagation usually go along with the local increase of free volumes and crack sites within BMGs due to the weakness in the shear bands or shear-off steps (Fig. 2-20) [42, 43], subsequently leading a fracture and fatigue damage, as demonstrated in Fig. 2-21. A simple four component Lennard-Jones simulation model was used to study the fatigue-damage behaviors in metallic glasses and proposed that the free volume level would increase and would be localized with each deformation cycle during the cyclic loading in both the shear and tension tests [138]. They believed that this occurrence would induce the initiation of fatigue damage and/or shear-band formation in BMGs. It follows that, if we can reduce the free volumes in BMGs, the plastic deformation and fatigue damage might be retarded and the fatigue life might be extended.

Through using positron annihilation spectroscopy (PAS) measurements on the effects of free volume changes, it was found that the crack growth and fatigue lifetime will increase with decreasing free volumes in the glass matrix, but the fatigue-crack-growth rates are insensitive to free-volume variations [139]. In contrast, as the crack propagates, the stress or strain concentration induces an increase in free volume within a transformation zone at the crack tip. That controls the local flow properties and makes the fatigue crack growth insensitive to the initial free volume state. The effects of reduction in free volume are often coupled with the states of residual stresses. Specifically, residual compression stresses on the specimen surfaces reduce the crack propagation rate in the threshold region and improve its fracture toughness. Their relationships with fatigue threshold, fracture toughness, and fatigue limit are shown in Fig. 2-22 [139]. In addition, the temperature does not have large influence on the propagation of fatigue crack of BMGs [105]. With the above limited information, the further exploration on the critical theoretical model and basic fatigue-damage mechanism in fatigue behavior of BMGs is still needed.

Chapter 3 Background of Molecular Dynamics Simulation

Characterization of basic material properties at microscopy level has been recognized to be more and more important lately. In despite of the development and application of electron microscopy on the microstructural analysis, observation of the underlying energetic and interaction mechanism at the atomic level is not always accessible by experimental tools in most situations. In such cases, using the computer-based techniques seems to be promising [140]. Molecular dynamics (MD) and Monte Carlo (MC) simulations are two of the powerful atomic level simulate methods that are widely applied to study the atomic topology of BMGs in the recent years [30-33, 36, 92-94]. They can not only obtain strict numerical results about a complex system in microscopic scale, but can also produce macroscopic behavior under precisely controlled conditions. As compared with the MC method, time dependence is the advantage of MD to simulate the physical mechanism of rate relationship. For example, it is possible to consider the dependence of the glass properties on quench rates[141], or mechanical properties on strain rates [126].

A brief description of the MD methods is given in the following sections; the detailed presentations can be referred to textbooks elsewhere [140, 142].

3-1 Equations of motion and potential function

In the MD method, the classical Newton's motion equations are adopted to solve for the atoms molecules as

$$m_i \frac{d^2 r_i}{dt^2} = F_i = -\frac{\partial \Phi}{\partial r_i}, \tag{3-1}$$

where m_i, r_i, F_i are mass, position vector, force vector of molecule i, respectively, and Φ is the potential of the system. The potential function Φ describes how the potential energy of a system of N atoms depends on the coordinates of the atoms, r_1, r_2, …, r_N. It is assumed that the electrons adjust to new atomic positions much faster than the motion of the atomic nuclei (Born-Oppenheimer approximation). When the discrete time steps Δt which is usually given between 1-10 fs and a set of thermodynamic variables such as volume, pressure and temperature are chosen, the time evolution of the system is determined through a deterministic calculation of the trajectory of each particle in the phase space. This is in contrast to the MC method [140, 142], where the system evolves according to stochastic dynamics by setting up a random walk to sample configurations via a given distribution function.

It is well known that the classic equation of motion is a good approximation of the Schrödinger equation if the mass of atom is not too small and the system temperature is not too low. Once the potential of the system is taken, Eq. (3-1) should be solved by numerical methods. In principal, any of the gas, liquid, solid states, and inter-phase phenomena can be solved without the knowledge of "thermo-physical properties" such as thermal conductivity, viscosity, latent heat, saturation temperature and surface tension [143, 144].

The potential of a system Φ (r_1, r_2,…..r_N) can often be reasonably assumed to be the sum of the effective pair potential $\phi\,(r_{ij})$ as

$$\Phi = \sum_{i}\sum_{j>i}\phi(r_{ij}), \tag{3-2}$$

where r_{ij} is the distance between molecules i and j. The assumption of Eq. (3-2) is often employed for simplicity even though the validity is questionable. The covalent system such as carbon and silicon cannot accept the pair-potential approximation. Such categories of potential is developed from the Schrödinger equation that accounts for the position of nuclei and electrons, but using computations such as first principle theory describing electronic degrees of freedom are severely computation restrictive [143, 144]. About 1,000 atoms are the utmost amount that can be solved by state-of-the-art computations. To increase a calculating length scale, various approximation strategies have been developed, in which the electronic effects are averaged out and only the nuclear coordinates are considered as atomic coordinates for instance pair potentials. Lennard-Jones potential is a typical example of pair potential which has form given below [143, 144]:

$$\phi(r) = 4\varepsilon\left[\left(\frac{\sigma}{r}\right)^{12} - \left(\frac{\sigma}{r}\right)^{6}\right], \tag{3-3}$$

where ε and σ are energy and length scales, respectively, and r is the intermolecular distance, as shown in Fig. 3-1. This potential has a well description on the characteristics of inert monatomic molecules (the parameters of ε and σ for each molecule are listed in Table 3-1). It also has a well investigation on the atomic behavior, which the intermolecular van der Waals interaction is the major influence in the system, of about several million-billion atoms. However, the nature of bonding is not accounted for in pair potentials. This leads to unphysical effects in the core of lattice defects such as unusually high stacking fault energy in metals [145]. Furthermore, pair potentials can not account for environmental dependence due to the many body effects in the intermolecular interaction, e.g. atoms in the bulk is too similar to the atoms on the surface or near a defect sites, which are important in metals.

For metallic behaviors, an alternative simple but rather realistic approach to the description of bonding in metallic systems is based on the concept of local density. This allows one to account for the dependence of the strength of individual bonds on the local environment which is especially important for simulation of surfaces and defects. Many methods have been proposed since early 1980s, e.g. embedded-atom method - EAM, effective medium theory - EMT, Finnis-Sinclair potential, the glue model, corrected effective medium potential - CEM, etc. and are based on different physical arguments (e.g. tight-binding model, effective-medium theory), but lead to a similar expression for the total energy of the system of N atoms as:

$$E_{total} = \sum_i E_i \,, \tag{3-4}$$

$$E_i = F_i(\rho_i) + \tfrac{1}{2}\sum_{j \neq i} \phi(r_{ij}) \,, \tag{3-5}$$

and

$$\rho_i = \sum_{j \neq i} f_i(r_{ij}) \,. \tag{3-6}$$

Interpretation and the functional forms of F, f, and ϕ depend on a particular method. Take the point of view of effective medium theory or the embedded-atom method for example, the sketch as shown in Fig. 3-2, the energy of the atom i is determined by the local electron density at the position of the atom and the function f describes the contribution to the electronic density at the site of the atom i from all atoms j. The sum over function f is therefore a measure of local electron density ρ_i. The embedding energy F is the energy associated with an atom embeded in the electron environment described by ρ. The pair-potential term ϕ describes their electrostatic contributions. The general form of the potential can be considered as a generalization of the basic idea of the density functional theory that the local electron density can be used to calculate the energy. Complying with different physical interpretations, the methods to determine the way function are different as well. Some functions and parameters are driven from the first principles calculations and others are guessed or fitted to the experimental data. Generally, the results are basically rather similar.

Good ability to describe the variation of the bond strength with coordination is the main advantage of these methods compared with pair potentials. Increase of coordination would decrease the strength of each of the individual bonds and increase the bond length, resulting in a reproduction for the bulk, surface, and defects properties. In the past decades, such category potentials have been widely used in several studies involving modeling of grain boundaries, fracture studies, study of surfaces, wear and friction.

3-2 Ensembles

Once the potential is chosen, the trajectories of atoms are determined straightforward by employing Newton’s laws to the force fields obtained from radial derivatives of potentials in molecular dynamics [140]. The classical molecular dynamics simulations are performed on a NVE (N is the number of particles, V is the volume, E is the total potential energy) ensemble, which considers the movement of a constant number of particles in a box of fixed size and shape, and the system is assumed to be free from any external force so that number of particles, volume, and the total potential energy are conserved, that is, a micro-canonical ensemble. The advantage of NVE ensemble is easy to handle but difficult to make direct comparison with experiments because laboratory experiments are usually carried out at constant pressure and temperature.

Additional canonical ensemble commonly applied to include the thermodynamic effect in MD is the isothermal-isobaric (NPT) ensemble which further considers the fluctuation of temperature (T) and pressure (P) conditions [140]. The total energy in this ensemble is fluctuated by the interaction with a piston and through the thermal contact with a heat bath. The temperature T is related classically to the kinetic energy, and therefore the isothermal condition in the ensemble is realized by adjusting the velocities v_i of the particles in every time step of the simulation [140]:

$$v_i \rightarrow v_i \sqrt{3Nk_B T / \sum_{i=1}^{N} m_i v_i^2} \ . \tag{3-7}$$

This velocity-scaling method is an approximation by using Gaussian constraint method to fit the correct canonical distribution in the coordinate space [146, 147]. Similarly, a simple relation of pressure in MD is expressed by the virial equation:

$$P = \frac{Nk_B T}{3V} - \frac{1}{3}\sum_{1}^{N}\left(\sum_{j>i}^{N} \frac{\partial \Phi(r_{ij})}{\partial r_{ij}} r_{ij} \right) + P_{ex} \, , \tag{3-8}$$

where $Nk_B T$ is related to the average of the kinetic energy of the system as

$$P = \frac{1}{3V}\sum_{i=1}^{N}\left(m_i v_i^2 - \sum_{j>i}^{N} \frac{\partial \Phi(r_{ij})}{\partial r_{ij}} r_{ij} \right) + p_{ex} \, , \tag{3-9}$$

where v_i is the velocity of particle i, and r_{ij} is the vector joining particle i to particle j. $F_{ij} = -\partial \Phi(r_{ij}) / \partial r_{ij}$ is the force exerted by particle j on particle i and P_{ex} is the external pressure acting on system. From this representation, the pressure can be adjusted by expanding or contracting the simulation box.

In the history of ensemble development, Andersen [148] first advanced a refined constant pressure ensemble by the extended Lagrangian method. In his method, the volume is viewed as a degree of freedom which fluctuates with the consistent kinetic and potential term in the total Hamiltonian of an extended system. However, the constant temperature is performed by stochastic collisions with a heat bath in the Andersen's approximation. Nosé and Hoover [149-151] extended in the similar method based on a clever use of an extended

Lagrangian to treat the constant temperature condition by adding a degree of freedom which describes the coupling to the heat bath. Subsequently, Parrinello and Rahman [152] extended this technique to allow a change of both the shape and volume of the simulation box. The Parrinello and Rahman scheme made the ensemble of MD application be complete especially for studying phase transitions in solids.

3-3 Integration of the Newtonian equation

The most common MD algorithm for solving the integration of the equation of motion is the Verlet method [140], the integration scheme of Verlet can be simply derived by the Taylor expansion of the equation of motion as follows:

$$r_i(t+\Delta t) = r_i(t) + \Delta t v_i(t) + \frac{1}{2}\Delta t^2 \frac{F_i(t)}{m_i}, \tag{3-10}$$

$$r_i(t-\Delta t) = r_i(t) - \Delta t v_i(t) + \frac{1}{2}\Delta t^2 \frac{F_i(t)}{m_i}. \tag{3-11}$$

Through summing up and rearranging, it becomes

$$r_i(t+\Delta t) = 2r_i(t) - r_i(t-\Delta t) + \Delta t^2 \frac{F_i(t)}{m_i}. \tag{3-12}$$

The velocities can be calculated from:

$$v_i(t) = \{r_i(t+\Delta t) - r_i(t-\Delta t)\}/2\Delta t. \tag{3-13}$$

Another common algorithm is the leap-frog method as shown below:

$$v_i\left(t+\frac{\Delta t}{2}\right) = v_i\left(t-\frac{\Delta t}{2}\right) + \Delta t\frac{F_i(t)}{m_i}, \tag{3-14}$$

$$r_i(t+\Delta t) = r_i(t) + \Delta t v_i\left(t+\frac{\Delta t}{2}\right). \tag{3-15}$$

After the velocity of each particle is calculated by Eq. (3-14), the position is obtained by

Eq. (3-15). More elaborate integration schemes such as Gear's predictor-corrector method and Beeman algorithms [140] are sometimes employed depending on the complexity of the potential function and the demand of the accuracy of motion in each time step.

3-4 Periodic boundary conditions

Due to the restriction of computations, it is difficult to deal with the number of atoms as practical condition in the MD system. The numerical system with a typical particle number in the range of 10^3 is necessarily limited in size. A system under this size should be considerably affected by the free surface effects that easily lead to a deviation on the simulated results as compared with bulk properties. Periodic boundary conditions are usually used to minimize these finite-size effects [140, 143, 144]. This approach consists in a periodic repetition of the simulation box in the three directions to fill the whole space, as illustrated in Fig. 3-3 [143]. Any interaction of molecules beyond the periodic boundary is calculated with replica molecules. This utilization removes all free surfaces. By construction, each molecule possesses infinity of periodic images.

In order to avoid the calculation of potential between a molecule and its own replica, the minimal image convention is adopted [140, 143]. Only interaction with the closest images is taken into account in this scheme. The range of the interaction is assumed to be smaller than half of the cubic box length.

3-5 List method and cut-off radius

Since most potentials for modeling metals are short-ranged force, the interactive strength of two atoms would be reduced rapidly as increasing the distance between them and would decay smoothly to zero at a distance r_c. That is the cut-off radius of the potential in the MD simulations. The advantage of using cut-off radius is to reduce the laborious forces calculations due to the large number of particles pairs in a system, thus the interactions are limited to the neighbors at distances smaller than r_c. The calculation of the different $N(N-1)/2$ distances in every integration step also wastes a significant computing time. This can be considerably reduced by making use of the some techniques such as Verlet-list and cell-list [143, 153]. To every atom, one applies a neighbor list which contains all particles within a Verlet-radius r_v, chosen to be reasonably larger than r_c. Only the particles belonging to its list are considered in calculating the forces acting on a given atom. The neighbor list is updated once every about 5 to 20 integration steps depending on the mobility of the particles, such that the estimated maximal displacement of the particles between two updating steps remains smaller than the difference $r_v - r_c$, as shown in Fig. 3-4 [143, 153].

Figure 3-5 [143, 153] perform another scheme, cell-list, which is often used to treat a system with larger particle numbers. In this technique, the cubic simulation box is divided into a regular lattice of $n_{cell} \times n_{cell} \times n_{cell}$ cells, and the side of the cell $l_{cell} = L/n_{cell}$ is greater than the potential cutoff distance r_{cut}. Thus, it is only necessary to look for atoms in the same cell as the atom of interest, and in its nearest neighbour cells. Currently, it becomes preferable to apply the Cell-list linked Verlet-list in order to enhance the efficiency for large systems with short-range forces [140, 143, 153]. A flow chart of a typical molecular dynamics code is illustrated in Fig. 3-6.

Chapter 4　Model and Theory

4-1　Cyclic transformation between nanocrystalline and amorphous phases in Zr based intermetallic alloys during ARB

4-1-1　Tight-binding potential

In the simulation of Zr based alloys of the ARB process, all the atomic interactions are modeled by the many body, tight-binding potential as follows [154]:

$$E_i = -\left\{ \sum_j \xi^2 \exp\left[-2q\left(\frac{d_{ij}}{d_0} - 1 \right) \right] \right\}^{1/2} + \sum_j A \exp\left[-p\left(\frac{d_{ij}}{d_0} - 1 \right) \right], \tag{4-1}$$

where ζ is an effective hopping integral, d_{ij} is the distance between atoms i and j, and d_0 is the first-neighbor distance. The first part in the potential function is the summary of the band energy, which is characterized by the second moment of the d-band density of state. Meanwhile, the second part is a Born-Mayer type repulsive form. The parameters ζ, A, p, and q are determined by the experimentally obtained values of cohesive energy, lattice parameter, bulk modulus and 2 shear elastic constants (C_{44} and $C' = 2(C_{11} - C_{12})$, respectively) [154]. As introduced in Chapter 3, this empirical many body potential can perform the thermodynamic and structural properties of most transition metals and alloys with better accuracy than the common pair potential. It overcomes the difficulties of pair potential on the dealing with metallic characteristics, e.g. elastic constants, stacking fault energies, surface structure, and relaxation properties [154]. The tight-binding potential also proposes a simpler mathematic form as compared with other many body potentials to save computing time which is important especially for a large simulation model.

Subsequently, in order to use this potential in the MD simulation, it is needed to find the interatomic forces. The forces are given by the gradient of the potential energy. Since the potential depends on the interatomic distances only, the force on atom *i* can be expressed as

$$\vec{F}_i = \sum_{j \neq i} \left(\frac{\partial E_i}{\partial r_{ij}} + \frac{\partial E_j}{\partial r_{ij}} \right) \frac{\vec{r}_{ij}}{r_{ij}}, \tag{4-2}$$

or

$$\vec{F}_i = \sum_{j \neq i} F_{ij} \frac{\vec{r}_{ij}}{r_{ij}}, \tag{4-3}$$

where

$$F_{ij} = \frac{\partial E_i}{\partial r_{ij}} + \frac{\partial E_j}{\partial r_{ij}}. \tag{4-4}$$

The expression for F_{ij} is analytic and given with the notations introduced in Eq. (4-5).

$$F_{ij} = -\frac{2Ap}{r_0} \exp\left[-p\left(\frac{r_{ij}}{r_0} - 1 \right) \right] + \frac{q\xi}{r_0} \left[\phi_i^{-1/2}(2q) + \phi_i^{-1/2}(2q) \right] \exp\left[-2q\left(\frac{r_{ij}}{r_0} - 1 \right) \right] \tag{4-5}$$

where

$$\phi_k(\lambda) = \sum_l \exp\left[-\lambda\left(\frac{r_{kl}}{r_0} - 1 \right) \right]$$

The term ϕ_k is the contribution of surrounding particles stems from the N-body character of the potential. The parameters of tight-binding potential used in this dissertation are listed in Table 4-1.

4-1-2 Simulation model and conditions

In the simulation model of ARB process, a bi-layered structure consisting of hexagonal closed-packed (HCP) Zr coupled with the face-centered cubic (FCC) Ni elemental layers, measuring 20 nm in width, 20 nm in length and 12 nm in thickness for each elemental layer, was set to be the starting alloy model in order to trace the final cyclic transformation stage between nanocrystalline and amorphous phases during ARB. Meanwhile, the other model consisting of HCP Zr and HCP Ti is set up under identical condition with above case for comparison. The designed amounts of Zr and Ni atoms are 89,280 and 188,442 for the Zr-Ni system ($Zr_{32}Ni_{68}$), while 116,064 Zr atoms and 118,184 Ti atoms are designed for the Zr-Ti systems ($Zr_{50}Ti_{50}$). The processing ARB speed in the MD simulation is 0.05 nm/fs or 2×10^{12} s^{-1}. The present simulation employs the verlocity verlet algorithm to calculate the trajectories of the atoms and the scaling method is adopted during the simulation to control system temperature at 300 K. The repeated ARB strain-and-stack procedure applied in the simulation is schematically illustrated in Fig. 4-1.

In the consideration to the computing efficiency caused of data communication in a large scale, the distributed computing is the straightforward to implement parallelization method into MD program[155]. There are two common parallel algorithms for MD, one is particle decomposition method, and the other is spatial decomposition. In the particle decomposition method, all particles in the simulation cell are assign numbers, partitioned, and distributed to processors, as shown in Fig. 4-2 (a) [155]. The allotted particles are governed by each processor from the beginning to the end of the calculation. The globally data such as positions of particles must be shared and stored into each processor, which will decrease scalability and calculating efficiency in the system with increasing the number of processors, resulted from the synchronous global communication of broadcasting. Nevertheless, easily adjusting load balance among processors by uniform assigning the same number of particles to each processor and simply program writing are thought as advantages.

In the spatial decomposition method, the particles are divided locally into the partitioned space of simulation cell belonging to each processor, as depicted in Fig. 4-2 (b)[155]. In this method, only the communication data of particles near or across the boundary region are necessarily exchanged among processors, the others are still restricted to local areas. Therefore, the scalability and communication cost are significantly better than the particle decomposition method. However, load imbalance will come up as extremely inequality of the distribution of particles. In this thesis, the particle decomposition method is adopted for executing MD simulation, since the change of modeling shape is required during the deformation process.

4-1-3 Analysis methods for structural properties

In the current MD simulation, one of the most common methods to measure the structure features of a system is the radial distribution function (RDF), *g*(r). Also, the RDF is common applied to neutron and X-ray scattering experiments on simple fluids or amorphous structures. The RDF plays a central role in theories of the liquid state. Numerical results for the RDF can be compared with theoretical predictions and then offer a criterion to test a particular theory [140]. Measuring the RDF in the MD simulation is straightforward by considering the ratio between the average number density $n(r)$ at a distance r from any given atom and the density at a distance r from an atom in an ideal gas at the same overall density. The equation of RDF [156] can be calculated as

$$g(r) = \frac{V}{N^2}\left\langle \sum_{i=1}^{n} \frac{n(r)}{4\pi r^2 \Delta r} \right\rangle, \tag{4-6}$$

where N denotes the number of atoms in the simulation cell, V is the volume of the same cell, and $n(r)$ the number of particles which can be found in the shell from r to $r+\Delta r$. For a binary alloy system, partial radial distribution function (PRDF) for atom α and atom β is calculated by [156]

$$g_{\alpha\beta}(r) = \frac{V}{N_\alpha N_\beta} \left\langle \sum_{i=1}^{N_\alpha} \frac{n_{i\beta}(r)}{4\pi r^2 \Delta r} \right\rangle . \tag{4-6}$$

Subsequently, a powerful tool proposed by Honeycutt and Anderson [75] is used to study the local symmetry of the atomic arrangement within short-range ordering during the transformation process in the simulation model. Honeycutt and Anderson had used the pair analysis technique (termed as the HA pair index) to study the local structure features in disordered systems such as liquid and glass in early years [75]. This approach provides very clear information about the local symmetry of atomic arrangement more than the radial distibution function, and has been used to simulate the grain boundary microstructure transition, local cluster structure, and glass forming of metallic alloys under the rapid cooling condition [157, 158].

In this technique, two atoms are viewed as forming a bond pair if they are within a given cutoff distance that equals the first minimum in the partial radial distribution function (for example, Zr-Zr, Ni-Ni and Ni-Zr in the Zr-Ni system). There is a sequence of four integers to characterize the local structures according to the HA index. The first integer is to identify whether or not the atoms bonded in the HA pair are the near neighbors; 1 means yes, and 2 means not. The second integer is the number of the near neighbors shared by the HA pair. The third integer denotes the number of bonds among the shared neighbors. When the first three indices are identical but the bond geometries are different, the forth integer is added.

According to this method, different HA indices will represent different local structures, as shown some examples in Fig. 4-3 [159]. For example, the 1421 and 1422 pairs would exist predominantly in the close-packed crystalline structure, such as a face-centered cubic (FCC) type (including alloys, such as $L1_0$) or hexagonal closed-packed (HCP) type (including the B19 lattice). For a FCC cluster, the predominant pairs would be the 1421 ones; while in the HCP cluster, there are typically around 50% of the 1421 and 50% of the 1422 pairs. The 1441 and 1661 pairs are characteristic of the body-centered cubic (BCC or B2) structure. The 1551, 1541, and 1431 pairs are referred to the common short-range local structures of an amorphous or liquid state. Finally, the 1321 is a packing related to the rhombohedra, and this pair tends to evolve when the icosahedra 1551 packing is formed and can be viewed as the side product accompanying the icosahedra atomic packing.

Furthermore, one can identify several important polyhedra with specific symmetries through the utilization of HA technique. A cluster can be easy identified as a FCC polyhedron, if its center atom only has twelve near-neighbors consisting of twelve 1421 bonded pairs. Similarly, one can define a HCP polyhedron, if a center atom is surrounded by twelve near-neighbors but consisting of six 1421 and six 1422 bonded pairs. If a center atom has twelve neighboring atoms consisting of twelve 1551 bonded pairs, one can define an icosahedron. A defected icosahedron is composed of only 1551, 1441, and 1661 bonded pairs. Figure 4-4 shows four types of the above-mentioned clusters detected by the HA method in crystals and glasses [158, 160].

4-2 Atomic simulation of vitrification transformation in Mg-Cu thin film

4-2-1 Effective-medium theory potential

In this section, the effective-medium theory (EMT) potential is employed in this work to study the Mg-Cu system. The EMT model used in this simulation corresponds to a parameterization of the EMT barriers calculated by Jacobsen et al [161, 162]. The basic idea of his method is straightforward as that the total energy of a given atom in the system can be determined by the effect of their surrounding atoms. The energy of an atom in an arbitrary environment should be calculated by first estimating it in a well chosen reference system, namely the effective medium, and then by evaluating the energy difference between the real and reference systems. Thus the total energy of the system is written as

$$E = \sum_i E_{c,i} + (E - \sum_i E_{c,i}), \tag{4-8}$$

where $E_{c,i}$ is the energy of atom i in the reference system. A perfect FCC crystal is taken as the reference system in the present model. How to derive the form of the correction term $E - \sum_i E_{c,i}$ in Eq. (4-8) from the density function theory has been presented in the reference papers [161, 162].

The total energy of the system can be written as

$$E = \sum_i E_{c,i}(n_i) + \Delta E_{AS} + \Delta E_{1el} . \tag{4-9}$$

The first term $E_{c,i}(n_i)$ is the cohesive function of system and n_i is the embedding density of atom i. The second term ΔE_{AS} is atomic-sphere correction which is the difference in electrostatic and exchange-correlation energy for the atoms in an interested system and in the reference system, and ΔE_{1el} is one-electron correction that is the difference in the sum of one-electron energies in the two systems. The atomic-sphere correction ΔE_{AS} can be approximated well by a difference of pair potential in the two systems, and the considerable effects of ΔE_{1el} can be included in the adjustment of pair potential form V_{ij}. Thus the Eq. (4-9) can be expressed as

$$E = \sum_i \left[E_{c,i}(n_i) + \Delta E_{AS}(i) \right] \tag{4-10}$$

$$= \sum_i \left\{ E_{c,i}(n_i) + \tfrac{1}{2} \left[\sum_{j \neq i} V_{ij}(r_{ij}) - \sum_{j \neq i}^{ref} V_{ij}(r_{ij}) \right] \right\} . \tag{4-11}$$

The embedding density n_i describes the superimposing contributions to the electronic density at the site of the atom *i* from all atoms *j*, and is expressed the function of intermolecular distance r_{ij} and Wigner-Seitz sphere radius s_i (the same as neutral sphere radius).

$$n_i = \sum_{j \neq i} \Delta n_j (s_i, r_{ij}) \tag{4-12}$$

The neutral sphere radius s_i is obtained by solving Eq. (4-12),

$$s_i = s_0 - \frac{1}{\beta \eta_2} \log\left(\frac{\sigma_{1,i}}{12} \right), \tag{4-13}$$

and

$$\sigma_{1,i} = \sum_{j \neq i} \exp\left[-\eta_2 (r_{ij} - \beta s_0) \right]. \tag{4-14}$$

The cohesive function $E_{c,i}(n_i)$ can also be simplified as the function of Wigner-Seitz sphere radius s_i

$$E_C(s_i) = E_0 f\left[\lambda (s_i - s_0) \right], \tag{4-15}$$

$$f(x) = (1 + x) \exp(-x), \tag{4-16}$$

where s_0 is the constant of the equilibrium neutral-sphere radius and E_0 is the cohesive energy. Finally the last term in the Eq. (4-10) can be written as Eq. (4-17) since there are 12 nearest neighbors at a distance $\gamma = \beta s_i$ determined by the radius s_i in the FCC reference system,

$$\Delta E_{AS}(i) = \tfrac{1}{2} \left[\sum_{j \neq i} V(r_{ij}) - 12 V(\beta s_i) \right]. \tag{4-17}$$

Note that β is a geometric factor approximating to $(16\pi/3)^{1/3}/\sqrt{2} \approx 1.81$.

The pair potential in Eq. (4-17) is parameterized as Eq. (4-18),

$$V(r) = -V_0 \exp\left[-\kappa (r/\beta - s_0) \right]. \tag{4-18}$$

All the parameters mentioned above can be determined from experimental properties such as lattice constants, cohesive energies, as well as elastic constants for the interested metals and their figures are listed in Table 4-2[161, 162]. For two-component metal systems (A, B), the neutral radius s_i of a type A atom in Eq. (4-13) should be slightly adjusted to join the effects of additional type B atoms by a weighting coefficient χ_{AB}

$$s_A = s_{0A} - \frac{1}{\beta\eta_{2A} + \eta_{1B} - \eta_{1A}} \log\frac{1}{12}(\sigma_{1AA} + \chi_{AB}\sigma_{1AB}), \tag{4-19}$$

where σ_{1AA} is the sum of Eq. (4-14) running over the A neighbors to the atom A and σ_{1AB} is the sum over the B neighbors. The coefficient χ_{AB} is given by

$$\chi_{AB} = \frac{n_{0B}e^{-\eta_{1B}s_{0B}}}{n_{0A}e^{-\eta_{1A}s_{0A}}} e^{(\eta_{1B}-\eta_{1A})(s_A - s_{0A})}. \tag{4-20}$$

The last exponential function in Eq. (4-20) is usually very small so that it can be taken to be 1 although the neutral radius s_i is contained at the same time. Similarly, the atomic sphere correction for a type A atom is written

$$\Delta E_{AS}^{A} = \tfrac{1}{2}\left\{ \sum_{j_A \neq i} V_{AA}(r_{ij}) + \chi_{AB} \sum_{j_B \neq i} V_{AB}(r_{ij}) - 12V_{AA}(\beta s_{iA}) \right\}. \tag{4-21}$$

This EMT potential form has previously been shown to give a reasonable overall description of the FCC metals including transition and noble metals as well as their alloys. They have been great used in the study of mechanical properties of crystalline metals [163]. For the Mg-Cu system, Bailey et al. [164] refit the parameters of both elements not only from basic properties of the pure elements but also considering the formation energies of two intermetallic compounds, Mg_2Cu and $MgCu_2$. The reasonable formation energies are important for the amorphous alloys, otherwise the system will simply separate into regions of pure Cu and Mg, respectively.

4-2-2 Derivation of force for EMT potential

As the above-mentioned in dealing with tight-binding potential form, it is needed to find the forces in order to use this potential in the MD simulation. The forces are given by the gradient of the potential energy. Since the potential also depends on the interatomic distances only, the force on atom *i* can be expressed as

$$\vec{F}_i = \sum_{j \neq i} F_{ij} \frac{\vec{r}_{ij}}{r_{ij}}, \tag{4-22}$$

where

$$F_{ij} = \frac{\partial E_i}{\partial r_{ij}} + \frac{\partial E_j}{\partial r_{ij}}, \tag{4-23}$$

and

$$\frac{\partial E_i}{\partial r_{ij}} = \frac{\partial}{\partial r_{ij}} \sum_i \left\{ E_{c,i}(n_i) + \Delta E_{AS}^{A}(i) \right\}, \tag{4-24}$$

$$\frac{\partial E_c}{\partial r_{ij}} = E_0 \frac{\partial f(x)}{\partial r_{ij}} = -E_0 x \exp(-x) \frac{\partial x}{\partial r_{ij}}, \tag{4-25}$$

where the *x* is given by

$$x = \lambda_A (s_A - s_{0A}) = \frac{-\lambda_A}{C_A} \ln \frac{1}{12} (\sigma_{1AA} + \chi_{AB} \sigma_{1AB}). \tag{4-26}$$

The constant C_A is assumed that $\beta\eta_{2A} + \eta_{1B} - \eta_{1A} = C_A$. Assuming the calculated atom *i* is a type A species and the species of its neighbors *j* atom is the same with A atom (e.g. i = A, j = A), thus the distance between atom *i* and atom *j* is marked r_{ijA}, else is r_{ijB}. By algebra and separation of variables from Eq. (4-26), we obtain

$$\frac{\partial x}{\partial r_{ij_A}} = \frac{-\lambda_A}{C_A \sigma_{1AA} + (C_A + C_1) \chi_{AB} \sigma_{1AB}} \frac{\partial \sigma_{1AA}}{\partial r_{ij_A}}, \tag{4-27}$$

or

$$\frac{\partial x}{\partial r_{ij_A}} = \lambda_A \frac{\partial s_A}{\partial r_{ij_A}}, \tag{4-28}$$

where $C_1 = \eta_{1B} - \eta_{1A}$.

The derivative of the sphere radius s_A is given as

$$\frac{\partial s_A}{\partial r_{ij_A}} = \frac{-1}{C_A \sigma_{1AA} + (C_A + C_1) \chi_{AB} \sigma_{1AB}} \frac{\partial \sigma_{1AA}}{\partial r_{ij_A}}, \tag{4-29}$$

where

$$\frac{\partial \sigma_{1AA}}{\partial r_{ij_A}} = -\eta_{2A} \exp[-\eta_{2A}(r_{ij_A} - \beta s_{0A})]. \tag{4-30}$$

Similarly for the case of *i* atom = A species and *j* atom = B species, the differential equation of *x* in Eq. (4-28) becomes

$$\frac{\partial x}{\partial r_{ij_B}} = \lambda_A \frac{\partial s_A}{\partial r_{ij_B}}, \tag{4-31}$$

where

$$\frac{\partial s_A}{\partial r_{ij_B}} = \frac{-1}{C_A \sigma_{1AA} + (C_A + C_1)\chi_{AB}\sigma_{1AB}} \chi_{AB} \frac{\partial \sigma_{1AB}}{\partial r_{ij_B}}, \tag{4-32}$$

and

$$\frac{\partial \sigma_{1AB}}{\partial r_{ij_B}} = -\eta_{2A} \exp[-\eta_{2A}(r_{ij_B} - \beta s_{0A})]. \tag{4-33}$$

Finally, the differential equation of atomic sphere correction for the case of *i* = A, *j* = A is given by

$$\frac{\partial \Delta E_{AS}^{A}}{\partial r_{ij_A}} = \frac{\partial}{\partial r_{ij_A}} \sum_{j_A \neq i} V_{AA}(r_{ij_A}) + \frac{\partial}{\partial r_{ij_A}} \chi_{AB} \sum_{j_B \neq i} V_{AB}(r_{ij_B}) - 12 \frac{\partial}{\partial r_{ij_A}} V_{AA}(\beta s_{iA}). \tag{4-34}$$

The first term by the relation in Eq. (4-34) is

$$\frac{\partial}{\partial r_{ij_A}} \sum_{j_A \neq i} V_{AA}(r_{ij_A}) = \frac{V_0 \kappa_A}{\beta} \exp\left[-\frac{\kappa_A}{\beta}(r_{ij_A} - \beta s_{0A})\right], \tag{4-35}$$

the second term is

$$\frac{\partial}{\partial r_{ij_A}} \chi_{AB} \sum_{j_B \neq i} V_{AB}(r_{ij_B}) = \frac{\partial \chi_{AB}}{\partial r_{ij_A}} \sum_{j_B \neq i} V_{AB}(r_{ij_B}), \tag{4-36}$$

and the last term is

$$\frac{\partial}{\partial r_{ij_A}} V_{AA}(\beta s_{iA}) = V_{0A} \kappa_A \exp[-\kappa_A(s_A - s_{0A})] \frac{\partial s_A}{\partial r_{ij_A}}. \tag{4-37}$$

Similarly, the differential equation of atomic sphere correction for the case of *i* = A, *j* = B is rewritten as

$$\frac{\partial \Delta E_{AS}^{A}}{\partial r_{ij_B}} = \frac{\partial}{\partial r_{ij_B}} \sum_{j_A \neq i} V_{AA}(r_{ij_A}) + \frac{\partial}{\partial r_{ij_B}} \chi_{AB} \sum_{j_B \neq i} V_{AB}(r_{ij_B}) - 12 \frac{\partial}{\partial r_{ij_B}} V_{AA}(\beta s_{iA}). \tag{4-38}$$

The first term on the right side of the relation is quoted to zero; the second term is taken as

$$\frac{\partial}{\partial r_{ij_B}}\chi_{AB}\sum_{j_B\neq i}V_{AB}(r_{ij_B})=\frac{\partial\chi_{AB}}{\partial r_{ij_B}}\sum_{j_B\neq i}V_{AB}(r_{ij_B})+\chi_{AB}\frac{\partial}{\partial r_{ij_B}}\sum_{j_B\neq i}V_{AB}(r_{ij_B}), \tag{4-39}$$

and the last term is given by

$$\frac{\partial}{\partial r_{ij_B}}V_{AA}(\beta s_{iA})=V_{0A}\kappa_A\exp[-\kappa_A(s_A-s_{0A})]\frac{\partial s_A}{\partial r_{ij_B}}. \tag{4-40}$$

4-2-3 Simulation model and conditions

In this study, an initial sandwich model is constructed by stacking an FCC Cu layer, an HCP Mg layer, and an FCC Cu layer along the z axis. The 2-D scheme of this model is illustrated in Fig. 4-5. Two interfaces between the Cu and Mg layers are set in the [111] direction of FCC Cu and [0002] direction of HCP Mg along the z direction, respectively. The length scale in x, y, and z dimensions of an FCC Cu layer is 3.5 nm × 6 nm × 1.5 nm and of an HCP Mg layer is 3.5 nm × 6 nm × 3.5 nm. The numbers of Cu and Mg atoms in this sandwich model are 5,467 and 3,595, respectively. In addition to the z direction, the periodic boundary condition is employed on the x-y plane. Due to the lattice difference between Cu and Mg, the dimensions of the periodic boundary along the x and y directions are chosen to be large enough to minimize the mismatch effects at the Mg and Cu interface. In order to speed up the formation of a disordered state in the interface between two metals which are reasonably existing present in reality, an equal number of Cu and Mg atoms are artificially exchanged in the interface (see Fig. 4-5). After exchanging the Cu and Mg atoms, the sandwich model is annealed at 300 K for 5×10^6 time step by employing in the NVT ensemble and the equations of motion are solved by the velocity-Verlet algorithm.

4-3 Cyclic loading fatigue in a binary Zr-Cu metallic glass

4-3-1 Interatomic potential used in Zr-Cu

As so far, two of interatomic force field have been fitted to ZrCu, one is the tight-binding potential proposed by Duan *et al.*[156], the other is the EMT potential proposed by Paˇduraru [165] *et a*. Although the EMT potential of ZrCu provides a better precision on the description of the structure of the metallic glass than the former [165], the tight-binding potential provides a simple equation form to writing program and to save calculating efficiency. For that reason, the tight-binding potential is adopted again to model the mechanical properties of Zr-Cu in this part. The parameters of the tight-binding potential for Zr and Cu employed in the current simulation were proposed by Duan *et al.*[156], and the potentials have been shown to be in good agreement with the experiments.

4-3-2 Isothermal-isobaric ensemble and Nosé-Hoover Chain

On the other hand, a more complete ensemble of MD simulation, that is, the isothermal and isobaric (NPT) ensemble, is applied to control the temperature and stress to maintain a reasonable thermodynamic state during the MD-simulation process, as well as to bring the imposed tensile stress on the simulation model. The basic conception of NPT ensemble has already been introduced in Chapter 3. Nosé-Hoover NPT ensemble is known as one of the most popular NPT system in the MD. However, the Nosé-Hoover algorithm generates a correct canonical distribution for MD only when there is just one conserved quantity or there are no external forces and the center of mass remains fixed [140].

To alleviate the restriction for the Nosé-Hoover ensemble, Martyna *et al.* [166-168] extended a new scheme which Nosé-Hoover themostate is coupled to a chain of thermostats, Nosé-Hoover chain. This modification of Nosé-Hoover dynamics has been shown to give a very good approximation to the canonical ensemble even in pathological cases. The significant difference between the original Nosé-Hoover dynamics and new method is shown in Figs. 4-6 (a) and (b) [166-168]. In Fig. 4-6 (a), the trajectories of the harmonic oscillator and the projected distribution functions for the original method do not fill the space even if the initial conditions are changed, but the distribution functions for the new one have good approximations to the canonical results and the dynamics fills space, seeing in Fig. 4-6 (b). As the chains of thermostats are increased, the results will be better.

The equations of motion for the positions and momenta that generate the isobaric-isothermal ensemble are [166-168]:

$$\dot{r}_i = \frac{\mathrm{P}_i}{m_i} + \frac{p_\varepsilon}{W} r_i , \tag{4-41}$$

$$\dot{\mathrm{P}}_i = F_i - \left(1 + \frac{d}{N_f}\right)\frac{p_\varepsilon}{W}\mathrm{P}_i - \frac{p_\xi}{Q}\mathrm{P}_i , \tag{4-42}$$

where N_f is the degree of freedom for the number of particles in d dimensions. The symbols ξ, p_ξ, and Q are the coordinate, momentum and effective mass which are used to describe the thermostate in the Nosé-Hoover chain. The symbols, ε, p_ε and W, are the barostat variables similar to the version of thermostat.

$$\dot{V} = \frac{dVp_\varepsilon}{W} , \tag{4-43}$$

$$\dot{p}_\varepsilon = dV\left(p_{\mathrm{int}} - p_{ext}\right) + \frac{d}{N_f}\sum_{i=1}^{N}\frac{\mathrm{P}_i^2}{m_i} - \frac{p_\xi}{Q}p_\varepsilon , \tag{4-44}$$

$$\dot{\xi} = \frac{p_\varepsilon}{Q} , \tag{4-45}$$

$$\dot{p}_\xi = \sum_{i=1}^{N}\frac{\mathrm{P}_i^2}{m_i} + \frac{p_\varepsilon^2}{W} - \left(N_f + 1\right)kT . \tag{4-46}$$

In the equation, p_{ext} is the external pressure or imposed stress, and p_{int} is internal pressure, which can be calculated during the simulation process from virial equation,

$$p_{\text{int}} = \frac{1}{dV}\left[\sum_{i=1}^{N}\frac{\mathrm{P}_i^2}{m_i} + \sum_{i=1}^{N} r_i \cdot F_i - (dV)\frac{\partial \phi(r,V)}{\partial V}\right]. \tag{4-47}$$

The derivation of time-reversible integration scheme for solving the equation of motion numerically in the NPT ensemble is need to use Trotter expansion formula. The details of using this technique can be found elsewhere.

4-3-3 Simulation model and conditions

The current simulation model consisted of 47,424 atoms, in a mixture of 50% (atomic percent) Zr and 50% Cu in a box size of 9.5 nm × 9.5 nm × 9.5 nm. Periodic boundary conditions were employed in all three dimensions. The glassy structure was obtained by quenching the sample model at a cooling rate 5 K/ps (ps = 10^{-12} s) from 2,000 down to 300 K, followed by an equilibrium for 30,000 time steps. The glass transition was found to be about 650 K according to the volume versus temperature diagram. The average density is about 7.29 g/cm^3, and the potential energy at this as-quenched state is about - 5.233 eV. Because the difference of densities between 1 K/ps and 10 K/ps is 0.096 %, the density is considered insensitive to the cooling rate of the Zr-Cu BMG [110].

Both the stress-control and strain-control modes are included in this simulation. The uniaxial stress-control mode was first applied along the Z axis to implement the tension and compression cyclic-loading fatigue tests. To induce the localization of deformation in the simulation model during the cyclic-loading process, the maximum applied stress amplitude, $\sigma_{\max}$, was chosen to be 1 and 2 GPa, and the strain level during each fatigue cycle was around 2.8% for $\sigma_{\max} = 2$GPa. Note that the 2 GPa stress amplitude might appear to be too high judging from the fact that the fracture tensile or compression stress for bulk Zr-Cu amorphous specimen may only be around 1.5-1.8 GPa. But because of the size effect [169, 170], the stress level in micro- or nano-scale can increase to more than 2.5-3 GPa. The minimum stress, σ_{min}, was set to zero, equivalent to complete unloading; the stress ratio $\sigma_{min}/\sigma_{max}$ is equal to zero. The applied load was increased gradually at a rate of 0.5 MPa/fs (fs = 10^{-15} s) until the maximum tensile stress and then was held for 2,000 fs to reach a relatively equilibrium state, and vice versa. The tensile fatigue cycle is set to be 100 and stress in both x and y directions is maintained at zero during the whole processes. The period of one cycle is 12,000 fs. The applied cycling load is presented in Fig. 4-7 (a).

In order to further amplify the fatigue-induced deformation, the strain-control mode is also used. Several strain rates are selected, that is, at 5×10^9, 1×10^{10}, and 2.5×10^{10} s^{-1}; the maximum strain is set to 2.5%, 4%, and 10% in the z direction, respectively, and all minimum strains were set to be zero. The higher strain rate used in this MD work is due to the inherent nature of current MD simulations especially for cyclic loading work which usually needs very long time compared with the monotonic condition [171, 172]. On the other hand, the MD simulations of the transition metal alloys such as Zr-Ni, or Zr-Cu are generally insensitive to the strain rate effects [125, 173]. Again, the choice of 2.5 to 10% strain might seem to be too high. But from literature reports [174], the metallic glasses in micro- or nano-scaled size can exhibit much higher plastic strain before failure.

Note that in order to recover the induced tensile strain back to zero, the induced load needs to be reversed to the compressive stress, so that the strain-control fatigue is actually under the tension-compression mode, different from the above stress-control fatigue under the tensile mode. When the applied strains reach to the designated values, the models are given a tolerable time steps for relaxation during the cyclic loading process. It was noted that the 2.5% maximum strain case did not show significant difference on the qualitative results from the above 2 GPa stress control mode. Thus the maximum strain was increased to 10% to examine the possible more severe fatigue deformation under such a high strain amplitude.

The maximum stress achieved for this 10% strain-control mode approaches 3 GPa and the Poisson ration is about 0.43. The period of one cycle is about 80,000 fs. Since the strain accumulated during each cycle is much higher for this case, the fatigue cycle for this more severe 10% strain-control mode is set to be 25. The applied cycling-load pattern is presented in Fig. 4-7 (b). While the applied cyclic strain (10%) and the induced cyclic stress (3 GPa) appear to be exceeding the realistic levels for the Zr-Cu bulk metallic glass, the current simulation setup is simply to raise the cyclic strain and stress level to shorten the simulation cycle and time. The illustration applied in the simulation of cyclic fatigue is schematically illustrated in Fig. 4-8.

4-3-4 Observation of local shear strains

In order to quantify plastic deformation at the atomic level, there are three methods frequently used to identify where the irreversible plastic rearrangement are occurring. One is known as slip vector. The expression of slip vector is given in Eq. (4-48),

$$v_{sp} = \frac{\sqrt{\sum_{i=1}^{N} (\vec{r}_{ij} - \vec{r}_{ij}\,')^2}}{N}, \tag{4-48}$$

where N is the total number of nearest neighbors of each atom i, and j is the nearest neighbor of atom i. $\vec{r}_{ij}$ and $\vec{r}_{ij}\,'$ are the difference of two vectors between atom i and atom j, respectively, before and after deformation. Another is the atomic-bond rotation angle (ABRA) change [109]. The ABRA is quantified by calculating the change of angle φ_{ij} between mutual orientations of the nearest-neighbor bond vectors. The angle φ_{ij} is given by

$$\varphi_{ij} = \cos^{-1}\left(\frac{r_{ij} \cdot r_{ij}'}{|r_{ij}||r_{ij}'|}\right), \tag{4-49}$$

where r_{ij} and r_{ij}' are the nearest-neighbor bond vectors before and after deformation. While all atomic bonds rotate during shear deformation, the angle φ_{ij} is directly related to the local atomic shear strain. The third method is the local Lagrangian strain [129, 140], η^{Mises}. To calculate η^{Mises}, it is required to seek a local transformation matrix J_i by minimizing,

$$\sum_{j \in N_i} |r_{ij} J_i - r_{ij}'| \rightarrow J_i = \left(\sum_{j \in N_i} r_{ij}^T r_{ij}\right)^{-1} \left(\sum_{j \in N_i} r_{ij}^T r_{ij}'\right). \tag{4-50}$$

Therefore, each component of local Lagrangian strain η^{Mises} is given by

$$\eta_i = \frac{1}{2}\left(J_i J_i^T - I\right), \tag{4-51}$$

and

$$\eta_i^{Mises} = \sqrt{\eta_{yz}^2 + \eta_{xz}^2 + \eta_{xy}^2 + \frac{(\eta_{yy} - \eta_{zz})^2 + (\eta_{xx} - \eta_{zz})^2 + (\eta_{xx} - \eta_{yy})^2}{6}}\,. \tag{4-52}$$

It is easy to find the fact that the local Lagrangian strain is the better than two formers in the measurement of local inelastic deformation. However, in addition to the extremes (just existing local normal strain or shear strain), there is almost no difference among the results of such three methods for the current case. Therefore, we present the ABRA results to demonstrate where the local shear strains appear under cyclic loading.

Chapter 5   Simulation results

5-1   The results of phase transformation in Zr based intermetallic alloys during ARB

5-1-1   Morphologies of Zr-Ni and Zr-Ti during ARB cycles

Figures 5-1 (a) and (b) are the 2-D sliced plots parallel to the xz plane of the Zr-Ni metallic layers in Ni plan and Zr plan, respectively. There are significant distortions of lattice existing in Zr and Ni matrix after first ARB cycle. Previous studies of the experiments [37-39] have concluded that the pronounced increase in interfacial energy of the nanocrystalline phase lead to the transformation into the amorphous state, and interdiffusion across the phase boundary is the controlling atomic mechanism [175], as depicted in Fig. 5-1(c). Figure 5-1 (d) shows the sliced plot on the interface between two metallic layers. The domain of pure Ni elements embedded in that of Zr element forming two nanocrystalline phases separately. It is similar to the description in the Fig. 5-1 (c).

Figure 5-2 reveals the microstructural evolution of bi-layered $Zr_{32}Ni_{68}$ alloy subjected to various ARB cycles, together with the associated two-dimensional Fourier transform. The bi-layered Zr and Ni structures, with domain size of the same order as the layer thickness (about 5 nm), are fully vitrified after six ARB cycles via pronounced interdiffusion, consistent with our TEM observations and propositions. The simulation shows that the two elemental nanocrystalline phases transform directly to the amorphous alloying phase. There is seemingly no intermediate phase or intermetallic compound induced; the same observed experimentally. The interval from the third to the sixth ARB cycle is the transition between nanocrystalline and amorphous state.

For the current binary metallic system, it needs only 6 cycles for the bi-layered structure, with 5 nm in each layer thickness, to transform into a fully amorphous state. The current result on ARB is very similar to the MA case observed by Lund and Schuh [176, 177]. Meanwhile, with further rolling (to 14 ARB cycles), the amorphous structure was maintained until the end of simulation processing, though there are slight local reversions back to the partial nanocrystalline phases (i.e. slight local cyclic transformation between the 8th and 10th ARB cycle). This conclusion is also supported by the results of Fourier transformation. Figure 5-3 (a) reveals the associated Fourier transform of the pure FCC Ni in the [111] zone axis. The Ni [111] plane texture tends to be stress induced and lie along the rolling plane. The re-crystallized Ni phase size is very close to the observed critical phase size of ~2 nm before vitrification. The corresponding morphologies at the 8th and 9th cycles shown in Figs. 5-3 (a) and (b) indicate that the crystalline structure, surrounded by circles, reappear during ARB cycles. And a phase with such a small size cannot maintain its crystalline structure upon further rolling cycles. Thus, the nano-sized FCC Ni re-states to collapse from the 9th F&R cycle and returns back to amorphous structure at the end of the 10th F&R cycle.

The MD simulated microstructural evolution over the final ARB stage and the associated two-dimensional Fourier transformation of the bi-layered $Zr_{50}Ti_{50}$ subjected to various ARB cycles is revealed in Fig. 5-4. In the $Zr_{50}Ti_{50}$ systems, the nanocystalline structure is fully vitrified after 6 and 4 F&R cycles, respectively. Unlike the observations in the $Zr_{50}Ni_{50}$ system, a faster amorphization process is revealed in $Zr_{50}Ti_{50}$, consistent with the experimental findings.

5-1-2 Morphologies of pure Zr during ARB cycles

The microstructural evolutions of bi-layered pure Zr alloy under strain rate of 8.35×10^{8} s^{-1} after second, 7th, and 8th cycles are respectively shown in Figs. 5-5, 5-6, and 5-7. The pronounced close-packed structures, namely 1421 and 1422 geometries as shown in Figs. 5-5 (a) and (b), are appearing in the matrix. Through the aid of 1321 index in Fig. 5-5 (c), it could be inferred that a number of deformation twinning or twin boundaries are produced by a simple movement of atoms as a result of shear stress parallel to the x-y plan during ARB cycles, either the occurrence of partial dislocations or stacking-fault. Figure 5-5 (d) shows the a few amorphous structures existing in the grain boundaries among different orientation domains. Those deformation mechanisms are induced by large shear load repeatedly during first and 6th cycles with increasing folding and rolling steps. However, the dis-match plans accompanied with those defects are annihilated at 7th cycle especially for amorphous structures (see Fig. 5-6) but resume happening after 8th cycle, as shown in Fig. 5-7.

While applying high strain rate at 9.25×10^{9} s^{-1}, the vitrification would happen quickly after a few cycles. Although one could still find some apparent close-packing structures after the finishing of first F&R cycle in the Figs. 5-8 (a) and (b), most of the amorphous structures have existed in the matrix of pure Zr, as demonstrated in Fig. 5-8 (c) and (d). Subsequently, the corresponding morphologies are found in the later ARB cycles and it is almost to be a full amorphous structure in the matrix from second to 13th cycles, as observed in Fig. 5-9, in addition to 14th cycle. In the 14th cycle, an uncertain re-crystallized Zr phase whose size approach to 2 nm is identified in the matrix, as indicated in Fig. 5-10.

5-1-3 The results of radial distribution function (RDF) calculations for Zr-Ni, Zr-Ti, and pure Zr

Figure 5-11 presents the partial radial distribution function (PRDF) after the ARB cycles indicated for the Zr-Ni system. From the first three PRDF profiles of each pair, it is evident that the microstructure have gradually transformed from the crystalline to amorphous phase. In the Zr-Ni alloys, the Ni atoms have fully transferred to amorphous till sixth cycles (see Fig. 5-11 (a)) but Zr atoms just need three cycles, as shown in Fig. 5-11 (b). The Zr side appears to vitrify faster is not surprising, since the Ni atoms are the more dominant moving species [63]. It appears that the FCC Ni crystals are relatively more reluctantly to lose their FCC packing nature. This trend has been observed experimentally by the X-ray diffraction and transmission electron diffraction that the FCC Ni crystal structure appears to the most stable phase and needs more ARB cycles to force it to transform into fully amorphous state [37-39]. Figure 5-12 reveals the variations of RDF from 6th to 12th cycles and their relative packing density of $Zr_{32}Ni_{68}$ alloy subjected to various F&R cycles. The RDF in Fig. 5-12 (a) exhibits sharper peaks at the 8-9th cycles, and the packing density is seen to increase as the appearance of nanocrystalline Ni phase at the 8-9th and 12th F&R cycles in Fig. 5-12 (b).

Figure 5-13 presents the partial radial distribution function (PRDF) after the ARB cycles indicated for the Zr-Ti system. Compared with Zr-Ni system, both Zr and Ti atoms need three cycles only to render the peaks of crystalline become smooth. The simulated RDF for the pure Zr at two rolling speeds is shown in Fig. 5-14. For the higher simulation rolling speed of 0.025 nm/fs (strain rate of 9.25×10^{9} s^{-1}), and still maintaining the ambient temperature, the RDF peaks for the ordered HCP structure is seen to gradually become more and more smooth, and eventually similar to the RDF similar to amorphous materials, as depicted in Fig. 5-14 (a). However, for the lower simulation rolling speed of 0.001 nm/fs (strain rate of 8.35×10^{8} s^{-1}), the HCP structure remains nearly unchanged from 1 to even 15 ARB cycles, as seen in Fig. 5-14 (b).

5-1-4 The average coordination number and potential energy for Zr-Ni, Zr-Ti, and pure Zr

The variations of the MD-simulated alloy potential energy (representing the atomic interaction enthalpy energy) with increasing F&R cycles are shown in Fig. 5-15. In Fig. 5-15 (a), the system potential energy for $Zr_{32}Ni_{68}$ starts to decline, or becomes more stable with unlike atom mixing, from the third F&R cycle due to the severe structure change during the transition period and becomes saturated at the sixth cycle. This results is consistent with the strongly negative mixing enthalpy of Zr-Ni (ΔH_m = -49 kJ/mol) that decreasing potential enthalpy energy leads to the lower Gibbs free energy of the mixed amorphous phase.

In contrast, the potential energy variation for $Zr_{50}Ti_{50}$ in Fig. 5-15 (b) does not show the similar trend. No obvious variation of potential energy in $Zr_{50}Ti_{50}$, because of the unique characteristic of the completely dissolubility between Zr and Ti atoms together with the near zero mixing enthalpy. The variation of potential energy of pure Zr alloys subjected to different F&R cycles for the lower simulation rolling speed of 0.025 nm/fs is shown in Fig. 5-16. The potential energy of pure Zr was raised to the level that for the metastable amorphous state after finishing the first F&R cycle and has since maintained the state during ARB processes.

Figure 5-17 presents the variation of average coordination number (CN) of Zr-Ni system for every cycle. For example, the profile of the CN for the Zr-Ni pair is referred to the case that Ni is the referenced atom and Zr is the first neighbor atom surrounding Ni. The coordination numbers of all pairs in Fig. 5-17 show a continuously decreasing or increasing trend until around the 6th cycle. When the mixed microstructure becomes finer and finer, the mixing and thus the interaction between Zr and Ni atoms become stronger, leading to the more apparent drop of potential energy from the 4th (-4.8 eV) to 6th ARB cycle (-4.9 eV), as indicated in Fig. 5-15.

In Fig. 5-18, the profile presents the variation of average CN of the Zr-Ti pair for every cycle is referred to the case that Ti is the referenced atom and Zr is the first neighbor atom surrounding Ti. The coordination numbers of all pairs also show a continuously decreasing or increasing trend until around the 6th cycle similar to the observations in Zr-Ni system. The drop in overall system energy is not apparent in the Zr-Ti alloy system (see Fig. 5-18), as compared with the previous Zr-Ni simulation, since the mixing enthalpy of Zr-Ti is intrinsically low. The variation of average coordination number (CN) of pure Zr system at two strain rates for every ARB cycles is shown in Fig. 5-19. There are slight cyclic fluctuations in CN of the higher strain rate condition but relatively smooth for lower one. However, the amorphous Zr shows a higher average coordinate number than crystalline.

5-1-5 The results of HA analysis for Zr-Ni, Zr-Ti, and pure Zr

For the Zr-Ni system

The more detailed local pairing variations with increasing ARB cycles for the Zr-Ni alloy are depicted in Fig. 5-20, respectively. Figure 5-20 (a) shows the evolution of the close-packed pairs of 1421 FCC-like and 1422 FCC/HCP-combined bond pairs in the Zr-Ni system. The 1421 pairs continue to decrease from the initial 54% to 25% until the 4th cycle and 1422 pairs does not reduce their population as fast as 1421 over this stage but also drop from 25% to 20%. Above the 5th cycle, both the 1421 and 1422 pairs appear to drop and then scatter at a low value of ~5%. It appears that the close-pack structures cannot be sustained in the Zr-Ni alloys after the 5th cycle.

In Fig. 5-20 (b), the 1541 icosahedra-defect and 1431 FCC-defect pairs in the Zr-Ni system have a finite amount existing in the first stage (~10% and 5%, respectively) and continue to rise or scatter to 15% and 20%, respectively. The 1541 icosahedra-defect pairs show a particularly wide scattering during the intermediate stage, from the lowest of 8% to the highest of 25% and with an overall average of ~15%. In contrast, the 1551 icosahedra pairs continue in their evolution from the initial less than 1% to 8% at the 4th cycle, and to 30% at the later stage. It seems that the icosahedra-defect and FCC-defect local structures are easier to form during the initial stage of the crystalline-to-amorphous transition processes.

From the above evolutions, it appears that the 1541 icosahedra-defect pairs are the intermediate transition atomic arrangement, and would transform gradually into the 1551 icosahedra pairs. The fluctuation between 1541 and 1551 pairs tend to approach to a more steady state till the 9th cycle, thus 1551 icosahedra pair structure is the more stable atomic local arrange in the current amorphous phase of the Zr-Ni system. Furthermore, an interesting phenomenon is evident in Fig. 5-20 (c) that the BCC related 1441 pairs will increase and then decrease during the amorphization transition processes. The other BCC type 1661 pairs and the rhombohedra-related 1321 pairs are also found, but the fractions of 1661 and 1321 pairs are consistently present with a low value ~5%.

For the Zr-Ti system

The detailed local pairing variations with increasing ARB cycles for the Zr-Ti alloys with an ARB rolling speed of 0.025 nm/fs are depicted in Fig. 5-21. The pairing variation of Zr-Ti shows basically smooth and steady evolution during the ARB cycles. The close-packed initial structures characterized by the 1421 or 1422 pairs continue to decrease from 50% to less than 10% in Fig. 5-21 (a). The overall percentage adding both 1421 and 1422 is about 20%. In contrast, the icosahedra and icosahedra-defect 1431, 1541 and 1551 pairs, characteristic of the amorphous phase increase lastingly from initial 0% to an overall 60% in Fig. 5-21 (b) for the Zr-Ti system. As shown in Fig. 5-21 (c), the BCC-related 1441 and 1661 pairs consistently occupy minimum amounts; while the icosahedra-accompanied 1321 pairs smoothly increase to 20%. The evolution sequence as a function of ARB cycles exhibits a simple trend. There seems no intermediate atomic pairing formed during the transformation from the HCP to icosahedra (i.e., the quasi-amorphous) structure, unlike the Zr-Ni system where a BCC-like intermediate pairing was seen.

For the pure Zr system

The detailed atomic pairing evolution of the pure Zr during ARB at two simulation speeds are shown in Figs. 5-22 and 5-23, respectively, for the higher and lower speeds. For the case of pure Zr at the high rolling speed, as shown in Fig. 5-22, the HA evolution trends resemble the trends seen in the Zr-Ti binary alloy. From Fig. 5-22 (a), it can be seen that the overall close-packed and ordered 1421 plus 1422 pairs continue to decrease from the initial 100% to overall 40% after 13 ARB cycles. At the same time, the amorphous natured icosahedra and icosahedra-defect 1431, 1541 and 1551 pairs increase continue to from the initial 0% to an overall 45% in Fig. 5-22 (b). The rest minor 1321, 1441 and 1661 pairs consistently occupy an overall 10% in Fig. 5-22 (c). The above result for pure Zr was simulated at a faster rolling speed of 0.025 nm/fs, the situation for the pure Zr at the lower simulation rolling speed of 0.001 nm/fs reveals a different story.

From the RDF curves shown in Fig. 5-14 (b), the HCP structure is resistant to be altered. This can be confirmed from the extracted HA index, shown in Fig. 5-23. Now, the overall close-packed and ordered 1421 plus 1422 pairs decrease from the initial 100% to only overall 70% after 15 ARB cycles, as presented in Fig. 5-23 (a). It means that the crystal structure of the pure Zr after 15 ARB cycles is still predominantly HCP. The amorphous-like icosahedra and icosahedra-defect 1431, 1541 and 1551 pairs together can only occupy 20%, as shown in Fig. 5-23 (b). The rest 1321, 1441 and 1661 pairs are basically negligible. The amorphization degree is very limited in this case.

5-2 The simulation results of vitrification transformation in Mg-Cu Thin Film

5-2-1 Morphologies of Mg-Cu during different temperatures

A series of atomic position projections in the interfacial layers during the structural evolution, corresponding to at 300, 413 and 500 K, are illustrated in Figs. 5-24 (a), (b), and (c), respectively. An inter-diffusion behavior occurred in the interfacial layers caused by the energy difference between Mg and Cu, resulting in the disorder-like structures in the Mg-Cu interfacial layers. The Mg and Cu atoms far away from their interfaces, which are not presented in the figure, are still retained the crystalline state during the processes. Compared with the Mg atoms which display a relatively uniform distribution in the interfacial layers, the Cu atoms are seen likely to congregate together forming a network distribution due to their higher binding energy than that of the Mg atoms, as shown in Fig. 5-24 (a). Subsequently, the regularly ordered clusters of the Cu atoms are gradually formed in the Mg matrix and approach toward the Cu-rich sides in Figs. 5-24 (b) and (c). The interfacial diffusion originated in the Mg/Cu disordered interlayer, however, does not further grow into their crystalline matrix even when the simulation is finished.

5-2-2 The results of density distribution profiles for the Mg-Cu

To define whether the amorphous structures have been formed in the interfacial layer in this sandwich model, the density profile of each species α along the *z* direction $\rho_\alpha(z)$, which can measure the number of α atoms within a certain distance interval along the *z* axis, is calculated to describe and quantify the mixing circumstances at each of interfacial region in this model. The density profiles $\rho_{Mg}(z)$ of the Mg atoms (red line) and $\rho_{Cu}(z)$ of the Cu atoms (green line) are shown in Fig. 5-25 for three different simulation states corresponding to Fig. 5-24. Figure 5-25 shows that the density profiles of the Mg and Cu atoms merge at the interfacial region, indicating the occurrence of mixing phenomena on the atomic scale. Some different species atoms in the interfacial region diffuse, indeed, in the areas over each other. The intermixing of Mg and Cu atoms at the interfacial region is not accompanied with the obvious local loss of crystalline order, although the thickness of the mixing areas present a well mixed and smooth distribution with increasing temperature.

5-3 The simulation results of cyclic loading fatigue in Zr-Cu binary amorphous alloy

5-3-1 The simulation results for $Zr_{50}Cu_{50}$ under different cooling rates

The volume versus temperature curves at different cooling rates, 1, 2.5, 5, and 10 K/ps obtained by quenching the sample model from 2000 to 300 K are shown in the Fig. 5-26. The glass transition temperature can be identified through the changes in the volume slope during cooling process. Figure 5-26 reveals only a slight difference among the T_g points (around 650 K) for four different quenching rates. The potential energies at their as-quenched state are about -5.237, -5.235, -5.233, and -5.232 eV and the average densities are 7.294, 7.293, 7.29, 7.287 g/cm^3, respectively. Because the difference of densities between 1 K/ps and 10 K/ps is 0.096%, the density is considered insensitive to the cooling rate for the Zr-Cu system. The similar trend is observed in their respective RDF curves. The PRDF of cooling rate 5 K/ps is shown in Fig. 5-27. The distinctly splitting phenomena occurring for the second peak among the $g_{Cu\text{-}Cu}(r)$, $g_{Zr\text{-}Zr}(r)$, and $g_{Cu\text{-}Zr}(r)$ curves of PRDF are similar to the results of Duan *et al.* [156], in which an amorphous phase was claimed to be produced under a cooling rate of 5 K/ps. For referring to literatures of other Zr-Cu simulations, the results for cooling rate of 5 K/ps would be used as the initial state for subsequent mechanical test simulation.

5-3-2 The mechanical properties of monotonic tension tests at different strain rates

Variation of potential energy

Figure 5-28 reveals the variations of potential energies for three conditions: one is using 5×10^9 s^{-1} strain rate to reach to strain of 20% (case 1), the second is using 5×10^9 s^{-1} to reach to strain of 30% (case 2), and the other is using 2.5×10^9 s^{-1} to reach 20% strain (case 3). The energies of case 1 and 2 increase from -5.233 to -5.227 eV when their reaching to 20% strains and that of case 2 keeps on rising to -5.226 eV at strain of 30%. The energy of case 3 increases from -5.233 to – 5.228 eV when reaching 20% strain. Apparently, high strain rate would induce a large steep slop of potential energy curve and a high energy state in Fig. 5-28. All three energy curves alter their slope to become smooth after passing through the 5% strain.

Variation of density

The density variations of three strain conditions are shown in Fig. 5-29. The densities of three cases decreases rapidly with increasing their strains from as-quenched state (7.29 g/cm^3) but approach to the respective saturation states after passing through 5% strains. The density in case 3 (7.26 g/cm^3) is slightly higher than those of cases 1 and 2 (7.255 g/cm^3). The decrease in densities from the initial 7.29 g/cm^3, is the evidence that the free volumes in three Zr-Cu amorphous models would increase during deformation. The amount of increase in total free volume in the simulation models is about 0.4% for case 3 and 0.48% for cases 1 and 2.

Stress-strain curves and local atomic strains

The stress versus strain curves for the above three conditions are displayed in Fig. 5-30. The σ_y is measured 2.2 GPa for the case 3 and about 2.4 GPa for the case 1 and 2, respectively. The Young's modulus for $Zr_{50}Cu_{50}$ metallic glass is fitted to be about 70 GPa, and the Poisson's ratio is about 0.43. There is a strain softening phenomenon appearing in the three cases after occurring yielding. Figures 5-31 (a) to (c) show the excessive atomic strain distribution of a slice parallel to the yz plane of the Zr-Cu amorphous alloy during and after plastic strains of 5, 10, and 30% under the monotonic tensile mode at strain rate of 5×10^9 s^{-1}. The strain of 5% corresponding to the position of σ_y on the strain-stress curve in Fig. 5-30 (a) shows that the initiation of STZs were induced by the irreversible local atomic strains (the green colors in Fig. 5-31) in the matrix and the total macroscopic strain of model has not depended on those irreversible local atomic movements yet. When the deformation of model gets into plastic deformation range, the STZ groups grow quickly and stochastically but not show an apparent shear localization (even under 30% plastic strain), as show in Figs. 5-31 (b) and (c).

The development of STZs in the condition of case 3 (see Fig. 5-32) is consistent with the observation in Fig. 5-31, and net-work organization composed of individual STZ groups is clearly indicated in Fig. 5-32 (c). The distribution of both figures of local atomic strains indicates no shear band forming in the current models even though they are applied under strain loading of 20 and 30%.

5-3-3 The results of structural analysis for different cyclic loading conditions

After 100 cycles of the tensile fatigue test under the stress-control mode at $\sigma_{max} = 2$ GPa, their PRDF curves for the $Zr_{50}Cu_{50}$ specimen in Fig. 5-33 did not show an apparent change during the whole deformation process, still similar to the as-quenched PRDF in Fig. 5-27. The case of the more severe strain-control tension-compression fatigue (even to 10%) still shows the same results. These results are interesting, since the specimen has been subjected to the severe local shear deformation under numerous fatigue cycles. The PRDF results indicate that structures of the $Zr_{50}Cu_{50}$ amorphous alloy still maintains in the liquid-like state, at least from the viewpoint of a medium range order, even when the alloy is subjected to the more severe strain-control tests.

The different HA indices for the compression and tension cyclic loadings under 1 GPa are shown in Figs. 5-34 (a)-(c) and 5-35 (a)-(c), respectively. Clearly, both the close-packed and liquid-like indices have an apparent fluctuation with the cyclic loading but do not show any continuously decreasing or increasing trend (like the trend shown in Fig. 5-20) throughout cycling, irrespective of the tensile or compressive mode. This trend means that the local structures with short-range ordering were indeed changed in response to the cyclic loading, but could be relaxed back to the amorphous state upon unloading or reversed loading. These detailed HA-pair analysis shown in Figs. 5-34 and 5-35 explains why there is no major change in the PRDF curves of Fig. 5-38. Although shear deformations are accumulated with increasing cyclic loading, it does not cause permanent structure transitions in the current Zr-Cu amorphous alloy. Similar behavior is also seen in Fig. 5-36, for the HA evolution in the most severe strain-control mode at $\varepsilon_{max} = 10\%$.

However, few crystal-like atomic clusters, such as close-packed or B2 structures, are indeed detected during the simulation process, as shown in Figs. 5-37 (a)-(c). Figures 5-37 (a) and (b) record the superimposed projections of close-packed atoms in the compression and tension at $\sigma_{max} = 1$ GPa during cyclic loading process and Fig. 5-37 (c) show those of the B2 atoms during the stress-control tensile mode at $\sigma_{max} = 2$ GPa. A blue particle indicates a FCC atom composed of its 12 near-neighboring atoms following -A-B-C- proper stacking sequence as shown on the top left corner of Fig. 5-37 (a), and a HCP atom is identified as green particle in the same figure similar to above method. The superimposed projections of B2 cluster is shown in Fig. 5-37 (c).

It is found that these crystal-like atoms always appeared near or within the shear transition zones (STZs), but not necessarily appeared at the places with the highest local strains. The appearance of the close-packed or B2 atoms is very interesting, because the formation of crystal-like clusters can be regarded as the precursors for the subsequent crystallization or the candidate of crystal nuclei [178]. Unlike the nucleation in quenched liquids, such ordered atoms in the simulated specimen did not congregate together to form larger clusters or keep on growing in the amorphous matrix. Instead, they simply appeared as an unstable state, and would appear and, then, disappear during cyclic loading. Throughout the simulation, such crystal-like atoms occurrences are rather rare, and did not have the ability to grow and form larger crystalline nuclei during the course of cyclic loading. The occasional occurrence of unstable local structures cannot result in the fatigue-induced crystallization in the current Zr-Cu amorphous alloy. This finding is in agreement with the fatigue studies of Zr-based BMGs.

5-3-4 Potential energies for different cyclic loading conditions

The comparison of potential energies between tension and compression of cyclic loading under stress-control at 1 GPa is shown in Fig. 5-38. Both energy curves show the continuously decreasing tendency with the evolution of time steps in Fig. 5-38 (a) that indicates the cyclic loading will influence Zr-Cu metallic glass going to a new steady state from the as-quenched condition. Although both decreasing amplitudes for tension and compression are very slight, the values of potential energy between tension and compression are approximately coincidence which indicates the same route occurring in this energy change between them. In Fig. 5-38 (b), the amplitude of potential energy of tensile mode has a higher fluctuation than that of compressive mode shows a better loading endurance for the compressive mode than the tensile one.

Figures 5-39 (a) and (b) are similar comparison of potential energies for the stress-control at 2 GPa. The potential energy for tensile mode is raised to - 5.231 eV from as-quenched state (- 5.233 eV) upon the first tensile loading cycle as a result of the stored deformation energy but gradually relaxes to - 5.235 eV at the end upon unloading (only 0.04% decrement as compared with the as-quenched state) with continuous cycling loading, as seen in Fig. 5-39 (a). Similarly, the amplitude of energy fluctuation for the compressive mode is smaller than that for the tensile mode but more evident than that for the case of stress-control at 1 GPa.

The comparison of potential energies between long and short periods for the cyclic stress-control at 2 GPa is shown in Fig. 5-40. The time steps for relaxation during the cyclic loading process for the case of long period is twice as much as the case of short one, as seen in Fig. 5-40 (b). Form Fig. 5-40, the variation of potential energy for the case of long period has the same way with short one, but just needs fewer loading cycles. In Fig. 5-40 (a), both energy curves show a change of their slope at the point corresponding to 500,000 time steps, and then become gradually saturated in later stages.

The comparison of potential energies between tension and compression of cyclic loading under strain-control at strain rate of 2.5×10^{10} s^{-1} is shown in Fig. 5-41. In Fig. 5-41 for the strain control mode, both energy curves show more apparent fluctuations due to the more severe strain amplitude. The energy suddenly increases to -5.224 eV for tensile and -5.226 eV for compressive mode upon the first loading cycle, and then gradually recovers to -5.234 eV as well as -5.232 eV, respectively, after cycle 12th and then keeps on this steady-state till the end upon unloading (only 0.02% decrement as compared with the as-quenched state). Unlike the observation on the stress-control cases, the energy curve of compressive mode reveals a higher value than tensile which indicates an more stable state could be easy raised under tensile mode.

Figure 5-42 is the comparison of potential energies of cyclic loading under strain-control among three different strain ranges. The loading condition of strain of 4% could cause larger fluctuation of energy amplitude than that of 2.5%, but the energy level of them is basically at the same range during the process of cyclic loading. In contrast, the energy state would be raise to a high level entirely when the loading condition for the strain-control was stretched to 10%.

5-3-5 Variations of density (dilatation) analysis for different cyclic loading

conditions

The results of density variation for the stress-control mode at σ_{max} = 1 GPa under tension and compression are shown in Figs. 5-43 (a) and (b). Generally, the average of density variation in Fig. 5-43 (a) does not show the pronounced change during the cyclic loading regardless of cyclic tension or compression. The density curves will increase or decrease with applying compressive or tensile stress but return to original density level when the applied stresses are released, as indicated in Fig. 5-43 (b). While applied tensile stress reaches to σ_{max} = 1 GPa, the density will decrease from 7.29 g/cm^3 to 7.30 g/cm^3 (about 0.14% decrement as compared with the as-quenched state). Similar behavior is shown in the compressive mode instead of increment in density.

While the maximum stress is, respectively, added to σ_{max} = 2 GPa for the tensile and compressive mode, both the amplitude of density variation for two these modes in Fig. 5-44 are raised higher than that for the maximum stress at 1 GPa in Fig. 5-43. The amplitude of density fluctuation for the tensile mode at σ_{max} = 2 GPa is about twice of that at σ_{max} = 1 GPa. For the compressive mode at σ_{max} = 2 GPa, the amplitude of density fluctuation approach to triple of that at σ_{max} = 1 GPa. However, the variation of average density does no show the difference with the results of σ_{max} = 1 GPa. Compared with the results of density variation between two loading periods in Fig. 5-45, there is almost not any difference existing between long and short loading periods under the tensile mode at 2 GPa.

Figure 5-46 is the comparison of density variation under strain-control mode at ε_{max} = 10% between tension and compression. The density for the tensile mode shows a greater decrease to 7.24 g/cm^3 at the first cycle but then gradually increase to 7.32 g/cm^3 at the end upon unloading (about 0.4% increment), suggesting a slight decrease in free volumes via variation of energy in Fig. 5-41 during fatigue loading. However, the density for the compressive mode in Fig. 5-46 does not show this slight increase trend till the end of cyclic loading. The variation of density almost maintain at a fixed range between 7.25 and 7.32 g/cm^3 during the cyclic compressive loading. The effect of different maximum strain under strain-control mode at cyclic tension is shown in Fig. 5-47. In Fig. 5-47, all of three density curves have shown a slight increase trend during cyclic loading process. The severer strain is applied, the higher density fluctuation is responded.

To further understand how the local strain can accumulate in the system without a significant overall density increase or decrease with shear band, it is interesting to observe the local free volume variation in space. Actually, the accurate measurement of free volumes in the metallic glasses is difficult. In this study, we use the method of the density profile to replace the notion of the free volume for simplicity even though it is just a rough expediency. The density profile in this system is just calculated by dividing the system into cubic boxes of an edge length of 4 Å. The blue-color sphere shown in the density profile indicates the lower-density region, i.e., with more free volumes. Figures 5-48 (a)-(d) exhibit the density profiles for specimens subjected to 12 and 25 cycles of strain-control tension-compression loading, showing the uniform distribution of the lower-density region. Overall, the density profiles in Fig. 5-48 suggest the semi-homogenous distribution of the free volume within the current $Zr_{50}Cu_{50}$ metallic glass under cyclic loading. The free volumes are exhausted at one place and rearranged at another place in the matrix. It is found that the localized free volume would contract and shrink into an equiaxed shape periodically when the system is loaded, and relaxed along a specific direction when the system is unloaded. The results of density profile for the other cases of cyclic loading show the same observation on their behavior of free-volume distribution and do not be shown in this dissertation.

5-3-6 The results of local atomic strain for different cyclic loading conditions

Figures 5-48 (a)-(c) show the excessive strain distribution of a slice parallel to the xz plane of the Zr-Cu amorphous alloy during and after 10, 30, and 50 tensile fatigue cycles under the stress-control mode at σ_{max} = 1 GPa. Figures 5-49 (a)-(c) show the same pictures of those local strains but under compressive fatigue cycles. The 2D sliced plots in Fig. 5-48 and Fig. 5-49 are extracted from our 3D simulation results for the ease of presentation. In these images, the green-color sphere indicates the higher strain levels, while the blue-color sphere indicates small (or zero) strains.

During cyclic loading, it can be seen that there are two kinds of deformation mechanism in atomic scale concurrently to dominate the deformation process. One is the plastic deformation with the reversible atomic rearrangement, and the other is the plastic deformation with the irreversible atomic rearrangement. The similar phenomenon is the reduction of the free energy around the deformed areas. From Fig. 5-48, most of individual excessive strains would accumulate with increasing cycle number. In the simulation result of Zink et al.[116], an individual STZ has been suggested to be 15 Å in diameter or so, corresponding to approximately 120 atoms in the CuTi glass model. In our simulation results, these irreversible-deformation atoms constructed the independent STZs distributed in the metallic glass stochastically at the early stages of the current simulation, as shown in Fig. 5-48 (a). At this initial stage, the STZs in Fig. 5-48 (a) with a higher strain level in a green color have a size about 10 - 20 Å, consistent with the finding of Zink et al.[116].

Hence, the irreversible events dominate the majority of the deformation and lead to the development of STZs under fatigue loading. With increasing loading cycles, the larger plastic-strain zone is originated from the connection of each individual STZ, as shown in Figs. 5-48 (b)-(c). The development of STZs is uniformly and dispersedly under this condition, and the shear localization is very unapparent in the matrix till the end of cyclic loading. These behaviors of initiation and evolution of STZs in cyclic compression at $\sigma_{max} = 1$ GPa is basically similar to their counterpart of cyclic tension, as seen in Fig. 5-49. Further, the evolution of STZs in both cyclic compression and tension seems to be very slow even till finishing fifty loading cycles.

The excessive strain distribution of the Zr-Cu amorphous alloy during and after 10, 50, and 100 tensile fatigue cycles under the stress-control mode at $\sigma_{max} = 2$ GPa is shown in Figs. 5-50 (a)-(c), respectively. Similar development of STZs is observed in the early stage in Fig. 5-50 (a), but self-organized into a larger network-like construction existing in the 3D space semi-homogeneously with increasing cyclic loading, such as the green color shown in Figs. 5-50 (b) and (c). Although these developments of STZs are generated and grew gradually in the matrix, the growth rate of shear deformation also appears to become slower in the medium and final stages as compared with that in the early stage under the stress-control mode at $\sigma_{max} = 2$ GPa, even reaching one hundred cycles, as depicted in Fig. 5-50 (c).

In the strain-control tension-compression model, the resulting excessive strain distribution of a 2D sliced plane appears to be much more severe due to the 10% strain level for each cycle, as shown in Figs. 5-51 (a) to (c). The apparently larger deformation events are formed by the connection and growth of STZs after several strain-loading cycles, as presented in Fig. 5-51 (a). Even so, the distribution of shear strains does not seem to lie along a specific direction (localization), even after finishing 25 loading cycles. The strain distributions are coincided with the phenomena observed in the stress control case at $\sigma_{max} = 2$ GPa. This result is different from the case of the uniaxial monotonic loading experiments during which the linear distribution of shear strains is localized along a specific direction (± 40 - 60^o) with respect to the loading axis [179]. Similar to the stress-control case shown in above, the progress of these excessive strains in the current fatigue case tend to, moreover, connect to form a network-like organization without shear localization existing in the 3D space semi-homogeneously with increasing cyclic loading, such as the red and orange color shown in Figs. 5- 51 (b) and (c).

Furthermore, the statistics of accumulating deformations in the stress control at $\sigma_{max} = 2$ GPa and strain control at $\varepsilon_{max} = 10\%$ can help understand the growth behavior of flow defects during the cyclic loading. The numbers of deformed atoms in the stress control mode, which are in green color in Fig. 5-50, are gathered in Fig. 5-52 (a). The deformed atom number rises quickly in the early stage and becomes gradually saturated in later stages. This tendency corresponds well to the observation in the sliced plots in Fig. 5-50, with apparent difference in STZ numbers between Figs. 5-50 (a) and (b) but minor difference between Figs. 5-50 (b) and (c); the development of STZs seems to be saturated after ~50 cycles. The similar phenomenon also occurred for the strain control case, as shown in Fig. 5-52 (b). The deformed atom numbers in the severe strain control simulation is obviously higher than the stress control mode. The gradual saturation tendency of the deformed atom numbers or the growth rate of plastic flows, with increasing cycles implies a resistance against the further development of STZ groups once the accumulating deformation reaches a specific level during the cyclic loading.

5-3-7 The stress-strain curves for different cyclic loading conditions

Figures 5-53 (a)-(c) are the stress-strain curves for 2.5%, 4% (nearly elastic regime) and 10% strain (highly plastic regime) for the strain-control modes, respectively. The curves in

Figs. 5-53 (a) and (b) are basically within the elastic range and are similar to the stress control results, exhibiting a nearly linear relation to applied stress. It also means the energy input from the applied stress is fully loaded and unloaded in each cycle. Contrarily, the stress-strain curve in Fig. 5-53 (c) shows a mechanical hysteresis; the cyclic deformation curve can be divided into four parts: tensile loading, tensile unloading, compressive loading, and compressive unloading. The energy loss during loading and unloading suggests that there have some activities occurred, such as long-range atomic movement or dynamic relaxation/recovery in the Zr-Cu amorphous alloy.

Chapter 6 Discussion

6-1 The phase transformation in Zr based intermetallic alloys during ARB

6-1-1 The transformation of Zr-Ni from nanocrystalline to amorphous phase during ARB

Before discussing the local cluster structures and its structural transformation in this system, it is helpful to examine their equilibrium phase diagram first [180], as depicted in Fig. 6-1. The heat of mixing between HCP Zr and FCC Ni is -49 kJ/mol, which would lead to a strong driving force for the pure elemental Zr and Ni atoms to mix together and to form local ordering. Coupled with the large difference in the atomic radius, r, being 23 % judging from $r_{Zr} = 0.160$ nm and $r_{Ni} = 0.124$ nm, the Zr-Ni system has been considered to be a binary alloy with high glass forming ability upon rapid cooling. The strong tendency for local ordering results in the formation of many equilibrium intermetallic compounds, including Zr_2Ni, ZrNi and Zr_2Ni_7.

From the microstructural evolution and associated two-dimensional Fourier transform shown in Chapter 5-1-1, the vitrification of FCC Ni proceeds relatively more reluctantly than that of HCP Zr in Figs. 5-2 (a) to (c). Undeniably, this could be directly relative to the nature of characteristic between FCC and HCP structures. There are 12 octahdral slip systems for FCC metals competed with those for HCP. Also, the smaller atomic radii and mass of Ni compared with Zr would provide more atoms within a specific space, namely having higher number density than Zr in the same grain size. Both factors let it possess higher diffusion mobility and more alternative than Zr atom to quickly restore crystalline while being borne the same condition at high strain rate. On other hand, reduced grain size would lead to the unstable state within grain, e.g. the competition between their surface energy and volume energy in the classic nucleation theory. Hence, FCC or HCP crystals would collapse its long range order rapidly and transfer to short range order clusters when reducing its grain size to a critical value, but Ni could maintain this long range order better than Zr in the same space of their small grain size due to its small atomic radii.

The results of potential energy and HA index both show a pronounced transience at the early stages of ARB cycle. It is well known that one of easier forming compounds in the Zr-Ni alloys is Zr_2Ni, which has a body centered tetragonal (BCT) crystalline structure with lattice constants of a=0.65 nm and c=0.53 nm. Other intermetallic compounds include $ZrNi_5$ (cubic), Zr_2Ni_7 (monoclinic), $ZrNi_3$ (hexagonal), Zr_7Ni_{10} (tetragonal), ZrNi (orthorhombic), etc, based on the equilibrium thermodynamic phase diagram in Fig. 6-1. In general, it prefers to form the intermetallic compounds rather than an amorphous phase through the thermodynamics route. However, there is no information on the relative ease of forming these intermediate phases during the rapid and meta-stable processing of severe deformation at high rates. During the course of ARB under severe shear stress, the induced transient atomic local structures appeared in Fig. 5-20 (c) might be any one of these candidates. But the transient atomic structures might be deformed and deviated from the equilibrium phase structures. Because all intermetallic compounds of Ni-Zr have very complicated crystal structures with unit cell space over 100 cubic angstroms, the complicated Ni-Zr intermetallics require a abundant amount of time to be created [63]. The observed local geometry of 1441, 1661 and 1321 should be associated with such intermediate phases.

By closer examinations of the simulated structures in HA analysis of Zr-Ni, most atoms classified as the 1441 pairs are the Ni atoms, implying that the local geometric structures of the 1441 pairs is one of BCC-like short range ordering (or deformed BCC). This BCC-like pairs seem to be the transient atomic arrangement for the FCC structure to transform into the final amorphous phase. It is not clear whether this local atomic pairing is originated from the local formation of the BCT Zr_2Ni or the cubic $ZrNi_5$. But it is evident that the transition of the FCC Ni crystals in the current Zr-Ni system will pass a transition stage forming local atomic pairs other than face centered cubic. The evolution of the local pairing structures appears to be rather complicated.

A similar observation of the above transient pairing has also been reported in the MD simulation for the rapid cooling process of Cu[32, 159], where the 1441 and 1661 pairs would have a sudden fluctuation during glass transition. Unlike the process of supercooling where the glass transition is continuous; the amorphization during the current ARB cycle is formed by the strain-induced atomic mixing mechanism during each rolling cycle that will result in a more discrete structure transition than that occurring during supercooling. It follows that the fluctuation phenomenon of the 1441 pair becomes more obvious. Also, the recent simulation work on the rapid quenched Zr-Cu-Al bulk metallic glasses by Fan et al. [94] has also found the involvement of the BCC Zr-Cu structure.

It is noted that the simulated curves of Zr-Ni in their PRDF and coordinate average are basically stable after the 5^{th} cycle. However, the extracted populations of the local HA pairs still show evident fluctuations in Fig. 5-20. This provides more detailed information on the local short-range order structure transitions which cannot be observed from the RDF, average potential energy, or coordination number.

6-1-2 The transformation of Zr-Ti from nanocrystalline to amorphous phase during ARB

In the Zr-Ti system, all of analysis results indicate the vitrification is fairly quickly for Zr-Ti during ARB process. Although this tendency is consistent with the observation in experiment [37-39], the reality of their mechanism is still questionable. This refers to the nearly zero for their mixing heat between Zr and Ti and not large difference, only 8%, of atomic radius between tow species (r_{Zr}=0.160 nm and r_{Ti}=0.148 nm) compared with Zr-Ni system. Zr and Ti are both of the hexagonal close-packed (HCP) structure in addition. For the above characteristics, the Zr-Ti binary system can form an isomorphous phase diagram without any intermetallic compound, but not be considered possessing a high glass-forming ability according to the experimental rules in Chapter 2-1.

The Zr-Ti equilibrium phase diagram [181] is shown in Fig. 6-2. No obvious variation of potential energy in $Zr_{50}Ti_{50}$, because of the unique characteristic of the completely dissolubility between Zr and Ti atoms together with the near zero mixing enthalpy. It appears that the faster mixing of unlike atoms in $Zr_{50}Ti_{50}$ is not a result of the potential or mixing enthalpy, but is due to the same HCP structure and the compatible initial hardness for Zr and Ti. The (0002) basal planes of both Zr and Ti lying on the rolling plane could be effectively sheared through with each other, accelerating the thickness reduction and atomic mutual mixing under current high strain rate.

Based on evolution sequence of HA analysis, there is no intermediate atomic paring (like BCC-like pairing detected in Zr-Ni system) formed during the transformation from HCP to amorphous phase. This results suggests that even with the isomorphous Zr-Ti phase diagram nature, this binary system can still be vitrified through the solid state ARB processing at room temperature, consistent with the experimental findings as well[37-39]. The solid-state roll-bonding can offer another alternative for systems such as isomorphous Zr-Ti to form amorphous alloys, which can transform the HCP crystalline phase into complete amorphous state in a smooth sequence. During the course of atomic structure transformation, the initial fully ordered atomic close packing (100% of 1421 or 1422 pairings) can be destroyed to occupy only 20% of the overall atomic pairings. Concurrently, the much more random icosahedra and icosahedra-defect 1431, 1541 and 1551 pairs for the amorphous structure gradually become the dominant fraction of ~60%.

6-1-3 The transformation of pure Zr from nanocrystalline to amorphous phase during ARB

Since the Zr and Ti are highly similar elements with the same crystal structure, similar atomic size, hardness and melting point, and both locate on the same IVB column in the Periodical Table, they actually act as twins in many ways. Following the above scheme, it is interesting to ask whether the pure Zr (or Ti) element itself can be vitrified by itself during the same ARB route at room or cryogenic temperatures. There have been a few attempts [67] to transform the crystalline pure element into the amorphous state, using torsion or ball milling, though the results are still controversial. In our experimental study, the trial using ARB experiments on the pure Zr multi-layers still could not achieve the amorphous phase as the X-ray results shown in Fig. 6-3. This was due to the fact that the applied rolling speed is too low and working temperature is still too high for the pure element to vitrify.

On the other hand, when we adopt the more rapid ARB rolling speed and liquid nitrogen to cool the rolled specimens, the ribbons become too brittle to be rolled repeatedly. The experimental difficulty prevents from the vitrification of pure Zr. However, using the same

MD simulation method, but replacing the Zr and Ti bi-layer to two pure Zr layers and running the rolling at two rolling speed of 0.001 and 0.025 nm/fs, the result might be stimulating for future experiments.

The HA evolution sequence as a function of ARB cycles for the rolling speed of 0.025 nm/fs exhibits a simple trend, similar to but not exactly the same as the Zr-Ti case. It appears that the vitrification degree of the pure Zr is consistently inferior to Zr-Ti. For example, the ordered 1421 plus 1422 pairs of Zr-Ti can be easily dropped to a minority of 20% after 10 ARB cycles, but the 1421 plus 1422 pairs of pure Zr only decrease to 40% (i.e., still a sizable portion of the persistent HCP pairing). Also, the icosahedra and icosahedra-defect 1431, 1541 and 1551 pairs, with the amorphous-like nature, can occupy ~60% in Zr-Ti, but occupy only 45% in pure Zr.

From the HA index evolution, the pure Zr seems to have the possibility to be vitrified, provided that the ARB rolling speed is sufficiently high and the working temperature is remained to be around 300 K. Experimentally, this is difficult to achieve, since the working temperature tends to rise more with increasing rolling speed. An appropriate cooling technique is necessary. Meanwhile, due to the large gap of the time scale involved in the MD simulation and real experiment, there is always room for questioning the current results (note that the rolling speed in MD is in the range of 10^{-2} nm/fs and the experimental rolling speed is around 10^{1} mm/s, or 10^{-8} nm/fs). Nevertheless, it is demonstrated by MD simulation that, under proper cooling and relative faster rolling speed, the crystalline pure Zr element could be able to transform into the amorphous phase. This is demonstrated by both the RDF curves and the HA index. Future experimental improvement is needed to justify the simulated results.

Here must be noted that the strain rate between two rolling speeds, 0.001 nm/fs (8.35×10^{8} s^{-1}) and 0.025 nm/fs (9.25×10^{9} s^{-1}) is just about 1 order, but present the very distinct results. It could very close in a critical strain rate for the phase transformation between crystalline and amorphous phase. Supposing to ignore the thermal activation generated by severe shear stress during deformation, vitrification can be viewed as a result of competition of stability between long and short rang order, similar to the condition in rapid cooling. When the strain rate is lower, the created defects can be always rearranged and annihilated to maintain the stable-state for crystalline in long range order, just like behaviors shown in Figs. 5-5 to Figs. 5-7. In contrast, when a strain rate is provided high enough to restrict the rearranged period for crystalline phase, a metastable state in short range order is preferred to create for metal atoms within very short deformation period.

6-2 Vitrification transformation in Mg-Cu thin film

As the Mg-Cu equilibrium phase diagram, is presented in Fig. 6-4, implying a possibility of interface reactions of the Mg-Cu intermetallic phases formed in the Mg-Cu multilayer. There are two intermetallic compounds can form in the Mg-Cu system. In the Cu-rich side, Cu_2Mg is a quite stable phase existing in the Mg-Cu system because the radii of major Cu atoms (1.28 Å), is smaller than surrounding Mg atoms (1.6 Å), which results in a greater packing fraction to form a Laves phase. In the Mg-rich side, a complex competing crystalline phase, Mg_2Cu, can exist in the Mg-Cu system, where the larger atoms is majority. Mg_2Cu is an orthorhombic structure but is not as stable as Cu_2Mg. For glass formation in the Mg-Cu system, the thermodynamic calculations and experiments [182, 183] indicated that the glass favor forming over the composition range of 12-22%Cu, including a lowest eutectic point at 14.5%Cu. Thus, it is expected that the amorphous phase or the Mg_2Cu phase have the chance to form in the lower temperature conditions.

However, it must be recognized that the amorphous structures have not been generated by MD simulation in this sandwich layers yet, even though higher temperature had been used to offer more kinetic energies for atoms. This may be caused by the employed NVT ensemble that constrained the space on the x and y plane, resulting in a lower degree of freedom for atoms to change their positions extensively in all directions. However, the Mg-Cu amorphous alloys are also difficult to produce by experiment in our laboratory [184]. A transmission electron microscopy (TEM) image of the Mg-Cu multilayer system produced by sputtering is given in Fig. 6-5. The bright zone is the Mg layer with a thickness of 150 nm, and dark zone is the Cu layer with a thickness of 50 nm. The Mg_2Cu compound structure was found in this multilayer system when this specimen was annealed at 413 K, as shown in Fig. 6-5. The structural transformation of the specimen during annealing at 413 K is also shown in the X-ray diffraction pattern. The strong peaks at 19.5^o and 39.6^o imply that the Mg_2Cu phase gradually forms along with a decrease of the Cu and Mg peaks.

In contrast, the MD simulations do not show the production of intermetallic compound, Mg_2Cu phase, in the current model. This does not only correlate to the constraint of necessary space for phase transformation due to ensemble condition but also relate to the availability of MD method applied on study of nature of diffusion behaviors. It is well known that the diffusion mechanism is a strongly time-dependent behavior with atomic movement. When being in high temperature over melting, the thermal kinetic is high enough for animated the inter-diffusion behavior between two kind of different species. This behavior is presented in the simulation of Mg-Cu under a simple NPT ensemble at an artificial temperature of 2000 K (not shown in this dissertation), but not show in low temperature conditions. This means that studying diffusion behavior in MD method will need much longer time period. Hence, choosing the Monte Carlo method instead of MD might be suitable for this topic.

6-3 Cyclic loading fatigue in Zr-Cu binary amorphous alloy

6-3-1 The crystallization in cyclic loading fatigue

Generally, the shear-band initiation and propagation during the severe deformation test would result in the structure transition within the amorphous alloys [185], so that some nanocrystallization might be induced along the shear bands. It is of concern whether there would also be any crystallization phenomenon occurred under the cyclic loading as seen in the uniaxial-monotonic loading because the fatigue crack is ordinarily easy to initiate from the sites of those nano-crystals in the BMG. The Zr-Cu equilibrium phase diagram in Fig. 6-6 refers a possibility of intermetallic phases formed in the Zr-Cu system[186]. For real ZrCu at a 50-50 composition according to this diagram, the B2 structure is the stable structure at higher temperatures; it transforms to a B33 structure at lower temperatures, but that will be rather similar to the B2 structure. Few B2 structures are identified in these cyclic loading simulations regardless of stress or severe strain-control mode but those can barely grow into the crystalline phase in progress, as seen Fig. 5-37.

In general, local heating of shear band is viewed as one of cause of crystallization in metallic glass; significant temperature rise in shear may offer enough thermal activation to drive the crystallization. But this viewpoint is not exactly available to our simulation results based on the applied isothermal condition which blocks the possibility of severe temperature change in the system. Hence, the appearance of local ordering phase is a result of another possibility that is strong shear flow enhances atomic mobility and induces the nanocrystalline phase forming in the shear band.

On the other hand, the nucleation is a time-dependent behavior at different temperatures, e.g., the time lag for nucleation would increase with decreasing temperature at low temperatures. Therefore, if those local ordering structures in Zr-Cu metallic glass can not be in an enough long time, the crystallization is almost impossible to occur from them. Apparently, in spite of strong shear flow applied from cyclic loading in different conditions (including loading amplitude, period, and strain rate), the circumstance for nucleation is also altered in each progress, and resulting in only repeated appearance and disappearance of those ordering structures.

6-3-2 The structural relaxation in cyclic loading fatigue

Instead of no phase transformation in $Zr_{50}Cu_{50}$ metallic glass during cyclic loading in this work, the structural behaviors observed from HA pair index during cyclic loading are always in a periodical fluctuation that indicates the domination of structure properties in its cyclic loading fatigue is straightforward structural relaxation. Another evidence is the observation of potential energy variation, which always shows a decrease tendency with increasing loading cycles. Structural relaxation plays an important role that would lead the metallic glass to transfer to lower energy states in the potential energy landscape through the atomic motion when annealing at a high enough temperature, but insufficient for crystallization. The simulation results of HA analysis and potential energy variation apparently prove the structural relaxation can be driven by mechanical method, which can provide enough atomic kinetics to leap over the energy barrier for next metastable equilibrium.

It is difficult to understand the details of structural relaxation through the current HA pair method which only shows the statistics of fraction of simple geometry in short range order. But properties of both potential energy and density can reveal some information about the factors of structural relaxation in cyclic loading fatigue. Based on the potential energy results of cyclic loading, it suggests there exists an ideal glass state for a special chemical component, and this ideal glass state could be directly related to its cooling rate. The true phase of the ideal glass state is unclear so far, but can be approached through the repeated structural relaxation by annealing at higher temperatures or mechanical cyclic loading. In the stress-control, it suggests the route to the saturated state (semi-ideal glass state) for structural relaxation is basically in agreement. But increasing loading amplitude helps to shorten the approach time, and extending loading period reduces the cycles for structural relaxation to reach its saturated state.

Furthermore, the tension mode can cause larger dilatation fluctuation than compression one; the $Zr_{50}Cu_{50}$ metallic glass shows a better resistance for structural relaxation under compression than tension. However, if the applied cyclic strain is large enough to go into plastic range (e.g. ε_{max} = 10%), the saturated state will be higher than that of applied strain within elastic range. There exists two ways in the cyclic loading fatigue. One is to raise its internal energy state within the glass matrix, leading to accumulation of damage to failure finally. Apparently, adding a severe applied strain into plastic range will drive to this tendency, as demonstrated in Fig. 5-42. The other way is to lead the cycled MG to a lower energy state. The current results show that structural relaxation can induce recovery in the energy state.

6-3-3 Microscopic deformation in cyclic loading

The results of local atomic strain show a homogeneous deformation in the monotonic and cyclic loading. In the monotonic loading cases, the domination of macroscopic strain attributes to the accumulation of irreversible atomic rearrangement. A number of STZ group does not rapidly evolve until exceeding overshoot of stress at the applied strain, ε_{max} = 5%. In the cyclic loading case, not only irreversible local shear evens which still dominate the accumulation of local strain but also reversible local elastic deformation affect the development of deformation behaviors in metallic glass.

Generally, the homogenous shear flow in metallic glass typically occurs within supercooled liquid region at high temperatures near the T_g point and provide a well plastic deformation properties. In experiments, most of the metallic glasses show the inhomogeneous deformation with the shear banding mechanism due to the shear localization at high stress concentrations and lower temperatures. In the results of this simulation, the STZs can initiate stochastically and organize to a network-like development in the glass matrix either in monotonic or cyclic loaing in time and space but do not localize. Localization in metallic glass is believed relative to local increase in free volume (positive dilatation), evolution of structure order, stress redistribution, or local heat generation [112]. In the density variation of monotonic loading, the increase of dilatation providing sufficient space for occurrence of a number of plastic flows is indeed observed before going into the plastic region, and plastic shear flows also increase rapidly and lastly in the plastic region. Hence, the difficulty in generation of shear band or localization may be a result of the space limitation in the current model size. It restricts the essential volume for developing a mature shear band, but can exist in a number of STZs groups (embryo shear bands) instead. On the other hand, the small model size will make the redistribution of internal stress or free volumes more easily and quickly in space and add difficulty in shear localization or stress concentration.

In the cyclic loading, the homogeneous deformation in metallic glass is associated with irreversible and reversible atomic rearrangement which are co-exist but account for different percentage in glass matrix during cyclic loading process. When suffering severe deformation initially, the irreversible local strains will take most percentage in the glass matrix to release the strain energy and gradually take place of the reversible local deformation. Here extends another issue about the anelastic which is a time dependent elastic behavior in metallic glass but not be well studied in the current works yet. Hence the accumulation of local strain tends to be slow once a balance between two kinds of local atomic strains is achieved in the progress of cyclic loading. Combining with observations in potential energy and density state, it suggests that the behaviors of atomic strains are strongly associated with structural relaxation of metallic glass. The accumulation of local plastic deformation does not go toward failure with increasing energy state and free volumes in metallic glass but, instead, to a steady-state with a lower energy state like the deformation behaviors in homogenous plastic flow.

6-3-4 The phenomenon of dynamic recovery

It is noted that the stress cycles would differ for the elastic and plastic regimes. Therefore, we have conducted simulations for the strain control mode to three different maximum strain levels, namely, 2.5%, 4% and 10% strain. Figures 5-53 (a), (b) and (c) are the stress-strain curves for 2.5%, 4% (nearly elastic regime) and 10% strain (highly plastic regime). The curve in Fig. 5-53 (a) is basically within the elastic range and is similar to the stress control results, exhibiting a nearly linear relation to applied stress. It also means the energy input from the applied stress is fully loaded and unloaded in each cycle. Contrarily, the stress-strain curve in Fig. 5-53 (c) shows a mechanical hysteresis; the cyclic deformation curve can be divided into four parts: tensile loading, tensile unloading, compressive loading, and compressive unloading. The energy loss during loading and unloading suggests that there have some activities occurred, such as long-range atomic movement or dynamic relaxation/recovery in the Zr-Cu amorphous alloy.

In the crystalline materials, dynamic recovery proceeds mainly via the rearrangement of dislocations cell walls or subgrain boundaries. And dynamic recovery occurs more easily in metals with high stacking-fault energy. In amorphous structures, local atoms suffered shear deformation could result in stacking-fault-like energy [128, 129], and the derivative of this stacking fault energy could become the resistance traction to hold back the highly localized shearing in the metallic glass. This event could cause the local instability of the deformed atomic clusters, and thereby dynamic recovery could be induced to occur via the mutual activation of STZ groups that are discretely generated by the cyclic deformation. This behavior is similar to the model of reversible/irreversible structural relaxation of metallic glasses [24, 25, 187, 188], but it is nearly diffusionless, different from the thermal recovery caused by structural relaxation in high-temperature annealing or creep. The cyclic deformation at room temperature can also provide mechanical-energy input for the relaxation reaction.

The self-repairing structural relaxation and dynamic recovery of metallic glasses under cyclic loading is proposed below. When an amorphous structure is achieved by quenching, it may be composed of icosahedral local short-range ordering, network-forming clusters medium-range ordering, and other unidentified-random local structures [23, 24]. With the complex atomic packing, there are some places that are more easy to undergo structural relaxation (i.e., with a higher degree of loose bonds or free volumes), termed as the relaxation centers (RCs) in the metallic glasses [187, 188]. Some of them are regarded as the reversible relaxation centers (RRCs) and others irreversible relaxation centers (IRRCs). The distribution and organization of such relaxation centers are believed to be sensitive to cooling rate.

The RRCs are inherent with a more symmetrical potential barrier state in space, as depicted in Fig. 6-7 (a). When the local atoms around RRCs are subjected to local shear stress, atoms are separated from their original positions into a new atomic arrangement. The energy states of the original and new atomic arrangements are both at the similar semi-stable level, and parts of new atomic arrangements belonging to RRCs tend to recover back to their original atomic arrangement state upon the applied stress is relieved or during reversed loading. Such atomic arrangement back and forth is reversible, and occurs predominantly when the applied fatigue stress/strain is small and within the elastic regime, for example, in the stress or strain control mode to around 2-2.5% strain. The fatigue-loaded Zr-Cu metallic glass, though subjected to long-cycle fatigue, still behaves undamaged, as if there have been local self-repairing dynamic recovering mechanisms during cyclic deformation.

On the other hand, The IRRCs are inherent with an asymmetrical potential barrier state, as shown in Fig. 6-7 (b). Parts of atoms belonging to IRRCs, under shear stress, would like to jump into a more compatible and stable state (with a lower energy) while the other atoms go to fill a vacant free volume. The occurrence of such irreversible plastic events would lead STZs to keep on accumulating and growing gradually inside the amorphous material. Such local plastic events during structural relaxation/recovery would benefit the annihilation or removal of defects (e.g. free volume) by moving the system toward a more stable state at each cycle. Such a new atomic arrangement possesses a tighter bonding. Since the new atomic arrangement is in the lower energy state, it is unlikely to return back to the original arrangement, behaving as irreversible relaxation. This behavior can be viewed as a self-repairing dynamic recovery process that the defects induced in the previous cycle could be eliminated in the subsequent cycle. This self-repairing dynamic recovery phenomenon during cyclic loading also results in the temporary appearance and disappearance of local STZs, reducing the tendency for massive STZ pile-up to form a damaging macro shear band.

The current simulation results suggest that the metallic glass in small size-scale can be quite fatigue resistant. The metallic bonds in the metallic glasses, once broken by local shear stress, can be self-repaired and re-bonded to neighboring atoms by the subsequent reverse shear stress. Such a dynamic recovery capability is particularly significant in fatigue loading. For applications of the metallic glasses in micro-electro-mechanical systems (MEMS)[189], the current finding is encouraging.

6-3-5 Fatigue softening or hardening in current model

It is of interest to examine whether the cyclically-loaded specimen in this work would exhibit fatigue softening, hardening, or constant strength during the course of cyclic loading. Crystalline materials have shown all these three kinds of behaviors, depending on the materials nature and the loading conditions. The current Zr-Cu metallic glass is found to show a slight cyclic-softening behavior, particularly for the initial stage upon the first cycle, as shown in Fig. 6-8. For the stress-control tension fatigue, as shown in Fig. 6-8 (a) at $\sigma_{max} =$ 2 GPa, the induced strain gradually increase from the 2.8% strain upon the first tension cycle, then to a 3.6% strain after 25 cycle, to a 3.9% strain after 50 cycles, and finally to a 4.1% strain after 100 cycles. It appears that the amorphous Zr-Cu alloy was soon softened upon the initial cycling stage and gradually reaches a semi-saturated state.

For the more severe tension-compression strain-control fatigue, as shown in Fig. 6-8 (b), the measured stress decreases appreciably from 3.0 GPa for the first cycle, to 2.5 GPa for the second cycle, and fluctuates within 2.5 to 2.7 GPa during the subsequent cycles. It seems that the severe first-cycle loading has induced a certain amount of defects or free volumes in this case, causing the initial softening. The following cycling loading does not render further fatigue softening after first-cycle loading. The induced defects or free volumes would be dynamically recovered, lessening the fatigue softening. Overall, the current Zr-Cu metallic glass, in small size-scale, appears to exhibit only minor fatigue softening.

6-4 Short discussion on the comparison of MD simulation and experimental results

The studies in this dissertation composed of three MD simulation works, namely phase transformation in ARB, diffusion properties in Mg-Cu thin film, and mechanical properties in cyclic loading. Although we always try to make a comparison with experimental data directly, it does exhibit significant discrepancy between MD simulations and experiments. One of main fact is an incredible difference in their time scales which always leads us to get no sense on applied strain rate. For instance, the rolling strain rate for Zr-Ni system is about 0.4-0.8 s^{-1} for each rolling cycle in our ARB experiment but about 10^{11} s^{-1} in simulation. This is due to the nature of MD theory. The vibration frequency of a atom is generally about 10^{10}-10^{13} s^{-1} , and hence it should be chosen to describe its dynamics under this small time scale, commonly being 10^{-15} s. Under this time scale, it can never approach the macroscopic scale regardless of much longer time steps we can use currently. Therefore, it could appear the amorphous phase at 40th ARB cycles in the experiments but just need 3~6 cycles to perform the same thing in simulation. This is not strange if we want to study something through such category of methods. We must, however, take notice of necessity of applied high strain rate in MD that chosen deformation speed can not exceed the speed of internal stress wave in the model. It will be better to choose a strain rate that can permit a steady-state of stress wave transmission exhibiting in the MD model.

On the other hand, the limitation of model size is always a barrier to challenge the computer load and work efficiency such as the works of ARB process and cyclic fatigue in this dissertation. How to get a reasonable physical picture within calculated ability is very important for designing a MD work. For example, we can design a plan model which provides a relative large space only in one or two dimensions to accommodate the critical space of a mature shear band, to take place the current model which used a relative small space in three dimensions in cyclic loading work but both tow models have the same computational efficiency. Therefore, we will have high possibility to perform a macroscopic mechanism under finite simulation resource. General speaking, the main advantage of MD simulation for us is to understand or obtain the qualitative characteristics in atomic behaviors, not focusing on the accuracy of computed values.

Chapter 7 Conclusions

In summery, the local atomic pairing arrangement of the binary Zr-Ni, Zr-Ti, and pure Zr systems during room temperature severe deformation under high strain rates is simulated by MD method. The following conclusions can be reached from this part of study.

(1) For the Zr-Ni system, the local defect structures of the FCC Ni and HCP Zr, or the icosahedra clusters are seen to form first in the early stage of the amorphous transition, and the FCC 1421 or FCC/HCP 1422 close-packed pairs would decay rapidly at the same time.

(2) For the Zr-Ni system, the icosahedra defect local structures, or the 1541 pairs, will first evolve and then transform into the more stable icosahedra clusters, or the 1551 pairs. The three types of pairs, namely the 1551, 1431, and 1541 pairs occupy totally ~70% of the total pair population. The rest are the remaining FCC or HCP (1421 or 1422, accounting for ~15%) and the intermediate local structures (1441, 1661 or 1321, accounting for another ~15%).

(3) During the transient stage for the Zr-Ni system, the BCC-related cubic-typed 1321 pairs are formed up to 20%, which may be related to the intermetallic compounds that will form according to their equilibrium phase diagram. But this transient atomic pairs would disappear at the later stage. In addition, the FCC Ni seems to be more difficult to change into the amorphous phase than the HCP Zr, judging from the PRDF curves. And the FCC local pairing appears to change to the BCC-typed pairing before transforming into the fully amorphous state. The structure transition mechanism of the FCC seems to be more complex and more persistent than that for the HCP structure.

(5) With the same HCP crystal structure for both Zr and Ti, the transformation in the Zr-Ti system is basically simple. No apparent transient atomic packing is formed in the intermediate stage. The icosahedra-related atomic pairs occupy nearly 80% in the later stage.

(6) The current simulation results reveal that the short-range icosahedra structures always play an important role during the course of crystalline-to-amorphous transition, both during the solid state strain-induced ARB and rapid cooling processes.

(7) Finally, it is demonstrated by MD simulation that, under proper cooling and relative faster rolling speed, the crystalline pure Zr element should be able to transform into the amorphous phase. But there exists a critical strain rate for the phase transformation between crystalline and amorphous phase. Below this critical strain rate, the created defects in metallic matrix can be always rearranged and annihilated to maintain the stable-state for crystalline in long range order without vitrification.

In the part of MD study on the diffusion behaviors between incoherent interfaces of the Mg-Cu system, the structural transition of Mg-Cu multilayer annealing at three temperature conditions had been studied by employing EMT potential in the MD simulation. The results lead to following conclusions.

(1) As increasing temperature, there are more kinetic energy offer interfacial atoms to relax their local structures. However, the NVT ensemble applied the constraint on the lateral sides in the simulation box. That is similar to a high pressure condition which results Cu atoms congregate in the Mg matrix from network to clusters. On the other hand, the experiment results also show that there are not obvious amorphous structures in the similar condition, just

Mg_2Cu compound forming in the Mg-Cu multilayer.

(2) A suitable ensemble, e.g. isothermal-isobaric (NPT) ensemble, is needed to take place of the current model to enhance the possibility of phase transition for forming the complex compound structures in Mg-Cu system. Diffusion behavior of atoms in lower temperature is strongly time-dependent and needs much longer time period. It could be better to investigate this propertie by MC method instead of MD in the future.

Through the molecular dynamics studies of the cyclic loading response of $Zr_{50}Cu_{50}$ metallic glasses, the following conclusions can be reached.

(1) Throughout the current cyclic deformation under the stress or strain control mode, there are no major atomic structure changes or stress-induced crystallization, as judged from the PRDF and HA index. This is thought to be a result of the limited simulated volume, within which the STZs are still in their early development. The mature shear bands are not yet fully developed even under the most severe strain control mode.

(2) The current simulated results demonstrate that the induced STZs, measuring 10-20 Å, are basically discrete and homogeneous. The temporary local STZs formed in one fatigue cycle frequently disappear in the subsequent unloading or reversed-stress loading cycles.

(3) Based on the deformation evolution as a function of cyclic loading, as evidenced by the simulated ABRA, potential energy, atomic density, and fatigue softening results, the current Zr-Cu amorphous alloy appears be deformed more readily in the initial fatigue stage, followed by gradual saturated behavior.

(4) It is found that structure relaxation, or dynamic recovery, has occurred in the current cyclic loading of the Zr-Cu metallic glass. When the fatigue stress or strain is low, still well within the elastic range, the dynamic recovery of RRCs will dominate the most atomic events. When the fatigue stress or strain exceeds into the plastic regime, dynamic recovery of IRRCs becomes easier.

(5) Through the self-repairing and dynamic recovery capability of IRRCs, the current Zr-Cu metallic glass could reduce the local spatial defects in STZs induced by the previous cyclic deformation. Thus the overall metallic glassy structure under fatigue could resist the damage accumulation, exhibiting satisfactory fatigue resistance.

(6) The current simulation results suggest that the metallic glass in small size-scale can be quite fatigue resistant. The metallic bonds in the metallic glasses, once broken by local shear stress, can be self-repaired and re-bonded to neighboring atoms by the subsequent reverse shear stress. Such a dynamic recovery capability is particularly significant in fatigue loading. For applications of the metallic glasses in micro-electro-mechanical systems (MEMS), the current finding is encouraging.

Reference

1. K.L. Chapra, *Thin Film Phenomena*. 1969: McGraw-Hill.
2. P.S. Gramt, Progress in Materials Science, 1995, 39, 497.
3. B. Li, N. Nordstrom and E.J. Lavernia, Mater. Sci. Eng. A, 1997, 237, 207.
4. C.R.M. Afonso, C. Bolfarini, C.S. Kiminami, N.D. Bassim, M.J. Kaufman, M.F. Amateau, T.J. Eden and J.M. Galbraith, Journal of Non-Crystalline Solids, 2001, 284, 134-138.
5. R. Liu, J. Li, K. Dong, C. Zheng and H. Liu, Mater. Sci. Eng. B, 2002, 94, 141.
6. C.C. Koch, O.B. Cavin, C.G. McKamey and J.O. Scarbrough, Applied Physics Letters, 1983, 43, 1017-1019.
7. J. Eckert, Mater. Sci. Eng. A, 1997, 226-228, 364.
8. N. Schultz, Mater. Sci. Eng., 1998, 97, 15.
9. F.Z. J. Lee, K. H. Chung, N. J. Kim, and E. J. Lavernia,, Metall. Mater. Trans. A, 2001, 32, 3109.
10. M. Sherif, E. Eskandarany and A. Inoue, Metall. Mater. Trans. A, 2002, 33, 135.
11. Z.P. Xing, S.B. Kang and H.W. Kim, Metallurgical and Materials Transactions a-Physical Metallurgy and Materials Science, 2002, 33, 1521-1530.
12. X.L. Yeh, K. Samwer and W.L. Johnson, Applied Physics Letters, 1983, 42, 242-244.
13. A. Sagel, H. Sieber, H.J. Fecht and J.H. Perepzko, Acta Materialia, 1998, 46, 4233.
14. N. Tsuji, Y. Saito, S.H. Lee and Y. Minamino, Advanced Engineering Materials, 2003, 5, 338.
15. Y. Saito, N. Tsuji, H. Utsunomiya, T. Sakai and R.G. Hong, Scripta Materialia, 1998, 39, 1221-1227.
16. R.B. Schwarz and W.L. Johnson, Physical Review Letters, 1983, 51, 415-418.

17. P. Haussler, F. Baumann, J. Krieg, G. Indlekofer, P. Oelhafen and H.J. Guntherodt, Physical Review Letters, 1983, 51, 714-717.
18. A.L. Greer, Science, 1995, 267, 1947-1953.
19. W.L. Johnson, Mrs Bulletin, 1999, 24, 42-56.
20. W.H. Wang, C. Dong and C.H. Shek, Materials Science & Engineering R-Reports, 2004, 44, 45-89.
21. J.P.K. Doye and D.J. Wales, Science, 1996, 271, 484-487.
22. F. Spaepen, Nature, 2000, 408, 781-782.
23. H.W. Sheng, W.K. Luo, F.M. Alamgir, J.M. Bai and E. Ma, Nature, 2006, 439, 419-425.
24. H. Tanaka, Journal of Non-Crystalline Solids, 2005, 351, 3396-3413.
25. Y.I. Golovin, V.I. Ivolgin, V.A. Khonik, K. Kitagawa and A.I. Tyurin, Scripta Materialia, 2001, 45, 947-952.
26. P. Murah and U. Ramamurty, Acta Materialia, 2005, 53, 1467-1478.
27. U. Ramamurty, S. Jana, Y. Kawamura and K. Chattopadhyay, Acta Materialia, 2005, 53, 705-717.
28. G.P. Zhang, W. Wang, B. Zhang, J. Tan and C.S. Liu, Scripta Materialia, 2005, 52, 1147-1151.
29. J.R. Morris, R.S. Aga, T. Egami and V.A. Levashov, International Journal of Modern Physics B, 2009, 23, 1229-1234.
30. K. Nordlund and R.S. Averback, Applied Physics Letters, 1997, 70, 3101-3103.
31. J.S. Robach, I.M. Robertson, H.J. Lee and B.D. Wirth, Acta Materialia, 2006, 54, 1679-1690.
32. H. Van Swygenhoven, P.M. Derlet and A.G. Froseth, Acta Materialia, 2006, 54, 1975-1983.
33. H. Van Swygenhoven, D. Farkas and A. Caro, Physical Review B, 2000, 62, 831-838.

34. D. Wolf, V. Yamakov, S.R. Phillpot, A. Mukherjee and H. Gleiter, Acta Materialia, 2005, 53, 1-40.

35. G.P. Zheng, Y.M. Wang and M. Li, Acta Materialia, 2005, 53, 3893-3901.

36. P.C. Millett, R.P. Selvam and A. Saxena, Acta Materialia, 2006, 54, 297-303.

37. P.J. Hsieh, Y.P. Hung and J.C. Huang, Scripta Materialia, 2003, 49, 173-178.

38. P.J. Hsieh, J.C. Huang, Y.P. Hung, S.I. Chou and J.S.C. Jang, Materials Chemistry and Physics, 2004, 88, 364-376.

39. P.J. Hsieh, Y.P. Hung, S.I. Chou and J.C. Huang, Materials Transactions, 2004, 45, 2686-2692.

40. S. Vautha and S.G. Mayr, Appl. Phys. Lett., 2005, 86, 061913.

41. X. He, S.H. Liang, J.H. Li and B.X. Liu, Physical Review B, 2007, 75, 10.

42. G.Y. Wang, P.K. Liaw, W.H. Peter, B. Yang, Y. Yokoyama, M.L. Benson, B.A. Green, M.J. Kirkham, S.A. White, T.A. Saleh, R.L. McDaniels, R.V. Steward, R.A. Buchanan, C.T. Liu and C.R. Brooks, Intermetallics, 2004, 12, 885-892.

43. G.Y. Wang, P.K. Liaw, W.H. Peter, B. Yang, M. Freels, Y. Yokoyama, M.L. Benson, B.A. Green, T.A. Saleh, R.L. McDaniels, R.V. Steward, R.A. Buchanan, C.T. Liu and C.R. Brooks, Intermetallics, 2004, 12, 1219-1227.

44. W. Klement, R.H. Willens and P. Duwez, Nature, 1960, 187, 869-870.

45. H.S. Chen and D. Turnbull, Acta Metallurgica, 1969, 17, 1021-1031.

46. H.S. Chen, Acta Metallurgica, 1974, 22, 1505-1511.

47. D. Turnbull and J.C. Fisher, Journal of Chemical Physics, 1949, 17, 71-73.

48. Z.P. Lu and C.T. Liu, Acta Materialia, 2002, 50, 3501-3512.

49. L. Xia, S.S. Fang, Q. Wang, Y.D. Dong and C.T. Liu, Applied Physics Letters, 2006, 88, 3.

50. A.J. Drehman, A.L. Greer and D. Turnbull, Applied Physics Letters, 1982, 41, 716-717.

51. H.W. Kui, A.L. Greer and D. Turnbull, Applied Physics Letters, 1984, 45, 615-616.

52. W.L. Johnson, Progress in Materials Science, 1986, 30, 81-134.

53. A. Inoue, T. Zhang and T. Masumoto, Materials Transactions, JIM, 1989, 30, 965-972.

54. A. Inoue, Acta Materialia, 2000, 48, 279-306.

55. A. Inoue, A. Kato, T. Zhang, S.G. Kim and T. Masumoto, Materials Transactions, JIM, 1991, 32, 609-616.

56. T. Zhang, A. Inoue and T. Masumoto, Materials Transactions, JIM, 1991, 32, 1005-1010.

57. A. Inoue, T. Zhang, N. Nishiyama, K. Ohba and T. Masumoto, Materials Transactions, JIM, 1993, 34, 1234-1237.

58. A. Inoue, Materials Transactions, JIM, 1995, 36, 866-875.

59. A. Inoue, N. Nishiyama and H. Kimura, Materials Transactions, JIM, 1997, 38, 179-183.

60. A. Inoue, Materials Science and Engineering A, 2001, 304-306, 1-10.

61. M. Leonhardt, W. Loser and H.G. Lindenkreuz, Acta Materialia, 1999, 47, 2961-2968.

62. F.Q. Guo, S.J. Poon and G.J. Shiflet, Applied Physics Letters, 2004, 84, 37-39.

63. W.J. Meng, B. Fultz, E. Ma and W.L. Johnson, Applied Physics Letters, 1987, 51, 661-663.

64. W.J. Meng, C.W. Nieh and W.L. Johnson, Applied Physics Letters, 1987, 51, 1693-1695.

65. D. Wang, Y. Li, B.B. Sun, M.L. Sui, K. Lu and E. Ma, Applied Physics Letters, 2004, 84, 4029-4031.

66. D.H. Xu, B. Lohwongwatana, G. Duan, W.L. Johnson and C. Garland, Acta Materialia, 2004, 52, 2621-2624.

67. T. Hattori, H. Saitoh, H. Kaneko, Y. Okajima, K. Aoki and W. Utsumi, Physical Review Letters, 2006, 96, 4.

68. J.D. Bernal, Nature, 1959, 183, 141.

69. M.H. Cohen and D. Turnbull, Nature, 1964, 203, 964.

70. R. Wang, Nature, 1979, 278, 700-704.

71. A. Inoue, T. Negishi, H.M. Kimura, T. Zhang and A.R. Yavari, Materials Transactions Jim, 1998, 39, 318-321.

72. W.H. Wang, R.J. Wang, D.Q. Zhao, M.X. Pan and Y.S. Yao, Physical Review B, 2000, 62, 11292-11295.

73. W.H. Wang, Q. Wei, S. Friedrich, M.P. Macht, N. Wanderka and H. Wollenberger, Applied Physics Letters, 1997, 71, 1053-1055.

74. A. Inoue, *Bulk Amorphous Alloys*. 1998: Trans Tech Publications.

75. J.D. Honeycutt and H.C. Andersen, Journal of Physical Chemistry, 1987, 91, 4950-4963.

76. H. Jonsson and H.C. Andersen, Physical Review Letters, 1988, 60, 2295-2298.

77. J.H. He and E. Ma, Physical Review B, 2001, 64, 12.

78. J.H. He, H.W. Sheng, P.J. Schilling, C.L. Chien and E. Ma, Physical Review Letters, 2001, 86, 2826-2829.

79. W.K. Luo, H.W. Sheng, F.M. Alamgir, J.M. Bai, J.H. He and E. Ma, Physical Review Letters, 2004, 92, 4.

80. C.F. Li, J. Saida, M. Matsushita and A. Inoue, Applied Physics Letters, 2000, 77, 528-530.

81. H. Reichert, O. Klein, H. Dosch, M. Denk, V. Honkimaki, T. Lippmann and G. Reiter, Nature, 2000, 408, 839-841.

82. D.R.N.a.F. Spaepen, Solid State Physics, 1989, 42, 1.

83. J. Saida, M. Matsushita and A. Inoue, Applied Physics Letters, 2001, 79, 412-414.

84. W.H. Wang, E. Wu, R.J. Wang, S.J. Kennedy and A.J. Studer, Physical Review B, 2002, 66, 5.

85. T. Waniuk, J. Schroers and W.L. Johnson, Physical Review B, 2003, 67, 9.
86. J.M. Cowley, Ultramicroscopy, 2002, 90, 197-206.
87. N. Mattern, U. Kuhn, H. Hermann, H. Ehrenberg, J. Neuefeind and J. Eckert, Acta Materialia, 2002, 50, 305-314.
88. T.C. Hufnagel, Nature Materials, 2004, 3, 666-667.
89. A. Hirata, Y. Hirotsu, E. Matsubara, T. Ohkubo and K. Hono, Physical Review B, 2006, 74, 6.
90. D.B. Miracle, Nature Materials, 2004, 3, 697-702.
91. G.L. Chen, X.J. Liu, X.D. Hui, H.Y. Hou, K.F. Yao, C.T. Liu and J. Wadsworth, Applied Physics Letters, 2006, 88, 3.
92. C. Fan, P.K. Liaw, V. Haas, J.J. Wall, H. Choo, A. Inoue and C.T. Liu, Physical Review B, 2006, 74, 6.
93. C. Fan, P.K. Liaw, T.W. Wilson, H. Choo, Y.F. Gao, C.T. Liu, T. Proffen and J.W. Richardson, Applied Physics Letters, 2006, 89, 3.
94. C. Fan, P.K. Liaw, T.W. Wilson, W. Dmowski, H. Choo, C.T. Liu, J.W. Richardson and T. Proffen, Applied Physics Letters, 2006, 89, 3.
95. A. Takeuchi and A. Inoue, Materials Science and Engineering a-Structural Materials Properties Microstructure and Processing, 2004, 375, 1140-1144.
96. K.M. Flores and R.H. Dauskardt, Acta Materialia, 2001, 49, 2527-2537.
97. K.M. Flores and R.H. Dauskardt, Journal of Materials Research, 1999, 14, 638-643.
98. A. Inoue and A. Takeuchi, Materials Transactions, 2002, 43, 1892-1906.
99. W.L. Johnson, Jom-Journal of the Minerals Metals & Materials Society, 2002, 54, 40-43.
100. C.C. Hays, C.P. Kim and W.L. Johnson, Physical Review Letters, 2000, 84, 2901-2904.
101. J. Schroers and W.L. Johnson, Physical Review Letters, 2004, 93, 4.

102. M.H. Cohen and D. Turnbull, Journal of Chemical Physics, 1959, 31, 1164-1169.

103. F. Spaepen, Acta Metallurgica, 1977, 25, 407-415.

104. A.S. Argon, Acta Metallurgica, 1979, 27, 47-58.

105. P.L. Michael Miller, *Bulk Metallic Glasses: An Overview*. Hardcover ed. 2007: Springer

106. A. Vandenbeukel and J. Sietsma, Acta Metallurgica Et Materialia, 1990, 38, 383-389.

107. B. Yang, M.L. Morrison, P.K. Liaw, R.A. Buchanan, G.Y. Wang, C.T. Liu and M. Denda, Applied Physics Letters, 2005, 86, 141904.

108. F. Albano and M.L. Falk, Journal of Chemical Physics, 2005, 122, 8.

109. Q.K. Li and M. Li, Applied Physics Letters, 2006, 88, 3.

110. Q.K. Li and M. Li, Physical Review B, 2007, 75, 5.

111. M.W. Chen, Annual Review of Materials Research, 2008, 38, 445-469.

112. C.A. Schuh, T.C. Hufnagel and U. Ramamurty, Acta Materialia, 2007, 55, 4067-4109.

113. C.A. Schuh and A.C. Lund, Nature Materials, 2003, 2, 449-452.

114. P.G. Debenedetti and F.H. Stillinger, Nature, 2001, 410, 259-267.

115. W.L. Johnson and K. Samwer, Physical Review Letters, 2005, 95, 4.

116. M. Zink, K. Samwer, W.L. Johnson and S.G. Mayr, Physical Review B, 2006, 73, 3.

117. M.L. Falk and J.S. Langer, Physical Review E, 1998, 57, 7192-7205.

118. M.L. Manning, J.S. Langer and J.M. Carlson, Physical Review E, 2007, 76, 16.

119. Y.F. Shi, M.B. Katz, H. Li and M.L. Falk, Physical Review Letters, 2007, 98, 4.

120. J.S. Langer, Physical Review E, 2008, 77, 021502.

121. M.L. Manning, E.G. Daub, J.S. Langer and J.M. Carlson, Physical Review E, 2009, 79, 17.

122. E. Pekarskaya, C.P. Kim and W.L. Johnson, Journal of Materials Research, 2001, 16, 2513-2518.

123. J. Li, F. Spaepen and T.C. Hufnagel, Philosophical Magazine A, 2002, 82, 2623-2630.

124. T.C. Hufnagel, T. Jiao, Y. Li, L.Q. Xing and K.T. Ramesh, Journal of Materials Research, 2002, 17, 1441-1445.

125. Q.K. Li and M. Li, Applied Physics Letters, 2005, 87, 031910

126. Q.K. Li and M. Li, Intermetallics, 2006, 14, 1005-1010.

127. N.P. Bailey, J. Schiotz and K.W. Jacobsen, Physical Review B, 2006, 73, 12.

128. F. Shimizu, S. Ogata and J. Li, Acta Materialia, 2006, 54, 4293-4298.

129. F. Shimizu, S. Ogata and J. Li, Materials Transactions, 2007, 48, 2923-2927.

130. S. Ogata, F. Shimizu, J. Li, M. Wakeda and Y. Shibutani, Intermetallics, 2006, 14, 1033-1037.

131. J.J. Lewandowski and A.L. Greer, Nature Materials, 2006, 5, 15-18.

132. F. Spaepen, Nature Materials, 2006, 5, 7-8.

133. B. Yang, C.T. Liu, T.G. Nieh, M.L. Morrison, P.K. Liaw and R.A. Buchanan, Journal of Materials Research, 2006, 21, 915-922.

134. M.L. Morrison, R.A. Buchanan, P.K. Liaw, B.A. Green, G.Y. Wang, C. Liu and J.A. Horton, Materials Science and Engineering a-Structural Materials Properties Microstructure and Processing, 2007, 467, 190-197.

135. M.L. Morrison, R.A. Buchanan, P.K. Liaw, B.A. Green, G.Y. Wang, C.T. Liu and J.A. Horton, Materials Science and Engineering a-Structural Materials Properties Microstructure and Processing, 2007, 467, 198-206.

136. C.J. Gilbert, V. Schroeder and R.O. Ritchie, Metallurgical and Materials Transactions a-Physical Metallurgy and Materials Science, 1999, 30, 1739-1753.

137. C.J. Gilbert, J.M. Lippmann and R.O. Ritchie, Scripta Materialia, 1998, 38, 537-542.

138. K.K. Cameron and R.H. Dauskardt, Scripta Materialia, 2006, 54, 349-353.

139. M.E. Launey, R. Busch and J.J. Kruzic, Acta Materialia, 2008, 56, 500-510.

140. D.F.a.B. Smit, *Understanding Molecular Simulation from Algorithms to Applications*. 2nd edition ed. 2002: Academic Press.

141. F.F. Chen, H.F. Zhang, F.X. Qin and Z.Q. Hu, Journal of Chemical Physics, 2004, 120, 1826-1831.

142. M.P. Allen and D.J. Tildesly, *Computer Simulation of Liquids*. 1987: Clarendon.

143. W.J. Minkowycz and E.M. Sparrow, Numerical Heat Transfer Part a-Applications, 2002, 42, 1.

144. W.J. Minkowycz and E.M. Sparrow, Numerical Heat Transfer Part B-Fundamentals, 1998, 33, 3-3.

145. M.S. Daw and M.I. Baskes, Physical Review B, 1984, 29, 6443-6453.

146. L.V. Woodcock, Chemical Physics Letters, 1971, 10, 257-&.

147. S. Nose, Progress of Theoretical Physics Supplement, 1991, 1-46.

148. H.C. Andersen, Journal of Chemical Physics, 1980, 72, 2384-2393.

149. S. Nose, Journal of Chemical Physics, 1984, 81, 511-519.

150. S. Nose, Molecular Physics, 1984, 52, 255-268.

151. W.G. Hoover, Physical Review A, 1986, 34, 2499-2500.

152. M. Parrinello and A. Rahman, Physical Review Letters, 1980, 45, 1196-1199.

153. M.P. Allen, 2004.

154. F. Cleri and V. Rosato, Physical Review B, 1993, 48, 22-33.

155. H.K. F. Shimizu, H. Kaburaki, J. Li and S. Yip. in *Proceedings of the Fourth International Conference SNA2000*. 2000.

156. G. Duan, D.H. Xu, Q. Zhang, G.Y. Zhang, T. Cagin, W.L. Johnson and W.A. Goddard, Physical Review B, 2005, 71, 9.

157. V. Yamakov, D. Wolf, S.R. Phillpot, A.K. Mukherjee and H. Gleiter, Nature Materials, 2002, 1, 45-48.

158. J. Liu, J.Z. Zhao and Z.Q. Hu, Materials Science and Engineering a-Structural Materials Properties Microstructure and Processing, 2007, 452, 103-109.

159. Y.T. Zhu and X.Z. Liao, Applied Physics Letters, 2005, 86, 3.

160. J.D. Honeycutt and H.C. Andersen, Chemical Physics Letters, 1984, 108, 535-538.

161. K.W. Jacobsen, J.K. Norskov and M.J. Puska, Physical Review B, 1987, 35, 7423-7442.

162. K.W. Jacobsen, P. Stoltze and J.K. Norskov, Surface Science, 1996, 366, 394-402.

163. J. Schiotz and K.W. Jacobsen, Science, 2003, 301, 1357-1359.

164. N.P. Bailey, J. Schiotz and K.W. Jacobsen, Physical Review B, 2004, 69, 11.

165. A. Paduraru, A. Kenoufi, N.P. Bailey and J. Schiotz, Advanced Engineering Materials, 2007, 9, 505-508.

166. M.E. Tuckerman and G.J. Martyna, Journal of Physical Chemistry B, 2000, 104, 159-178.

167. M.E. Tuckerman, D.A. Yarne, S.O. Samuelson, A.L. Hughes and G.J. Martyna, Computer Physics Communications, 2000, 128, 333-376.

168. C.J. Mundy, S. Balasubramanian, K. Bagchi, M.E. Tuckerman, G.J. Martyna and M.L. Klein, *Nonequilibrium molecular dynamics*, in *Reviews in Computational Chemistry, Vol 14*. 2000, Wiley-Vch, Inc: New York. p. 291-397.

169. Y.H. Lai, C.J. Lee, Y.T. Cheng, H.S. Chou, H.M. Chen, X.H. Du, C.I. Chang, J.C. Huang, S.R. Jian, J.S.C. Jang and T.G. Nieh, Scripta Materialia, 2008, 58, 890-893.

170. C.J. Lee, J.C. Huang and T.G. Nieh, Applied Physics Letters, 2007, 91, 3.

171. G.P. Potirniche, M.F. Horstemeyer, G.J. Wagner and P.M. Gullett, International Journal of Plasticity, 2006, 22, 257-278.

172. G.P. Potirniche, M.F. Horstemeyer, P.M. Gullett and B. Jelinek, Proceedings of the Royal Society a-Mathematical Physical and Engineering Sciences, 2006, 462, 3707-3731.

173. L. Tayebi, C.E. Lekka and G.A. Evangelakis. *Poisson ratio under compressive and tensile strain; effect on the mechanical response of the Cu46Zr54 metallic glass*. 2008: Wiley-V C H Verlag Gmbh.

174. Z.W. Shan, J. Li, Y.Q. Cheng, A.M. Minor, S.A.S. Asif, O.L. Warren and E. Ma, Physical Review B, 2008, 77, 6.

175. P.J. Hsieh, Y.C. Lo, J.C. Huang and S.P. Ju, Intermetallics, 2006, 14, 924-930.

176. A.C. Lund and C.A. Schuh, Journal of Applied Physics, 2004, 95, 4815-4822.

177. C.A. Schuh, A.C. Lund and T.G. Nieh, Acta Materialia, 2004, 52, 5879-5891.

178. L.J. Peng, J.R. Morris and Y.C. Lo, Physical Review B, 2008, 78, 4.

179. Y.F. Shi and M.L. Falk, Physical Review B, 2006, 73, 10.

180. P. Nash, *Phase Diagrams of Binary Alloys*, ed. M. Park. 1991, Ohio, USA: ASM International.

181. T.B. Massalski, *Binary Alloy Phase Diagrams*. second edition ed. 1990, Ohio, USA: ASM International, Materials Park,.

182. M.S. Ong, Y. Li, D.J. Blackwood and S.C. Ng. *The influence of heat treatment on the corrosion behaviour of amorphous melt-spun binary Mg-18 at.% Ni and Mg-21 at.% Cu alloy*. 2001: Elsevier Science Sa.

183. O.P. Pandey, S.N. Ojha and T.R. Anantharaman, Journal of Materials Science Letters, 1992, 11, 1260-1262.

184. Y.C. Lo, J.C. Huang, C.L. Chen, S.P. Ju, H.S. Chou, X.H. Du, M.C. Liu and C.N. Kuo, Journal of Computational and Theoretical Nanoscience, 2008, 5, 1717-1721.

185. J.J. Kim, Y. Choi, S. Suresh and A.S. Argon, Science, 2002, 295, 654-657.

186. C.L. Na Wang, Zhenmin Du, Fuming Wang, and Weijing Zhanga, Computer Coupling of Phase Diagrams and Thermochemistry, 2006, 30, 461.

187. V.A. Khonik, A.T. Kosilov, V.A. Mikhailov and V.V. Sviridov, Acta Materialia, 1998, 46, 3399-3408.

188. V.I. Belyavsky, K. Csach, V.A. Khonik, V.A. Mikhailov and V. Ocelik, Journal of Non-Crystalline Solids, 1998, 241, 105-112.

189. G. Kumar, H.X. Tang and J. Schroers, Nature, 2009, 457, 868-872.

190. A. Takeuchi and A. Inoue. *Size dependence of soft to hard magnetic transition in (Nd, Pr)-Fe-Al bulk amorphous alloys*. 2004: Elsevier Science Sa.

191. K. Wang, T. Fujita, Y.Q. Zeng, N. Nishiyama, A. Inoue and M.W. Chen, Acta Materialia, 2008, 56, 2834-2842.

Table2-1 Bulk metallic glasses and their developed years [20].

BMG system	Years
Pd–Cu–Si	1974
Pt–Ni–P	1975
Au–Si–Ge	1975
Pd–Ni–P	1982
Mg–Ln–Cu (Ln = lanthanide metal)	1988
Ln–Al–TM (TM = group transition metal)	1989
Zr–Ti–Al–TM	1990
Ti–Zr–TM	1993
Zr–Ti–Cu–Ni–Be	1993
Nd(Pr)–Al–Fe–Co	1994
Zr–(Nb, Pd)–Al–TM	1995
Cu–Zr–Ni–Ti	1995
Fe–(Nb, Mo)–(Al, Ga)–(P, C, B, Si, Ge)	1995
Pd–Cu(Fe)–Ni–P	1996
Co–(Al, Ga)–(P, B, Si)	1996
Fe–(Zr, Hf, Nb)–B	1996
Co–Fe–(Zr, Hf, Nb)–B	1996
Ni–(Zr, Hf, Nb)–(Cr, Mo)–B	1996
Ti–Ni–Cu–Sn	1998
La–Al–Ni–Cu–Co	1998
Ni–Nb	1999
Ni–(Nb, Cr, Mo)–(P, B)	1999
Zr-based glassy composites	1999
Zr–Nb–Cu–Fe–Be	2000
Fe–Mn–Mo–Cr–C–B	2002
Ni–Nb–(Sn, Ti)	2003
Pr(Nd)–(Cu, Ni)–Al	2003

Table2-2 Summary of yield and ultimate tensile strengths, fatigue-endurance limits at 10^7 cycles, and fatigue ratios based on the stress amplitudes of Zr-based BMGs and various crystalline alloys from the current study and literature reports. Test configuration refers to the fatigue-test geometry and R is the stress ratio of σ_{min} to σ_{max} [134, 135].

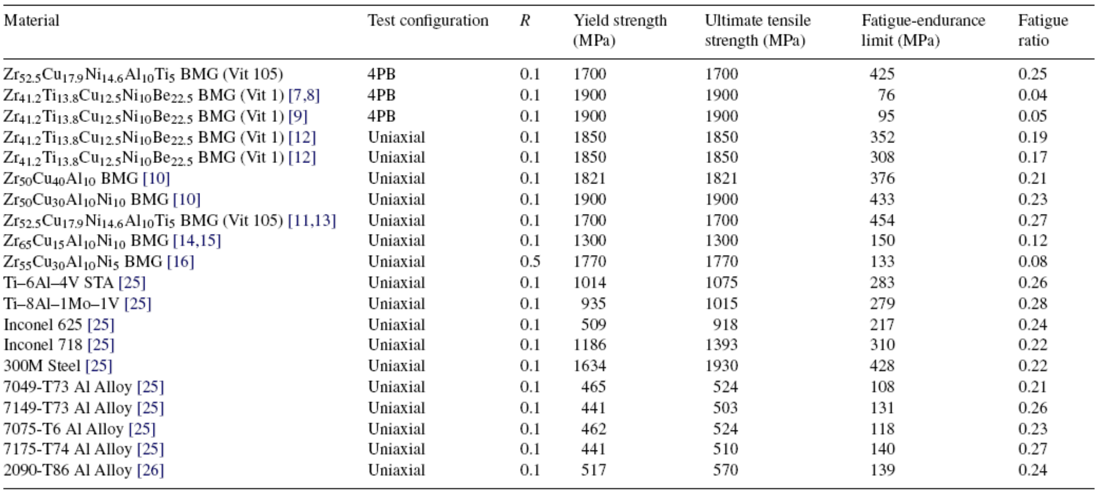

Material	Test configuration	*R*	Yield strength (MPa)	Ultimate tensile strength (MPa)	Fatigue-endurance limit (MPa)	Fatigue ratio
$Zr_{52.5}Cu_{17.9}Ni_{14.6}Al_{10}Ti_5$ BMG (Vit 105)	4PB	0.1	1700	1700	425	0.25
$Zr_{41.2}Ti_{13.8}Cu_{12.5}Ni_{10}Be_{22.5}$ BMG (Vit 1) [7,8]	4PB	0.1	1900	1900	76	0.04
$Zr_{41.2}Ti_{13.8}Cu_{12.5}Ni_{10}Be_{22.5}$ BMG (Vit 1) [9]	4PB	0.1	1900	1900	95	0.05
$Zr_{41.2}Ti_{13.8}Cu_{12.5}Ni_{10}Be_{22.5}$ BMG (Vit 1) [12]	Uniaxial	0.1	1850	1850	352	0.19
$Zr_{41.2}Ti_{13.8}Cu_{12.5}Ni_{10}Be_{22.5}$ BMG (Vit 1) [12]	Uniaxial	0.1	1850	1850	308	0.17
$Zr_{50}Cu_{40}Al_{10}$ BMG [10]	Uniaxial	0.1	1821	1821	376	0.21
$Zr_{50}Cu_{30}Al_{10}Ni_{10}$ BMG [10]	Uniaxial	0.1	1900	1900	433	0.23
$Zr_{52.5}Cu_{17.9}Ni_{14.6}Al_{10}Ti_5$ BMG (Vit 105) [11,13]	Uniaxial	0.1	1700	1700	454	0.27
$Zr_{65}Cu_{15}Al_{10}Ni_{10}$ BMG [14,15]	Uniaxial	0.1	1300	1300	150	0.12
$Zr_{55}Cu_{30}Al_{10}Ni_5$ BMG [16]	Uniaxial	0.5	1770	1770	133	0.08
Ti–6Al–4V STA [25]	Uniaxial	0.1	1014	1075	283	0.26
Ti–8Al–1Mo–1V [25]	Uniaxial	0.1	935	1015	279	0.28
Inconel 625 [25]	Uniaxial	0.1	509	918	217	0.24
Inconel 718 [25]	Uniaxial	0.1	1186	1393	310	0.22
300M Steel [25]	Uniaxial	0.1	1634	1930	428	0.22
7049-T73 Al Alloy [25]	Uniaxial	0.1	465	524	108	0.21
7149-T73 Al Alloy [25]	Uniaxial	0.1	441	503	131	0.26
7075-T6 Al Alloy [25]	Uniaxial	0.1	462	524	118	0.23
7175-T74 Al Alloy [25]	Uniaxial	0.1	441	510	140	0.27
2090-T86 Al Alloy [26]	Uniaxial	0.1	517	570	139	0.24

Table 3-1 Parameters for Lennard-Jones potential for inert molecules [143].

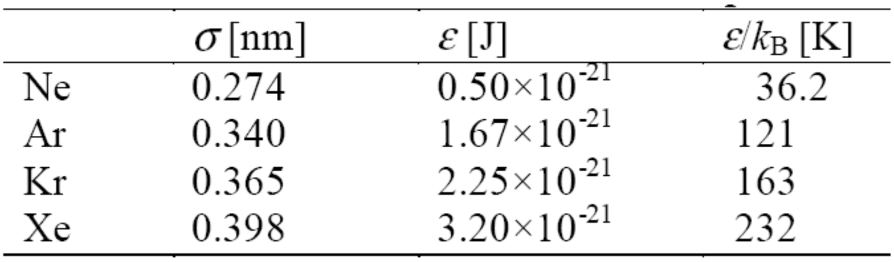

	σ [nm]	ε [J]	ε/k_B [K]
Ne	0.274	0.50×10^{-21}	36.2
Ar	0.340	1.67×10^{-21}	121
Kr	0.365	2.25×10^{-21}	163
Xe	0.398	3.20×10^{-21}	232

Table 4-1 Parameters used in the tight-binding potential.

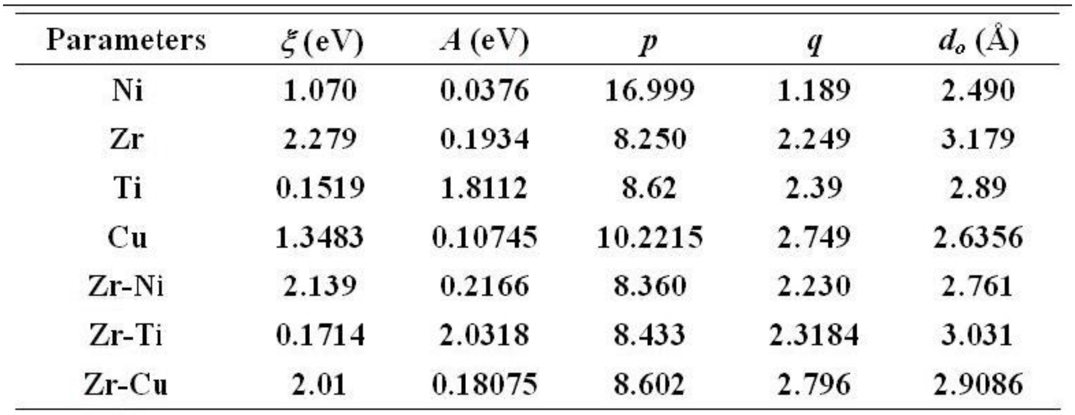

Parameters	ξ (eV)	A (eV)	p	q	d_o (Å)
Ni	1.070	0.0376	16.999	1.189	2.490
Zr	2.279	0.1934	8.250	2.249	3.179
Ti	0.1519	1.8112	8.62	2.39	2.89
Cu	1.3483	0.10745	10.2215	2.749	2.6356
Zr-Ni	2.139	0.2166	8.360	2.230	2.761
Zr-Ti	0.1714	2.0318	8.433	2.3184	3.031
Zr-Cu	2.01	0.18075	8.602	2.796	2.9086

Table 4-2 Effective medium potential parameters [162, 164].

	E_0 (eV)	S_0 (Å)	V_0 (eV)	η_2 (Å)	k (Å^{-1})	λ (Å^{-1})	n_0 (Å^{-3})
Cu	-3.51	1.412964	2.476	3.12170	5.17763	3.60166	0.06140
Ag	-2.96	1.592892	2.132	3.12170	5.27211	3.57521	0.03691
Au	-3.80	1.5876	2.321	3.16327	5.42895	4.12320	0.04743
Ni	-4.44	1.37592	3.673	3.15382	5.20975	3.68103	0.06950
Pd	-3.90	1.518804	2.773	3.43537	5.87113	4.07218	0.04642
Pt	-5.85	1.53468	4.067	3.42404	5.94293	4.14210	0.05411
Mg	-1.487	1.766399	2.22987	2.541137	4.435425	3.292725	0.035544

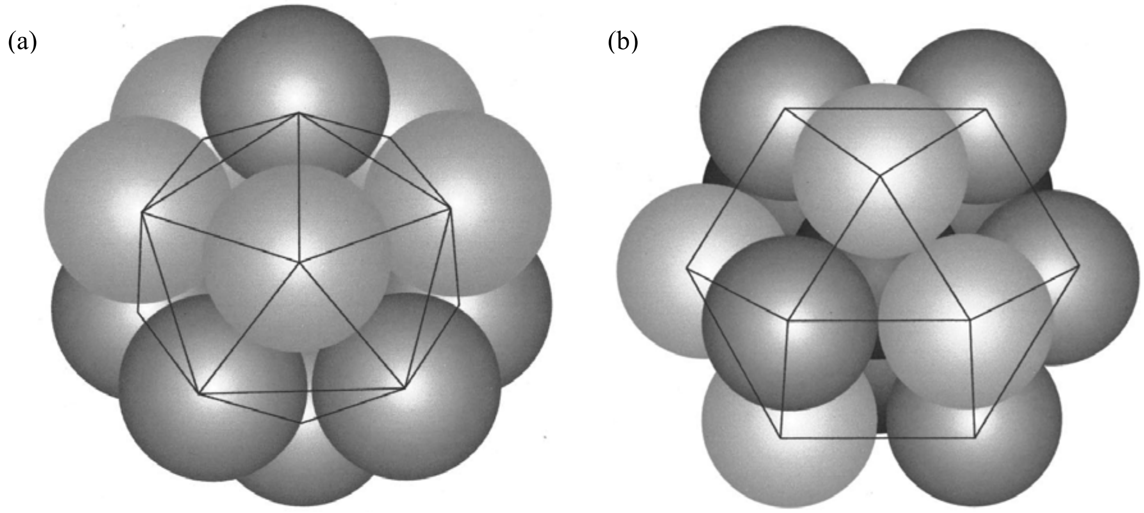

Fig. 2-1. (a) The fivefold symmetry and an icosahedral arrangement are shown with the brighter spheres (b) A face-centered-cubic arrangement. The same pair will become the hcp arrangement if the top close-packed plane is shifted to take the same type of position as the bottom plane [77].

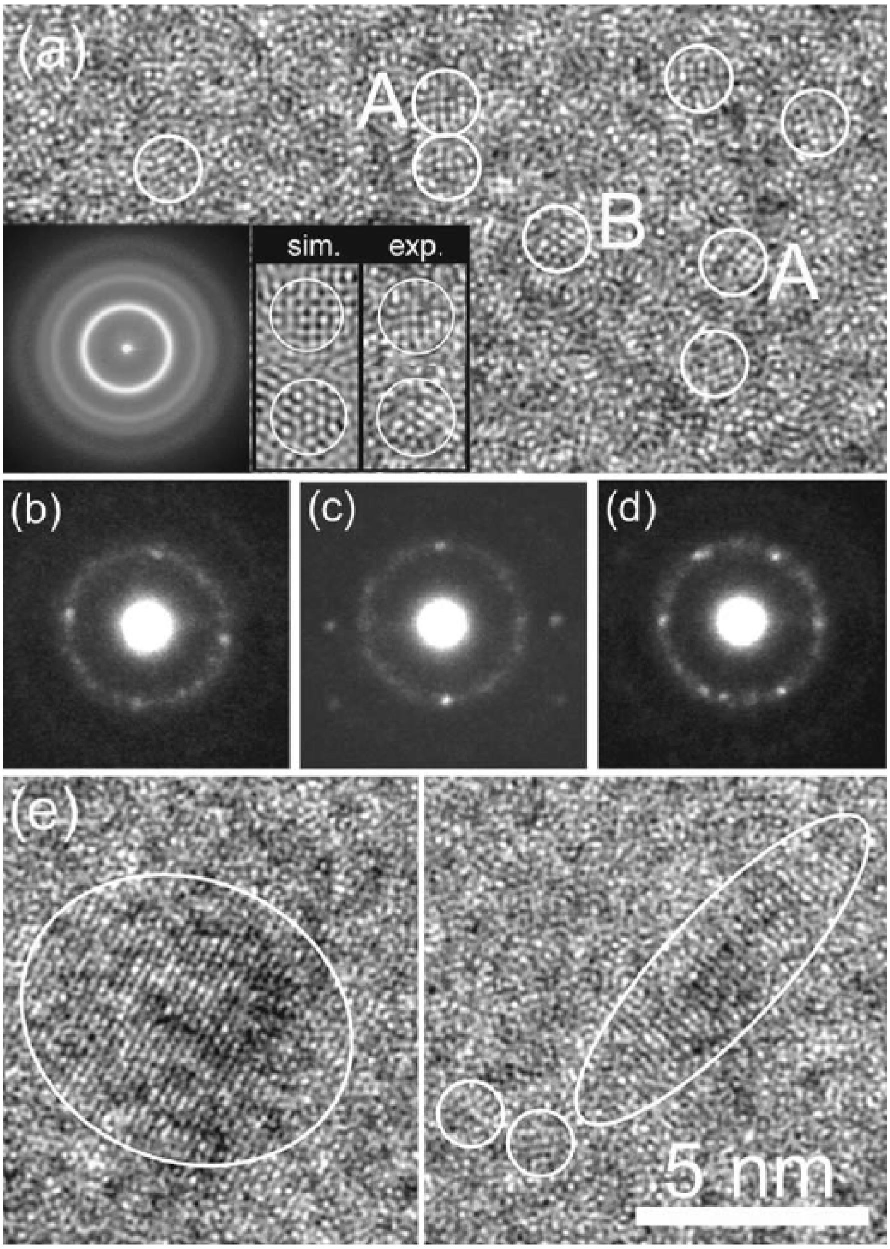

Fig. 2-2. (a) HREM image taken from an annealed specimen (773 K), together with nanobeam electron-diffraction patterns in (b), (c), and (d). Simulated HREM image is also shown in the inset of (a). (e) HREM image of minor regions in the specimen annealed up to 773 K [89].

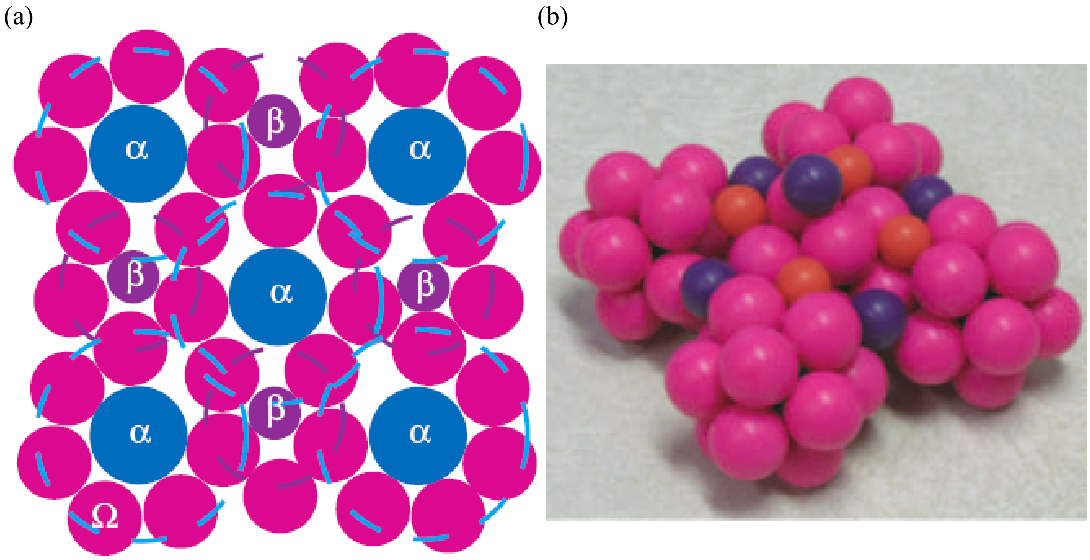

Fig. 2-3. The portions of a single cluster unit cell for the dense cluster packing model. (a) A two-dimensional representation of a dense cluster-packing structure in a (100) plane of clusters illustrating the features of interpenetrating clusters and efficient atomic packing around each solute. (b) A portion of a cluster unit cell of model in $[12\bar{1}\bar{0}9]$ system representing a Zr-(Al,Ti)-(Cu,Ni)-Be alloy. The α sites are occupied by blue spheres, the β sites are occupied by purple spheres and the γ sites are occupied by orange spheres. Pink Zr solvent spheres form relaxed icosahedra around each α solute [90].

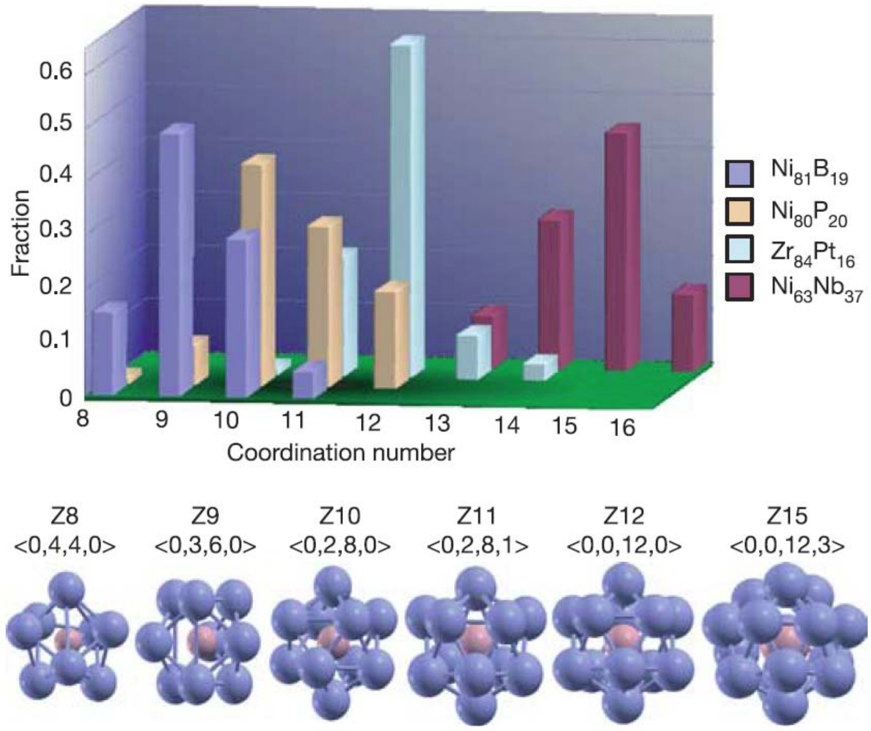

Fig. 2-4. The coordination number distribution of the solute atoms in several representative metallic glasses obtained from ab initio calculations [23].

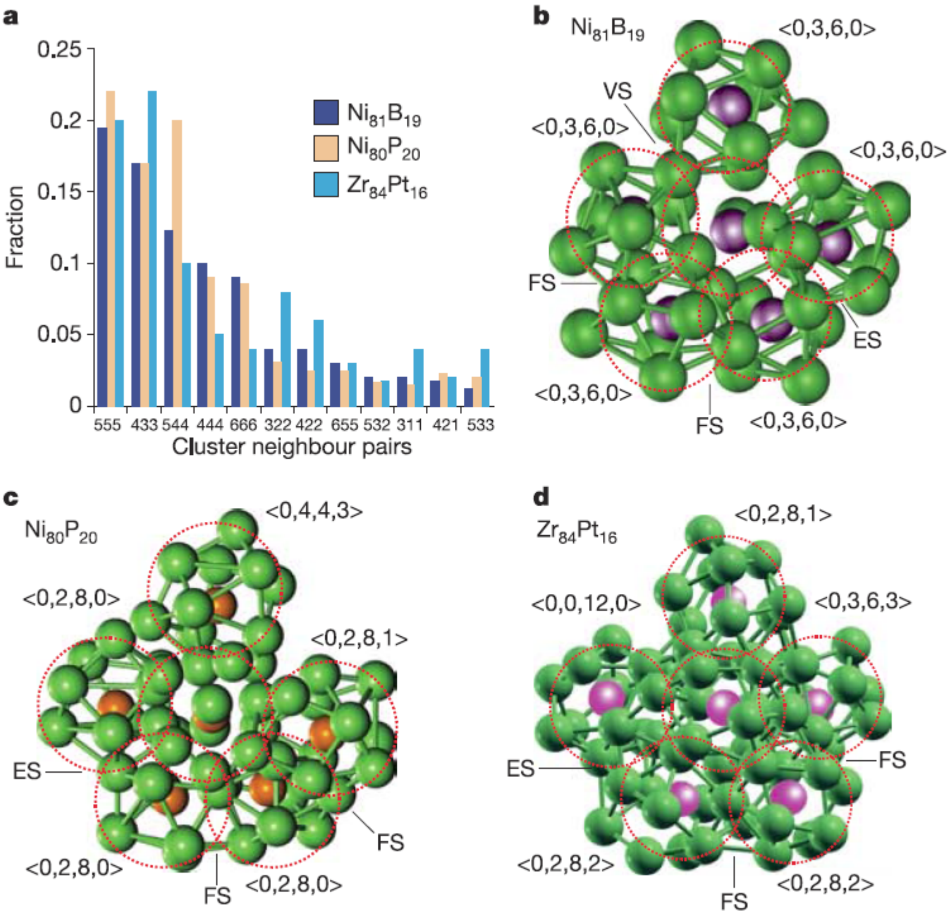

Fig. 2-5. The packing of the solute-centred quasi-equivalent clusters, showing their medium range order. (a) The cluster common-neighbour analysis showing that the local clusters in the metallic glasses exhibit icosahedral type ordering. The typical cluster connections, exhibiting the fivefold symmetry, are detailed for $Ni_{81}B_{19}$, $Ni_{80}P_{20}$ and $Zr_{84}Pt_{16}$ in (b), (c) and (d), respectively [23].

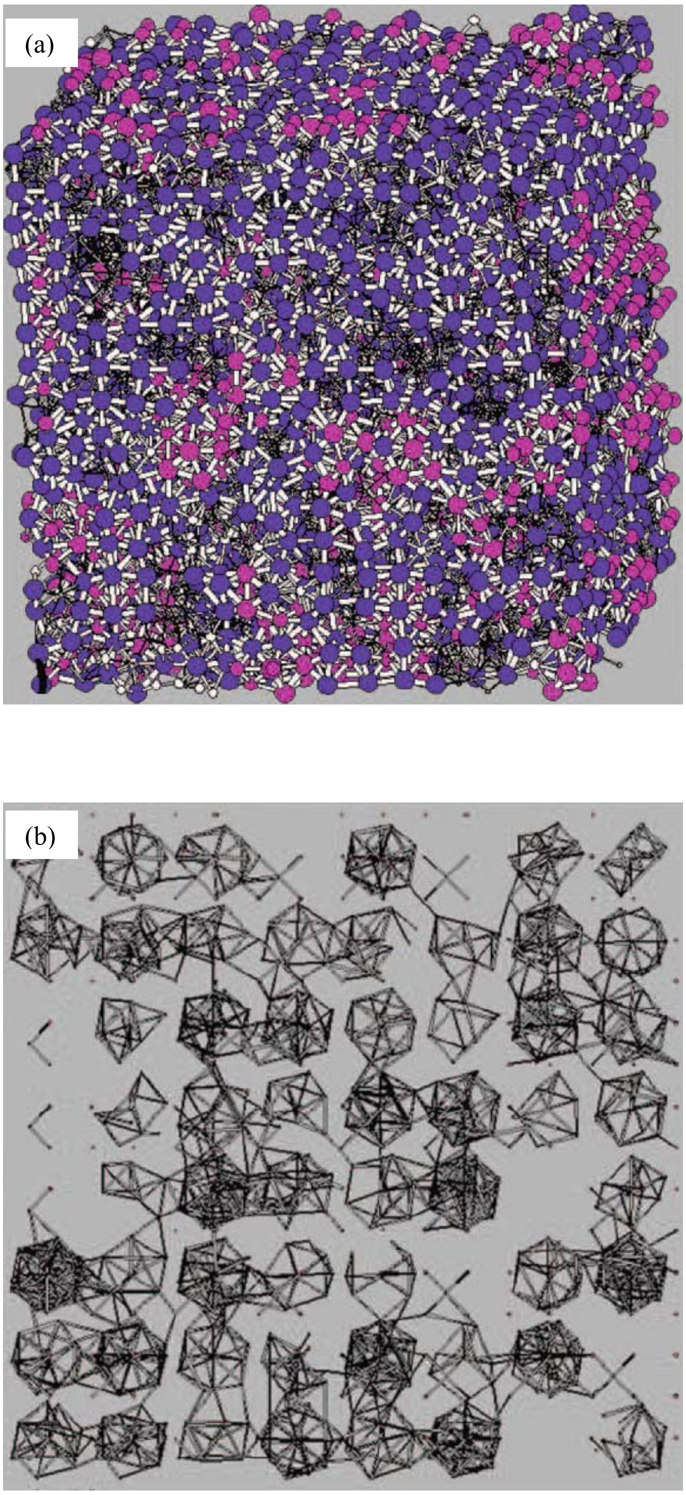

Fig. 2-6. (a) The structure of the as-cast bulk metallic glasses after reverse Monte Carlo refinement, (b) clusters of imperfect icosahedral and cubic forms extracted from [94].

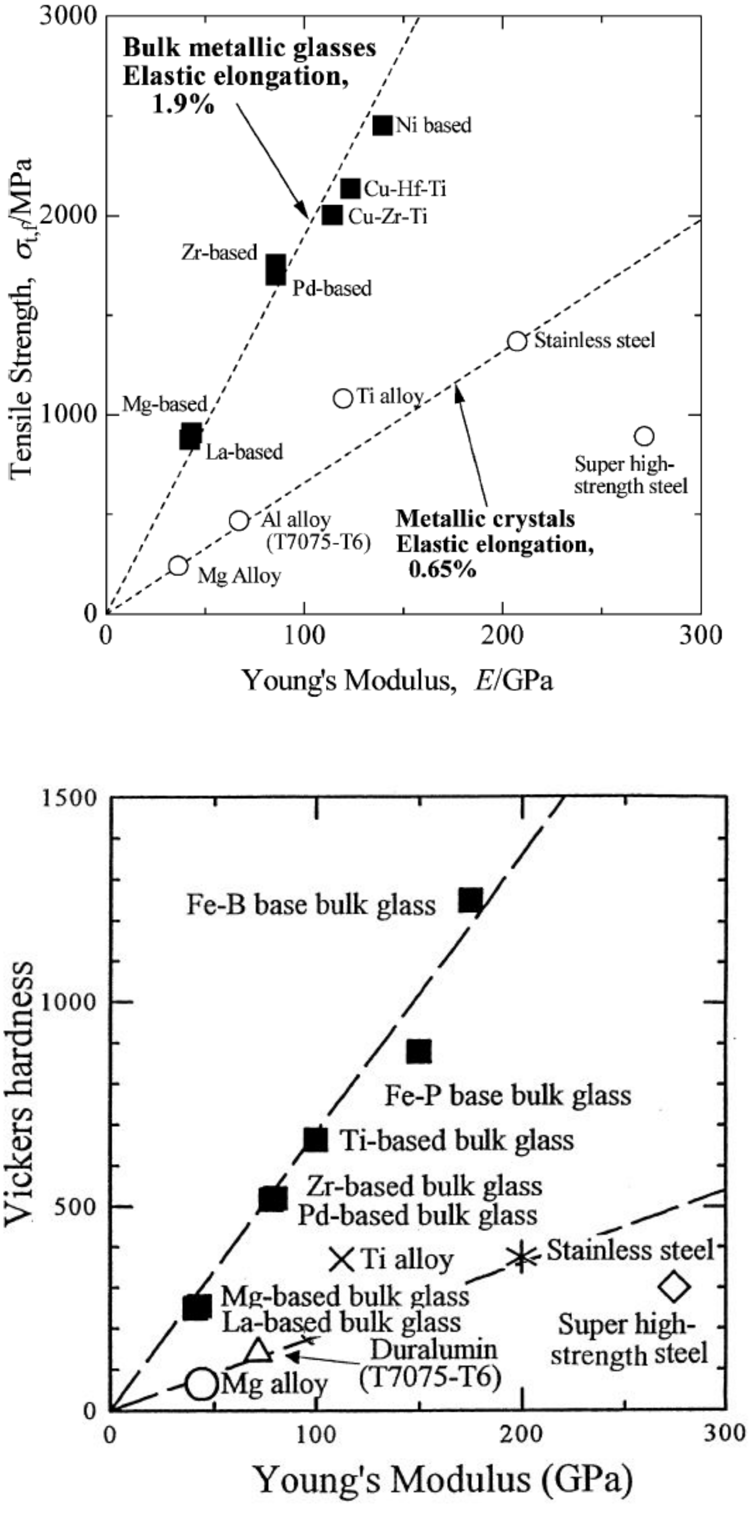

Fig. 2-7. Relationship between tensile strength, Young's modulus, and Vickers hardness for bulk glassy alloys. The data of crystalline metallic alloys are also shown for comparison [54, 190].

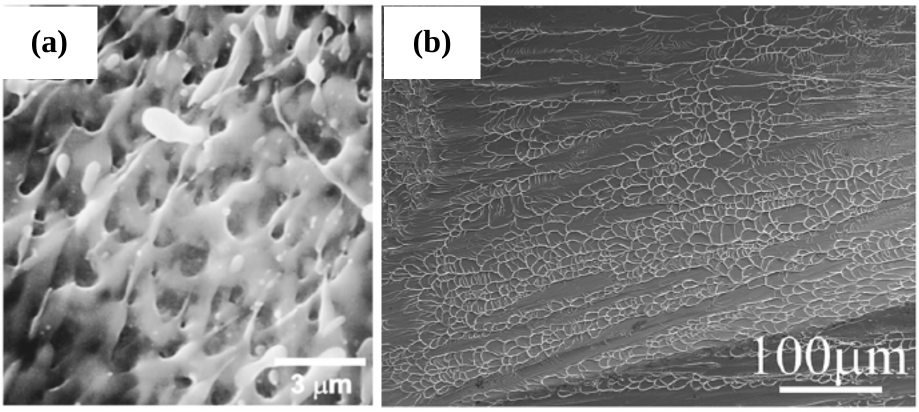

Fig. 2-8. (a) Failure surface from a tensile sample which exhibited cup and cone morphology. The droplets are indicative of localized melting reprinted from [96]. (b) Typical vein pattern on the fracture surface of a ductile $Pd_{30}Ni_{50}P_{20}$ bulk metallic glass subjected to compression testing [191].

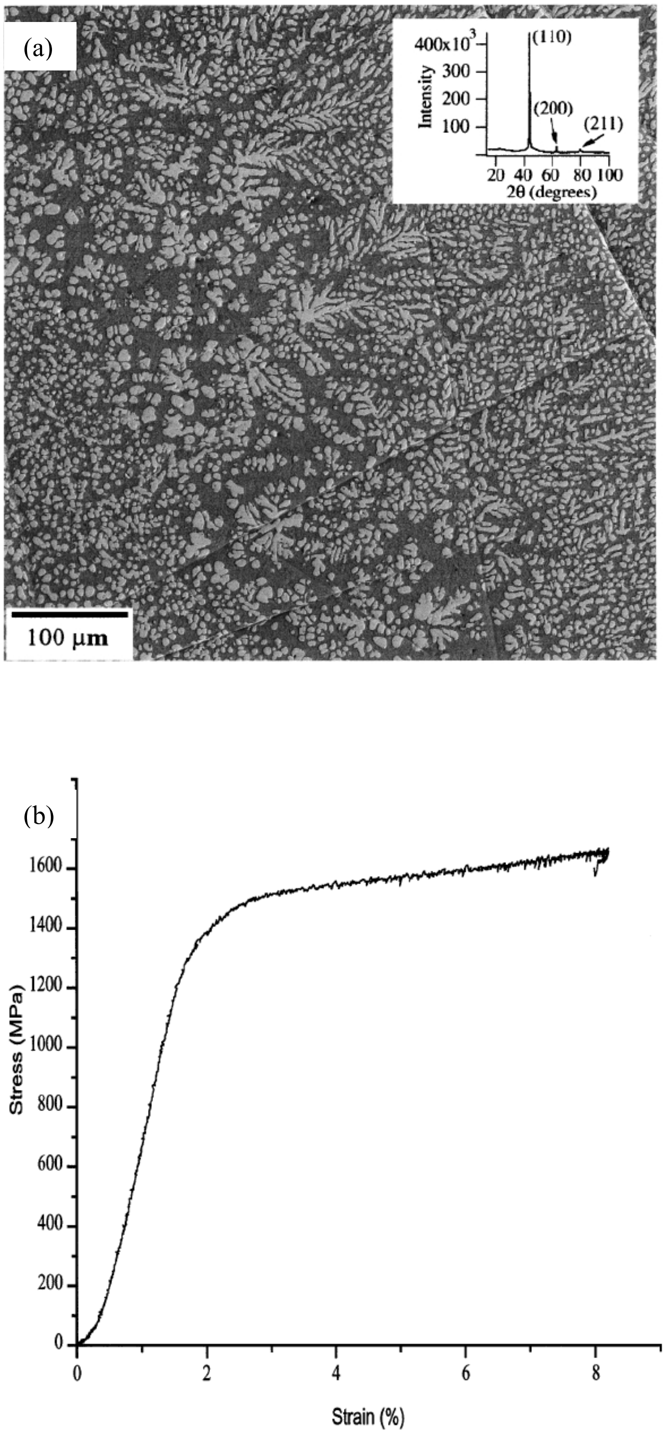

Fig. 2-9. (a) SEM backscattered electron image of in situ composite microstructure. (Inset: X-ray diffraction pattern for Zr-Ti-Nb in situ composite). (b) Compressive stress strain curve for cylindrical in situ composite specimen [100].

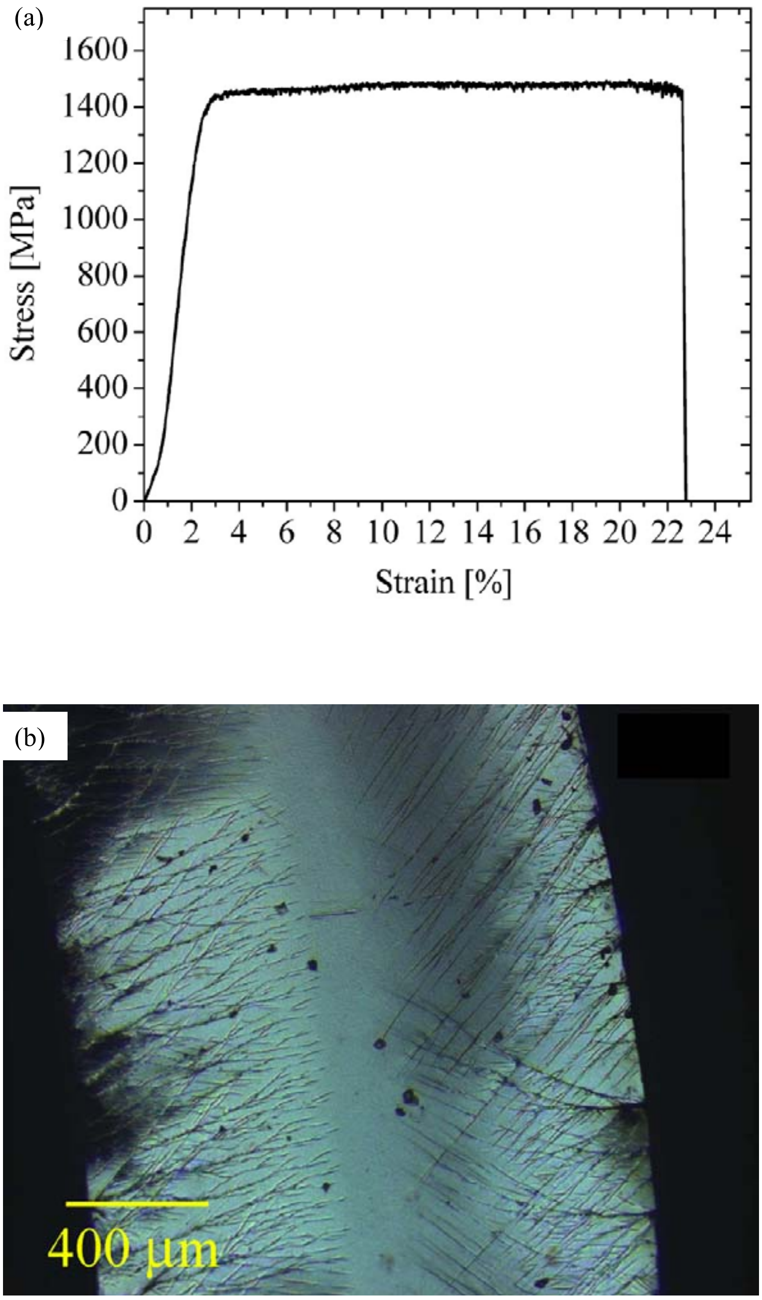

Fig. 2-10. (a) Stress-strain curve of amorphous monolithic Pt-Cu-Ni-P. The curve was determined under quasistatic compression of a bar shaped sample. The material undergoes about 20% plastic deformation before failure. (b) Optical micrograph of the Pt-Cu-Ni-P BMG which was bent over a mandrel of radius 6.35 mm, which corresponds to a strain of about 14% [101].

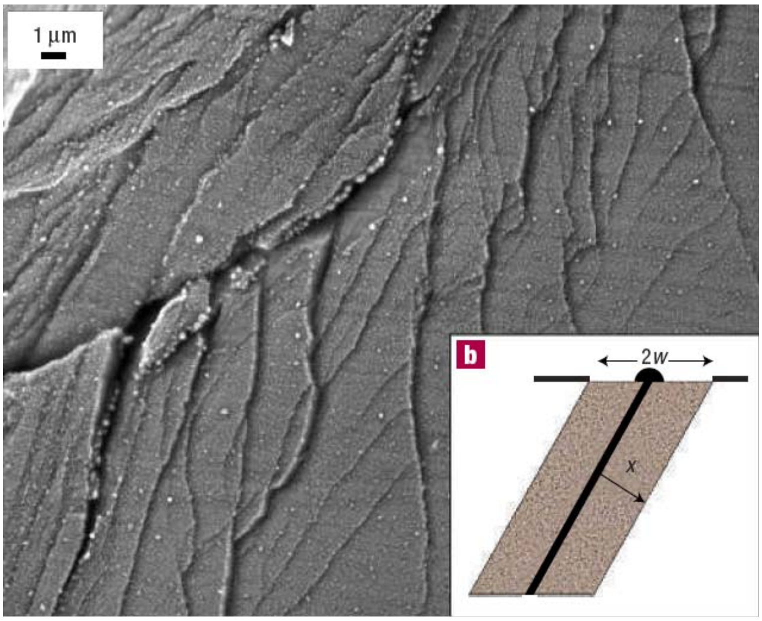

Fig. 2-11. SEM micrograph showing shear bands near a notch in a bend-test specimen coated with tin[131].

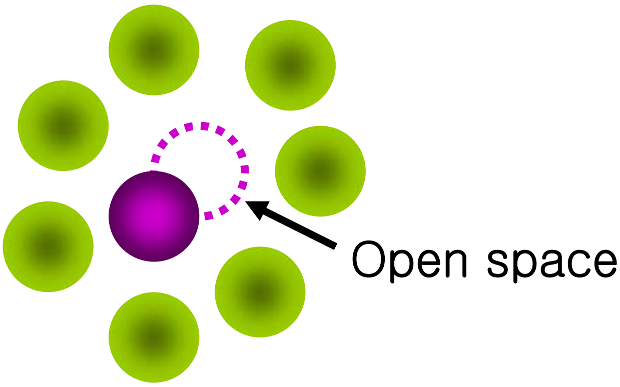

Fig. 2-12. Illustration of free-volume for an atom to move into a open space [105].

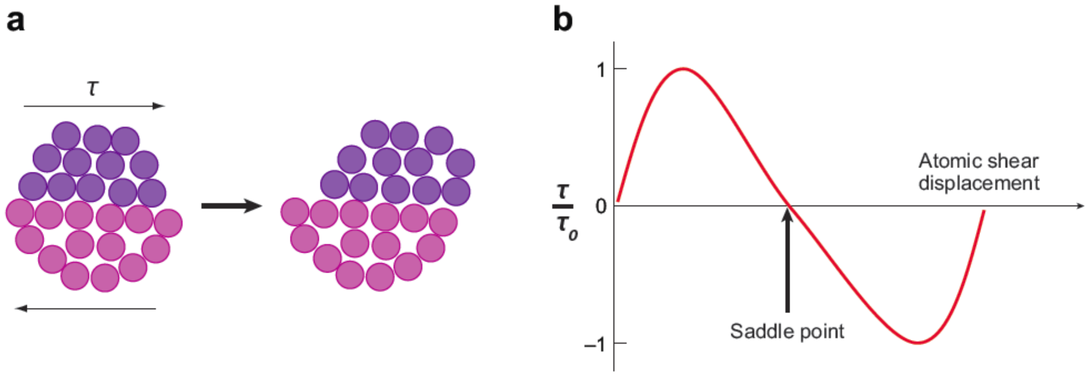

Fig. 2-13. A two dimensional schematic of a shear transformation zone deformation in the amorphous metal. (a) A two-dimensional schematic of a shear transformation zone in an amorphous metal. A shear displacement occurs to accommodate an applied shear stress τ, with the darker upper atoms moving with respect to the lower atoms. (b) The applied shear stress τ necessary to maintain a given atomic shear displacement, normalized by the maximum value of τ at $\sigma_n = 0$, τ_0 [111].

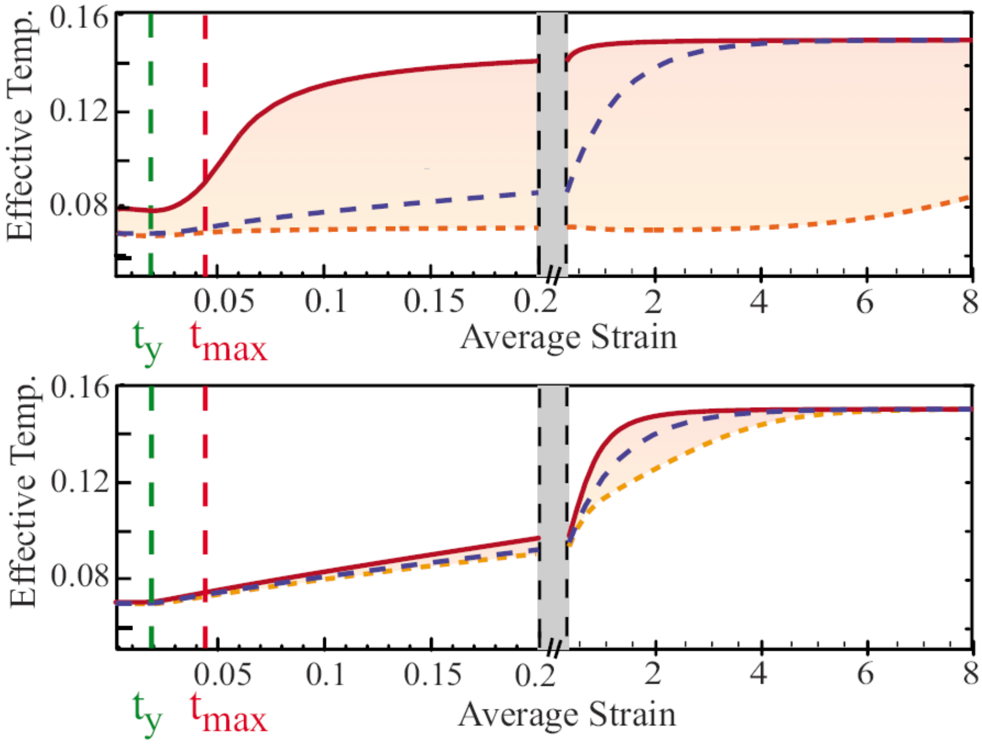

Fig. 2-14. Plot of effective temperature χ as a function of time for (a) an STZ solution for $\delta\chi_0 = 0.01$ that localizes and (b) an STZ solution for $\delta\chi_0 = 0.001$ that does not localize. Dashed vertical lines correspond to calculated values for the time the material first reaches the yield stress, τ_y, and the time the material reaches its maximum stress τ_{max} [118].

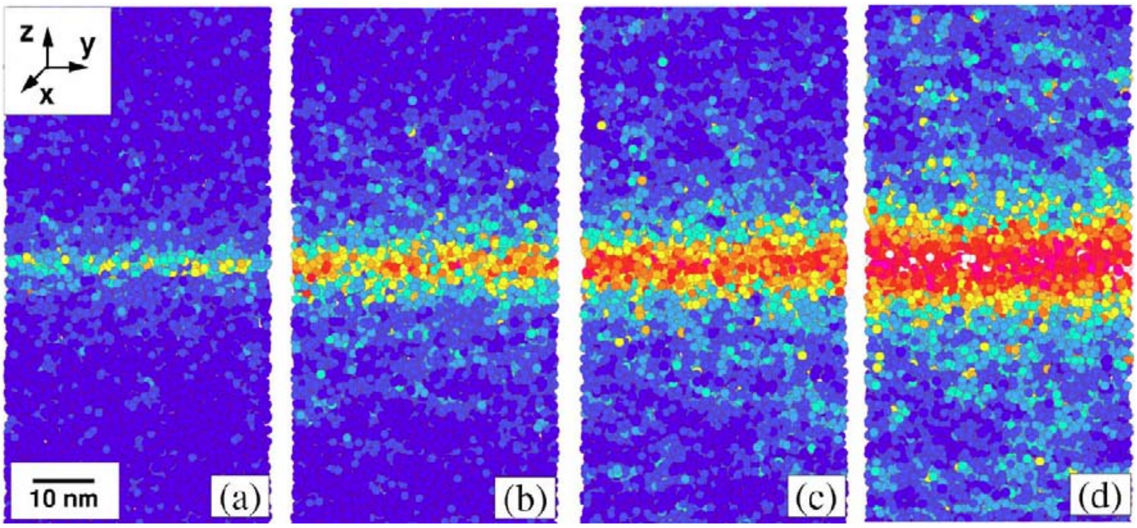

Fig. 2-15. The local shear strain distribution at different mean sample strains, (a) 4.10%, (b) 12.28%, (c) 20.44%, and (d) 40.81%. The color scheme reflects the change in the rotation angle of the nearest atomic bonds. Only a small section containing the shear band and its immediate vicinity is shown in the sample containing 288000 atoms arranged in a 49.73×4.07×97.60 nm^3 rectangular box [110].

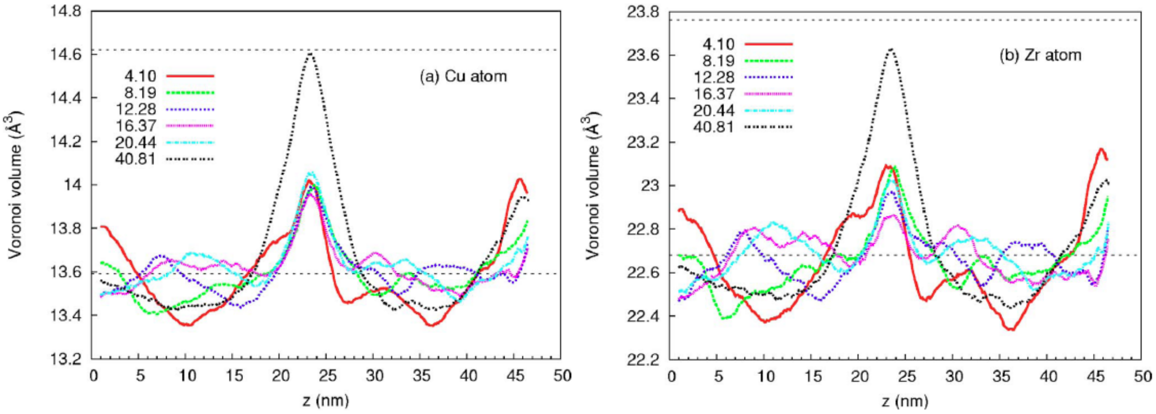

Fig. 2-16. The Voronoi volume distributions for (a) Cu and (b) Zr atoms at different mean sample shear strains (%). The lower dotted lines are the Voronoi volumes of the undeformed samples at 300 K and the upper dotted lines are the volumes of the undercooled liquid at T_g. The changes due to the finite size at the sample boundaries can be seen [110].

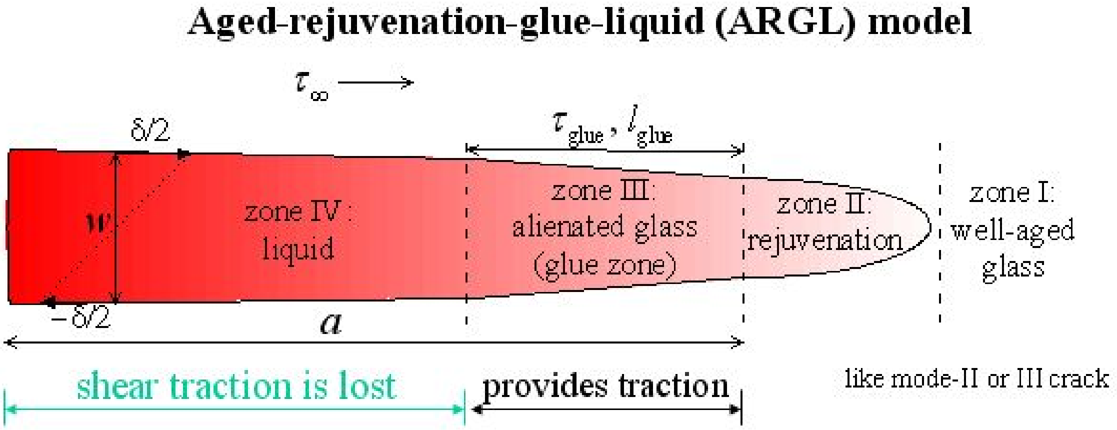

Fig. 2-17. Aged-rejuvenation-glue-liquid (ARGL) model of shear band in BMGs. The shading represents temperature [128].

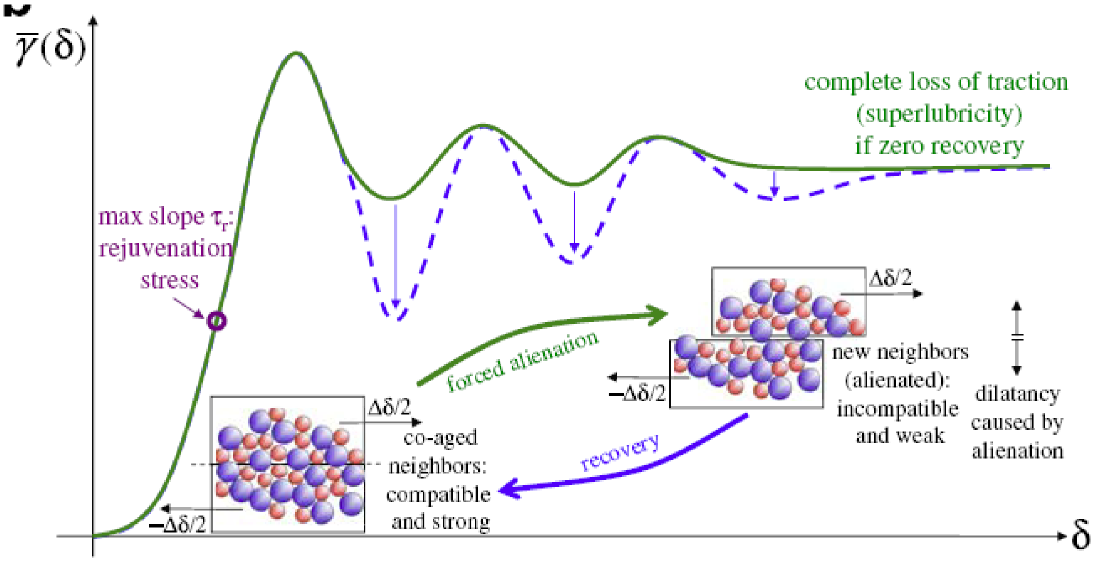

Fig. 2-18. GSF γ(δ) of a glass as a function of a sharp displacement discontinuity δ. The solid curve illustrates the behavior without any recovery process. The dashed curve shows that, as time increases, recovery occurs and the energy traps get deeper [128].

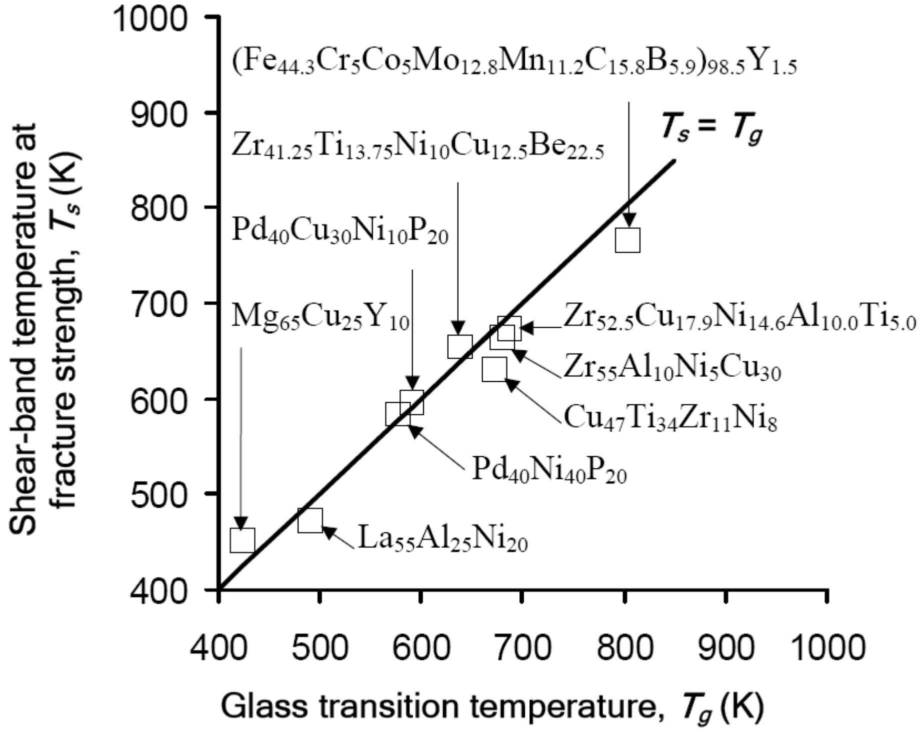

Fig. 2-19. Comparison between glass-transition temperature and calculated shear-band temperature at fracture strength for different bulk metallic glasses [133].

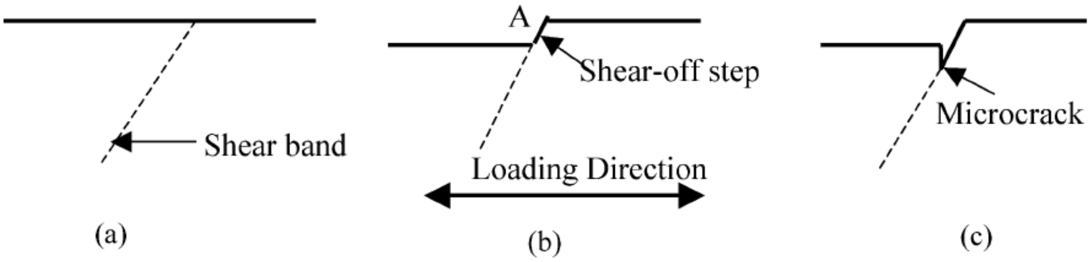

Fig. 2-20. A proposed fatigue-crack-initiation mechanism: (a) formation of shear band, (b) formation of shear-off step, and (c) microcrack initiation [42, 43].

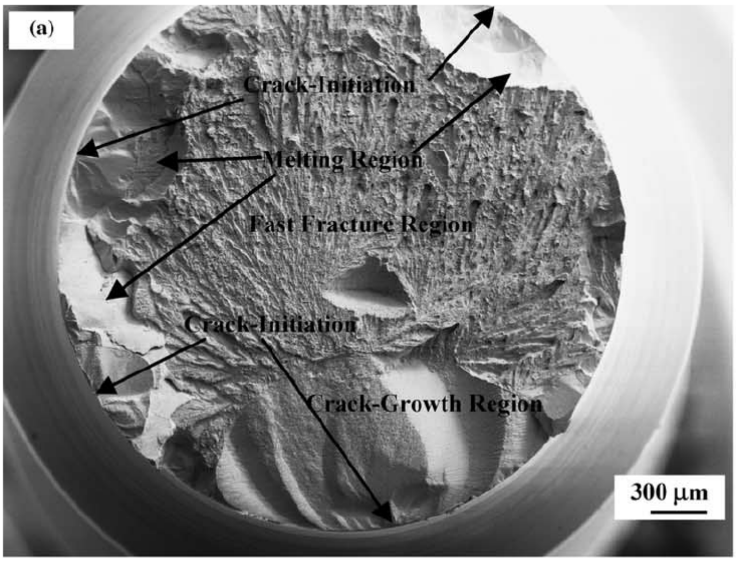

Fig. 2-21. The fatigue fracture surface of the $Zr_{50}Al_{10}Cu_{40}$ specimen was tested at σ_{max} = 1. 2 GPa in vacuum. The whole fatigue fracture surface consisted of four main regions [42, 43]: the fatigue-crack-initiation, crackpropagation, final-fast-fracture, and apparent-melting fareas.

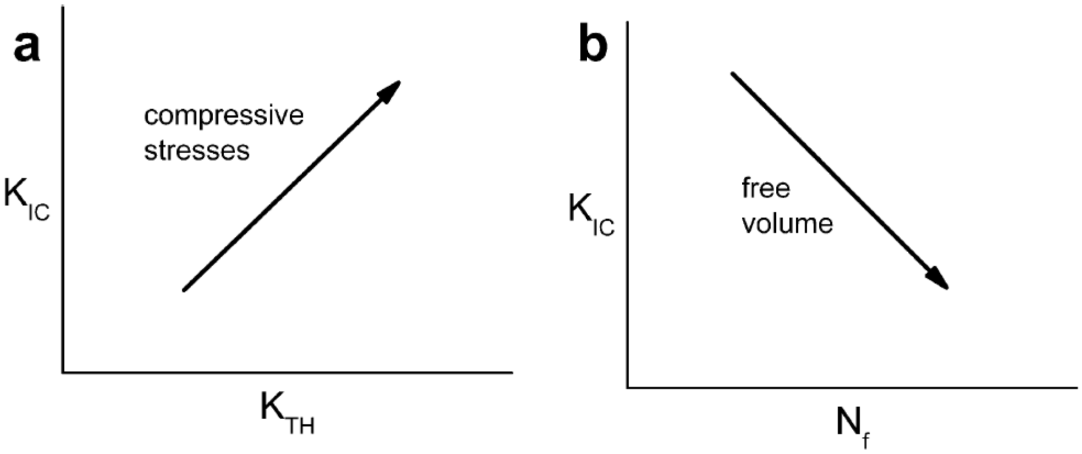

Fig. 2-22. Schematic illustrating how overall alteration of the fatigue and fracture properties in BMGs can be obtained by concurrently controlling [139]: (a) residual stresses to improve both the fatigue threshold, K_{TH}, and the fracture toughness, K_{IC}, and (b) the free volume to improve the fatigue limit but degrade the fracture toughness, K_{IC}.

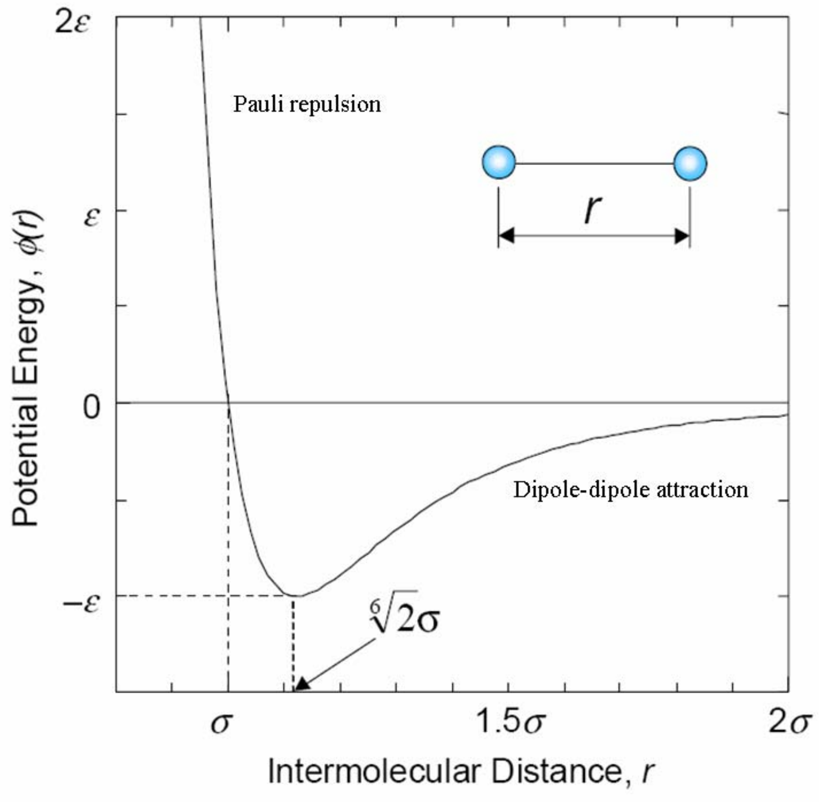

Fig. 3-1. Form of the Lennard-Jones (12-6) potential which describes the interaction of two inert gas atoms [143].

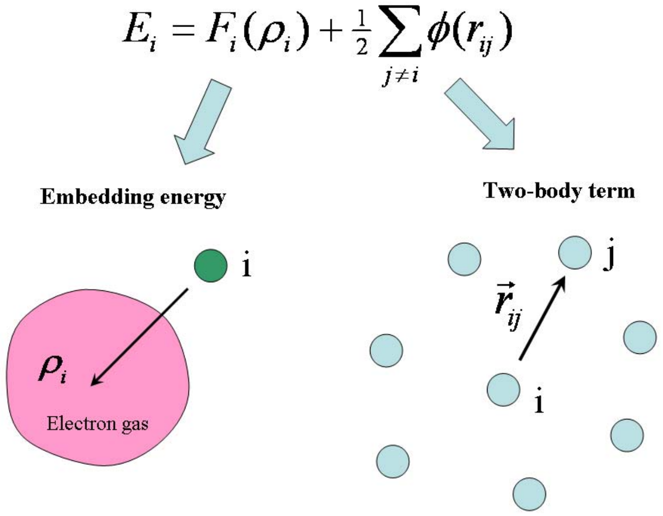

Fig. 3-2. The energy of the atom *i* is determined by the local electron density at the position of i atom and the ρ_i describes the contribution to the electronic density at the site of the atom *i* from all atoms *j*.

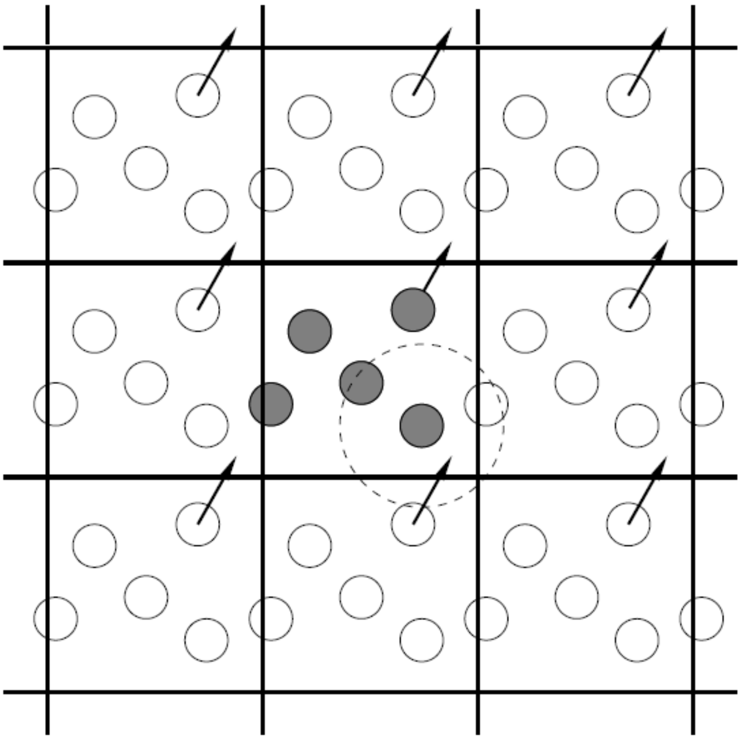

Fig. 3-3. Periodic boundary conditions. As a particle moves out of the simulation box, an image particle moves in to replace it. In calculating particle interactions within the cutoff range, both real and image neighbors are included [153].

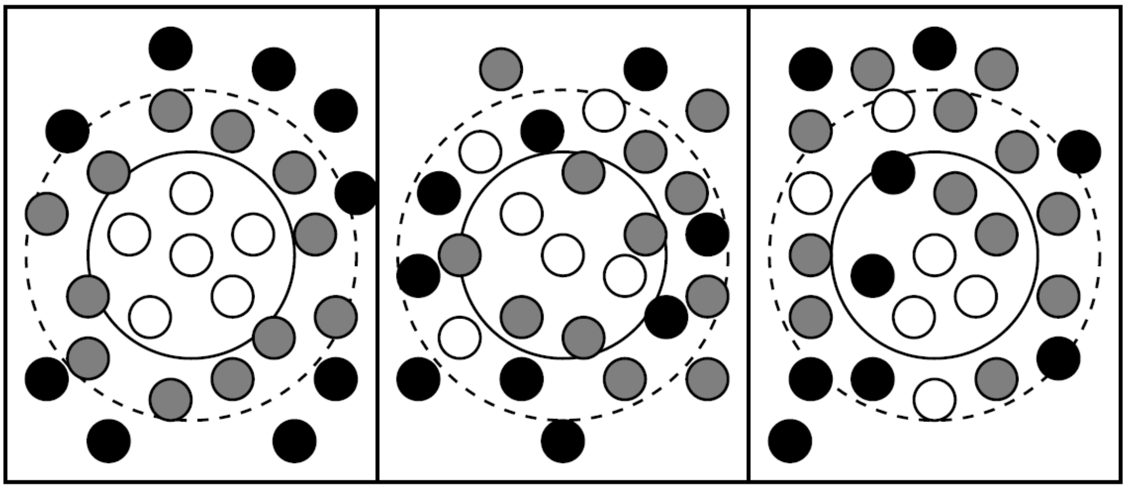

Fig. 3-4. The Verlet list on its construction, later, and too late. The potential cutoff range within r_c (solid circle), and the list range within r_v (dashed circle), are indicated. The list must be reconstructed before particles originally outside the list range (black) have passed the potential cutoff sphere[153].

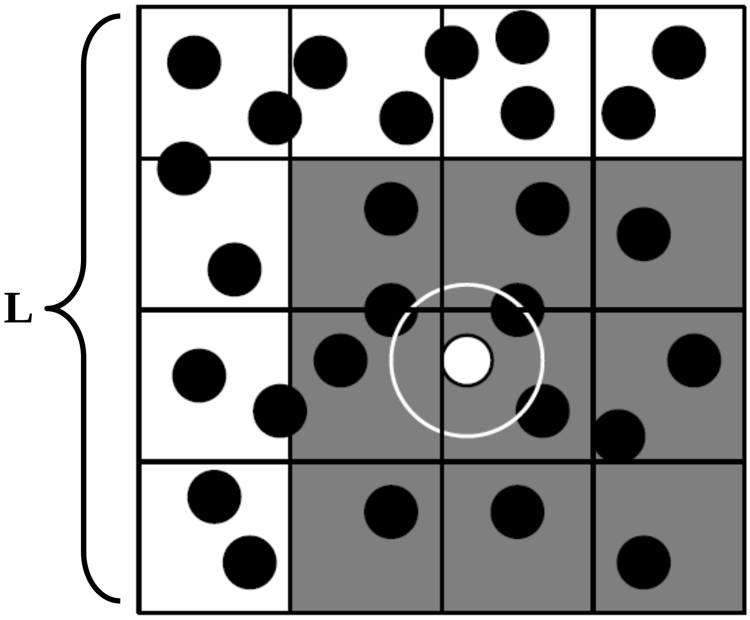

Fig. 3-5. The cell structure. The potential cutoff range is indicated. In searching for neighbours of an atom, it is only necessary to examine the atom's own cell, and its nearest-neighbour cells (shaded) [153].

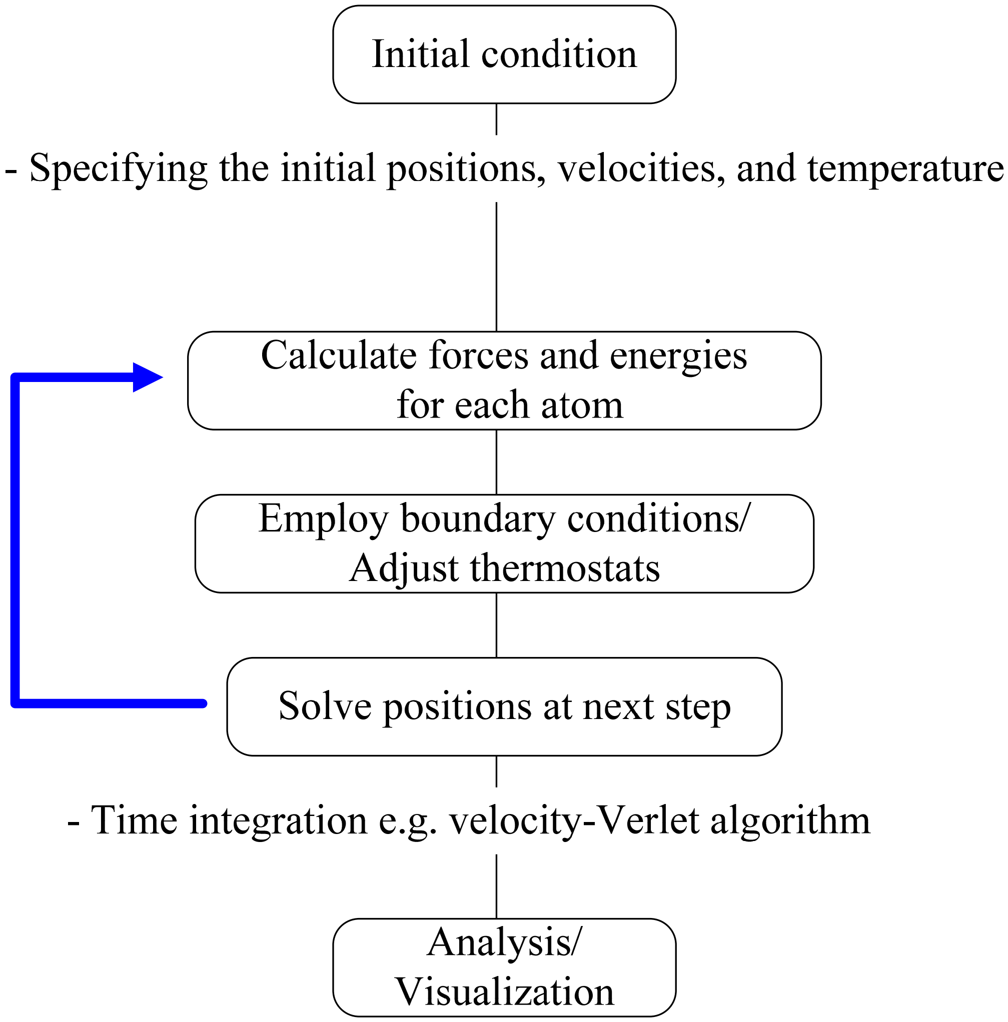

Fig. 3-6. Flow chart of molecular dynamics simulation.

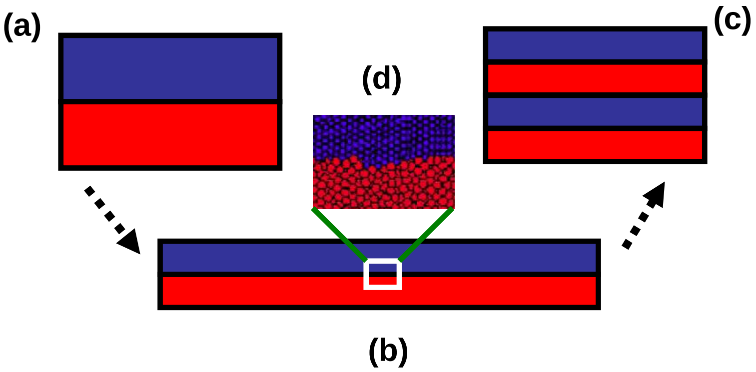

Fig. 4-1. A schematic representation of the simulated strain-and-stack process: (a) two of crystalline elemental bilayer structures (b) are elongated to twice its original length and half its original thickness and (c) subsequently halved along the solid line and stacked atop itself. The inset (d) shows a typical atomic structure at their interfaces [176].

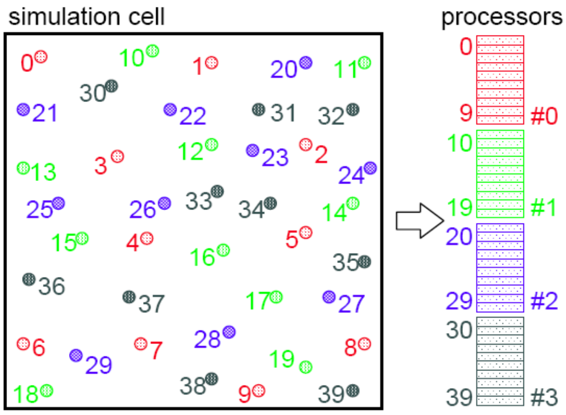

(a) Particle decomposition method

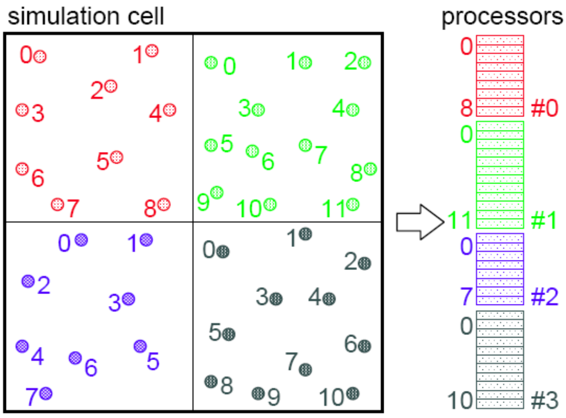

(b) Spatial decomposition method

Fig. 4-2. Two decomposition methods for parallel MD: (a) is particle decomposition method, and (b) is spatial decomposition method; each forty particles are allotted to 4 processors [155].

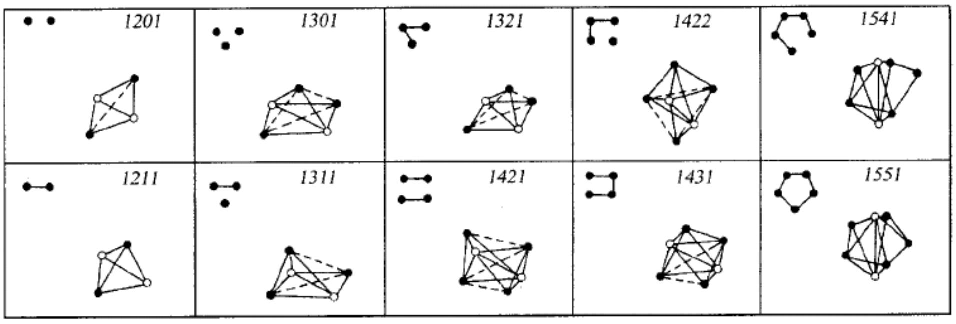

Fig. 4-3. The schematic drawing of the related HA pairs [159].

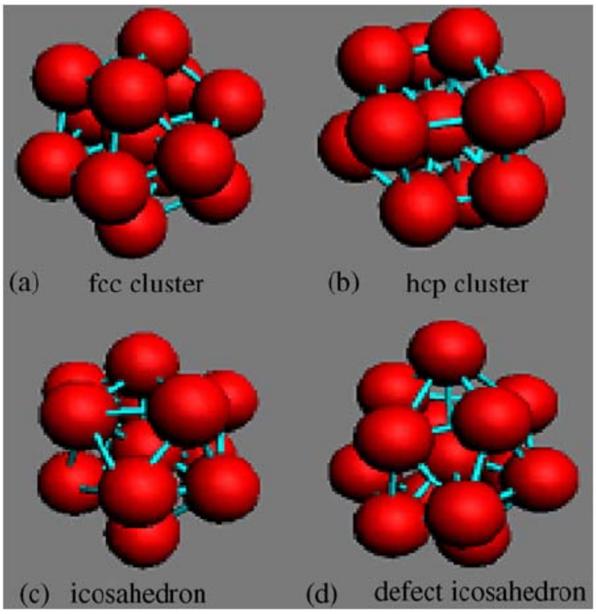

Fig. 4-4. Different type of clusters formed in crystals and glasses [158].

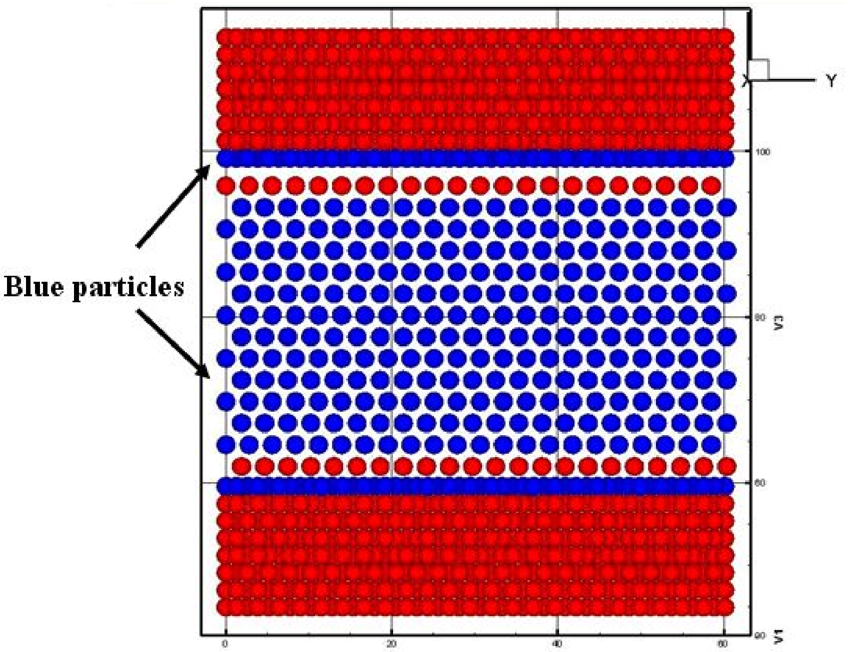

Fig. 4-5. The scheme of the initial Mg-Cu simulation model. The blue particles represent Mg atoms and red particles represent Cu atoms.

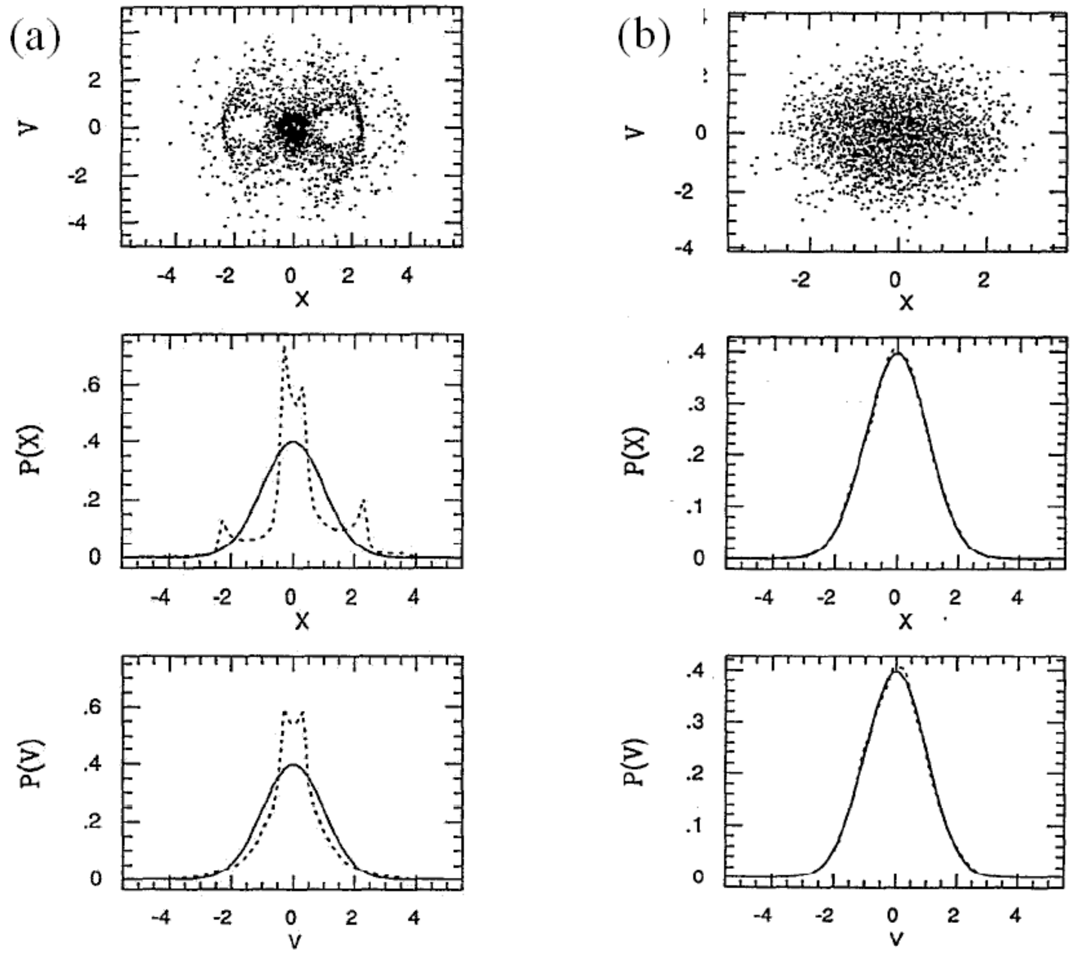

Fig. 4-6 (a) Density map V, position P(x) and velocity P(V) distribution functions obtained from Nosé-Hoover dynamics of a harmonic oscillator (dotted line). The solid line is the exact result. (b) Those three properties of a harmonic oscillator obtained from the Nosé-Hoover chain dynamics (dotted line). The solid line is the exact result [166, 167].

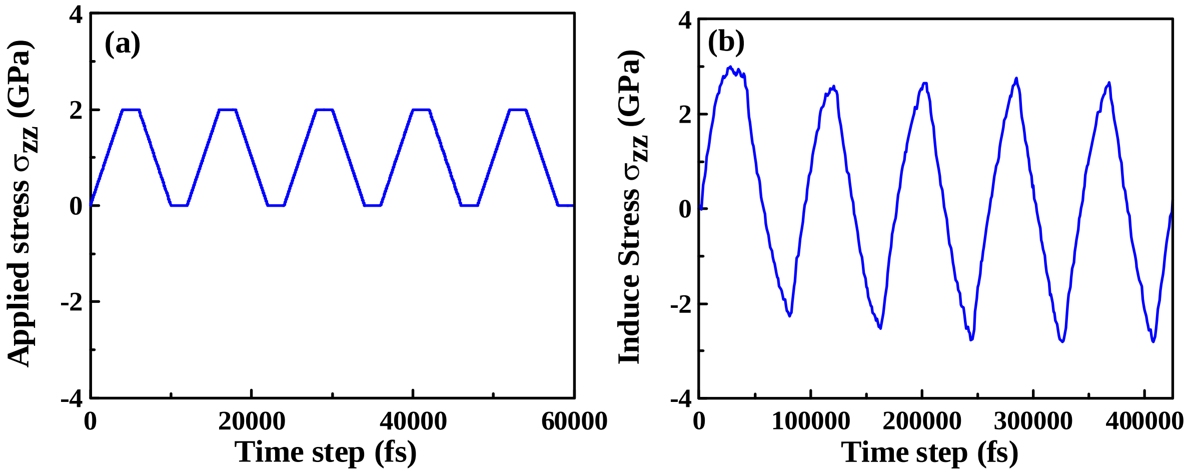

Fig. 4-7. Fatigue-loading conditions during MD simulations of Zr-Cu metallic glass: (a) the stress-control mode for a tension fatigue experiment at σ_{max} = 2 GPa, and (b) the strain-control mode for a tension-compression fatigue experiment at ε_{max} = 10% (showing the induced stress amplitude).

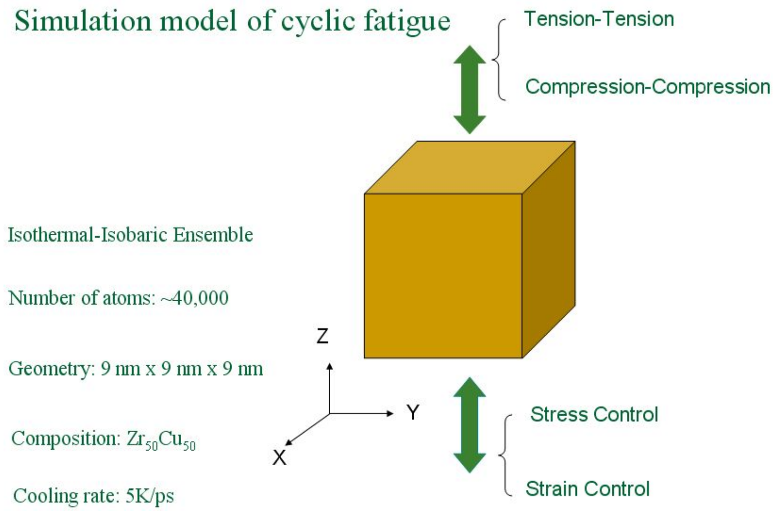

Fig. 4-8. Illustration of simulation model in cyclic loading fatigue.

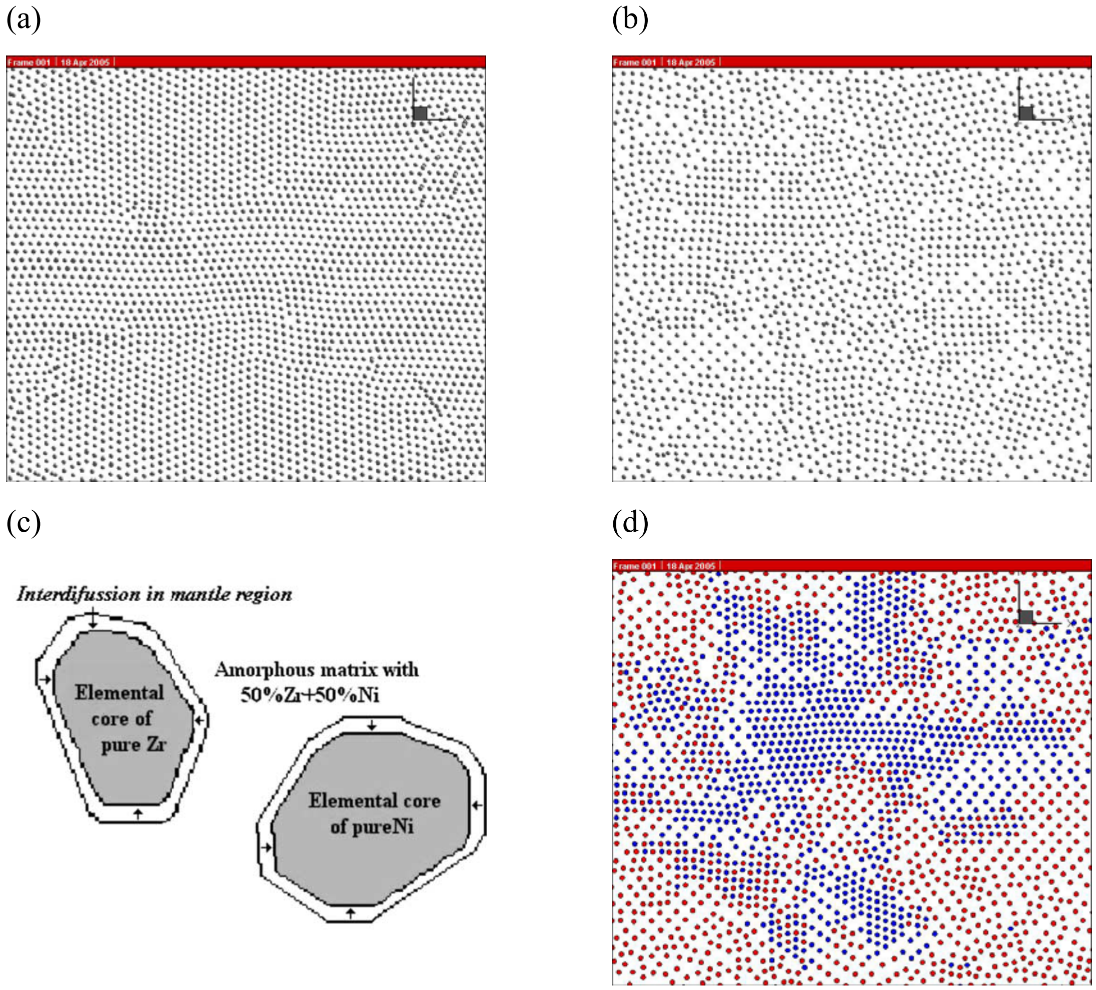

Fig. 5-1. The 2-D sliced plots parallel to the xz plane of the Zr-Ni metallic layers for (a) Ni layer and (b) Zr layer, rrespectively. (c) Schematic illustration of the transformation mechanism via interdiffusion, and (d) the interface between Ni grain (blue particles) and Zr grain (red particles).

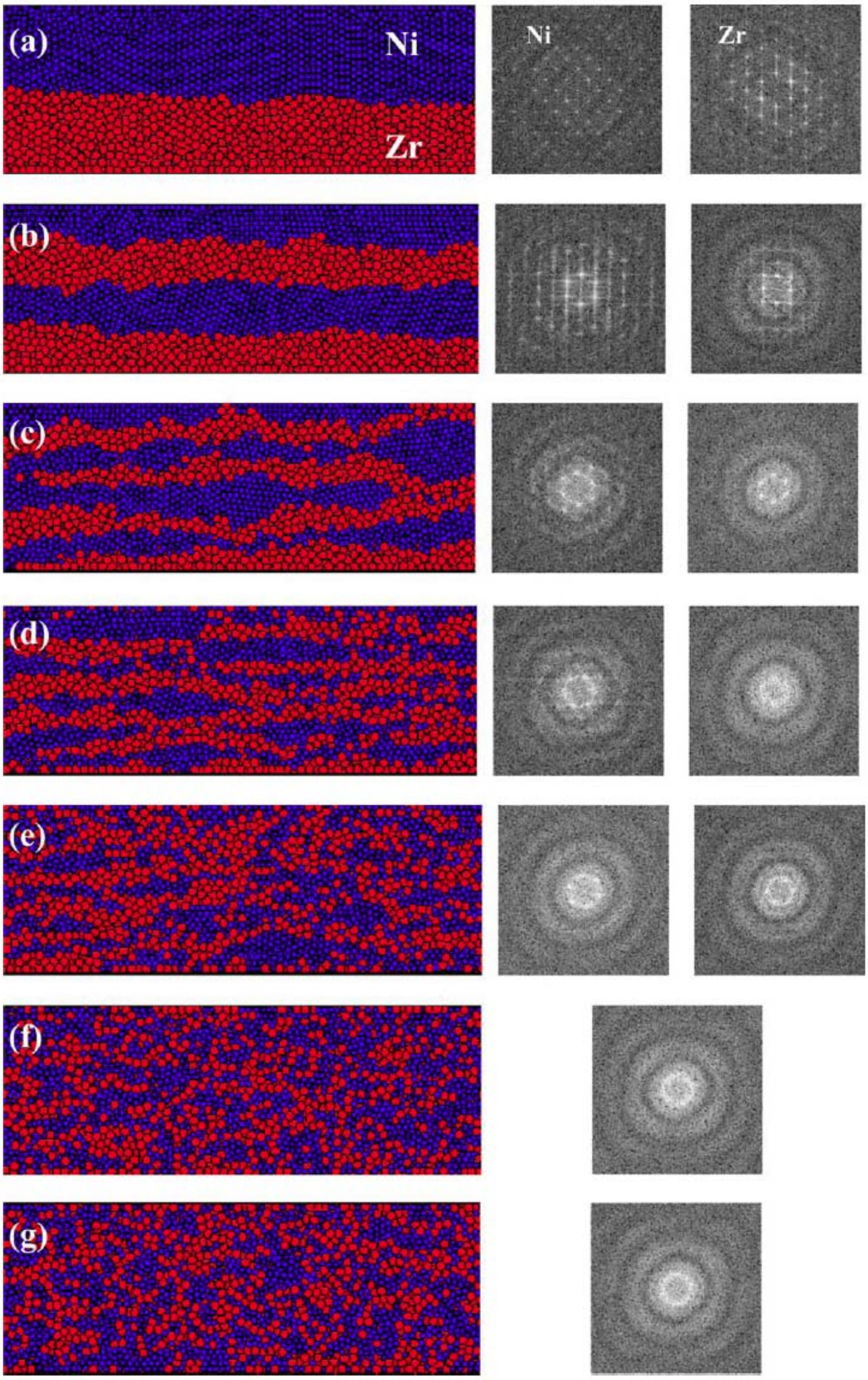

Fig. 5-2. The microstructural evolution and the associated two-dimensional Fourier transform of bi-layered $Zr_{32}Ni_{68}$ model subjected to various ARB cycles: (a) initial state, (b) 1, (c) 2, (d) 3, (e) 4, (f) 5 and (g) 6 ARB cycles.

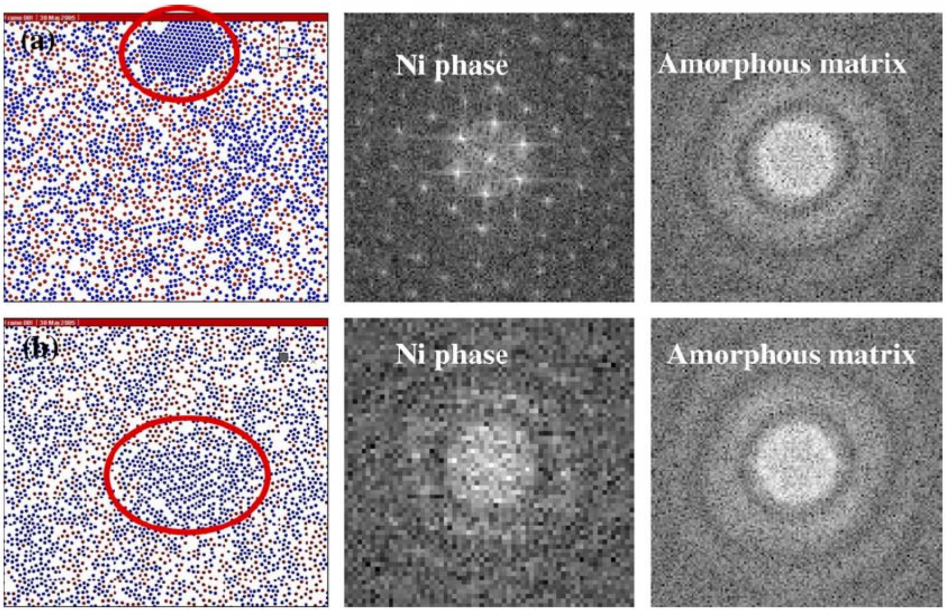

Fig. 5-3. The microstructural evolution and the associated two-dimensional Fourier transform of the bi-layered $Zr_{50}Ni_{50}$ model subjected to (a) 8 and (b) 9 F&R cycles.

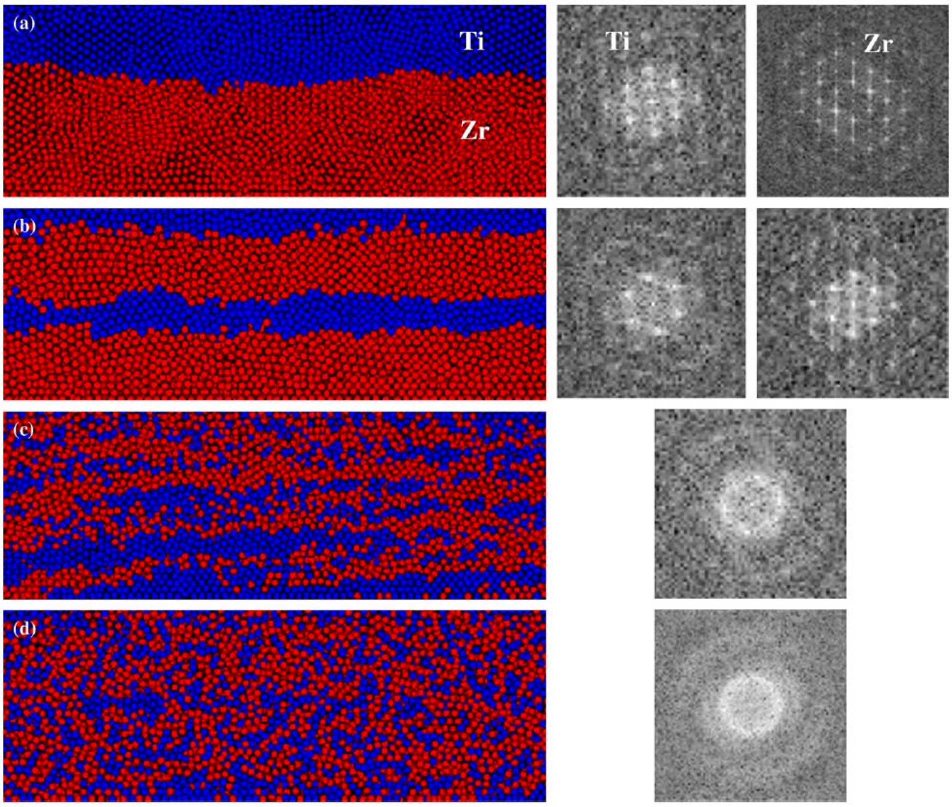

Fig. 5-4. The microstructural evolution and the associated two-dimensional Fourier transform of the bi-layered $Zr_{50}Ti_{50}$ model subjected to various ARB cycles: (a) initial state, (b) 1, (c) 4, and (d) 6 F&R cycles.

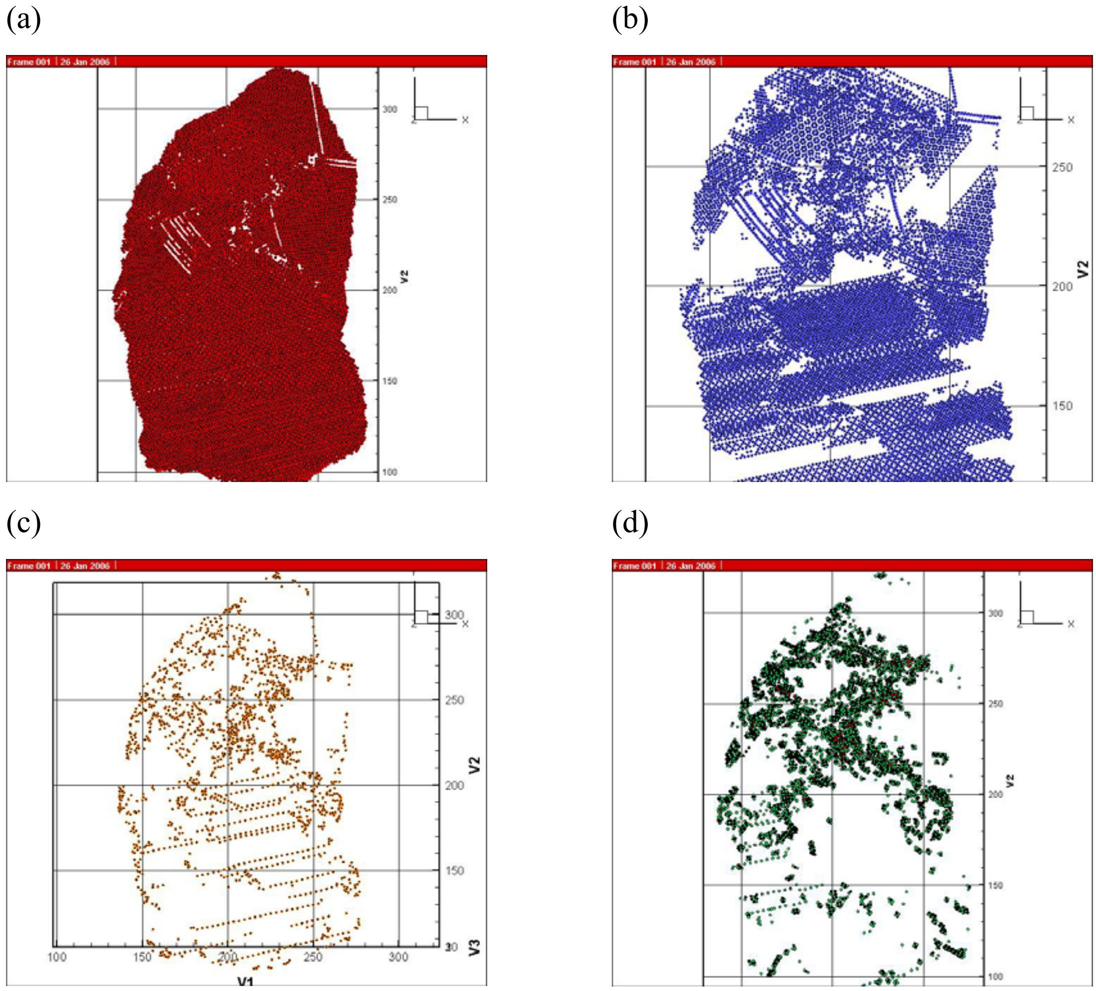

Fig. 5-5 Microstructures of pure Zr upon the end of second cycle at the condition of strain rate at 8.35×10^{8} s^{-1}, (a) composed of 1421 HA pairs, (b) composed of 1422 HA pairs, (c) composed of 1321 HA pairs, and (d) composed of 1431, 1541, and 1551 HA pairs

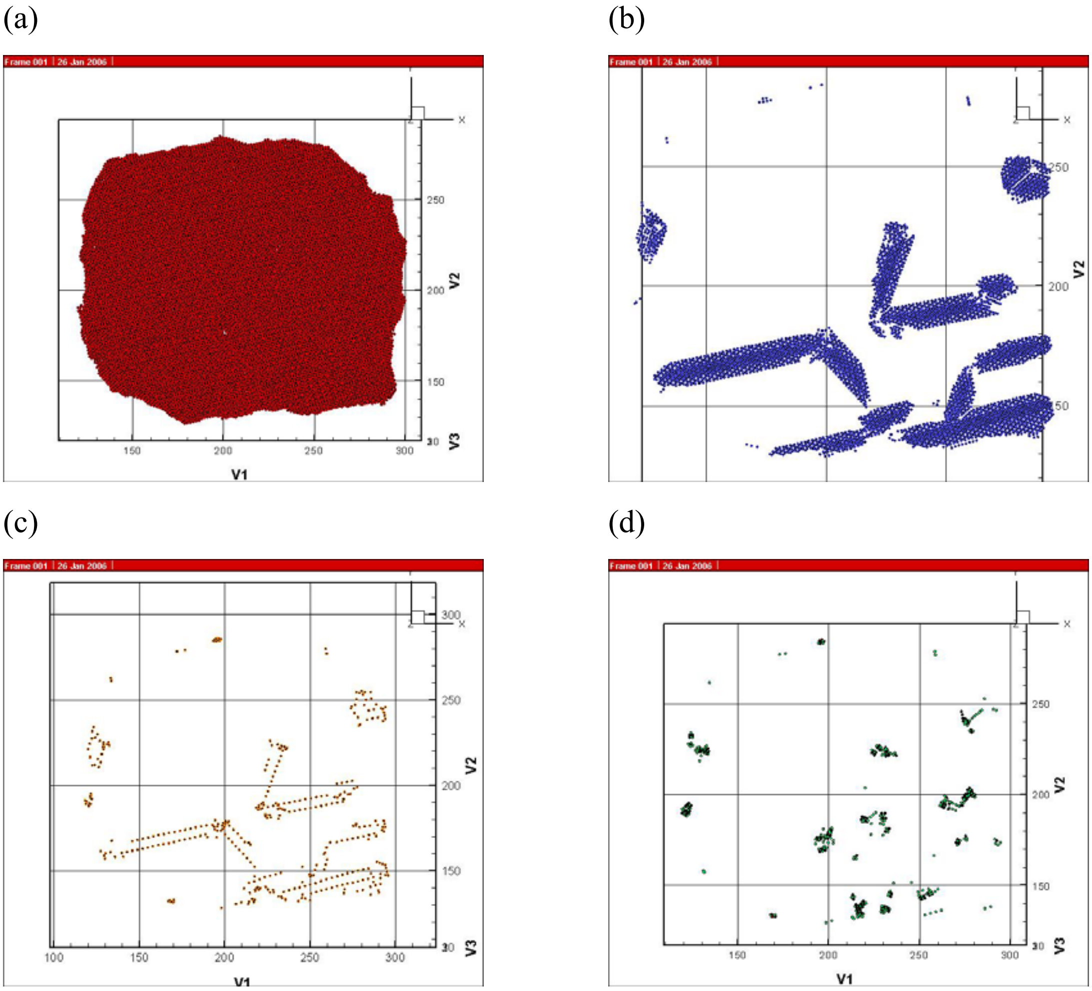
(a) (b) (c) (d)

Fig. 5-6 Microstructures of pure Zr upon the end of 7th cycle at the condition of strain rate at 8.35×10^{8} s^{-1}, (a) composed of 1421 HA pairs, (b) composed of 1422 HA pairs, (c) composed of 1321 HA pairs, and (d) composed of 1431, 1541, and 1551 HA pairs.

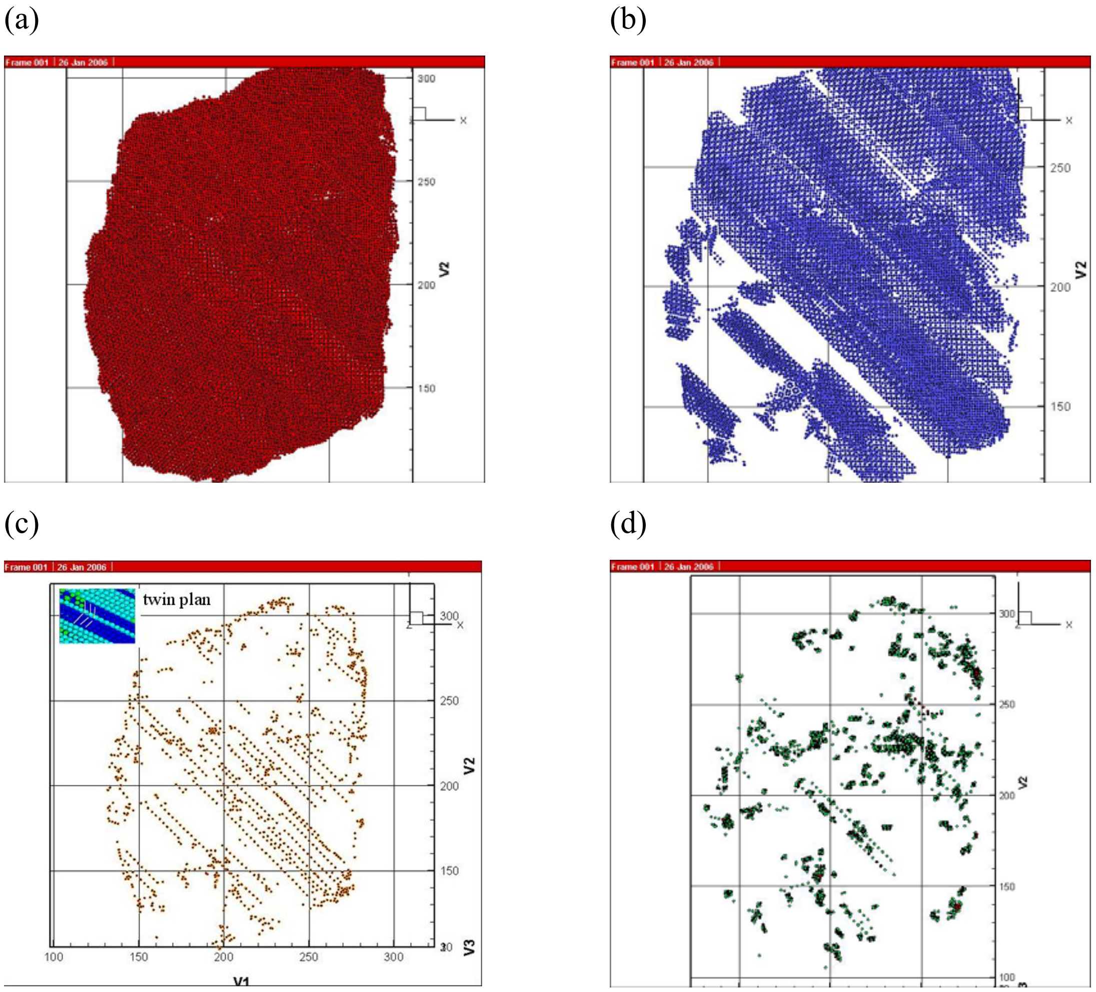

Fig. 5-7 Microstructures of pure Zr upon the end of 7th cycle at the condition of strain rate at 8.35×10^{8} s^{-1}, (a) composed of 1421 HA pairs, (b) composed of 1422 HA pairs, (c) composed of 1321 HA pairs, and (d) composed of 1431, 1541, and 1551 HA pairs. Inset in the corner at (c) show an amplification of twin plan in the Zr matrix.

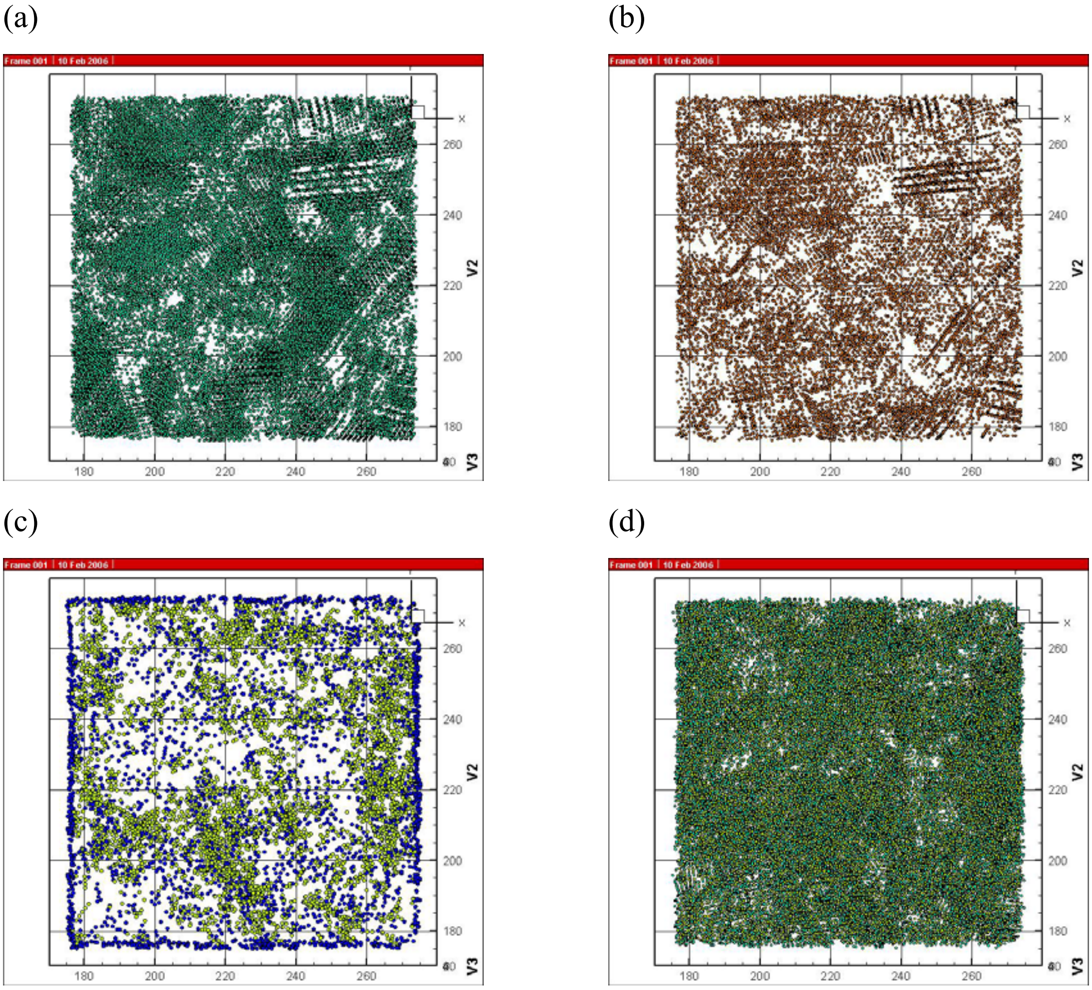

Fig. 5-8 Microstructures of pure Zr upon the end of first cycle at the condition of strain rate at 9.25×10^{9} s^{-1}, (a) composed of 1421 HA pairs, (b) composed of 1422 HA pairs, (c) composed of 1321 and 1551 HA pairs (dominated in the icosahedrons), and (d) composed of 1431, 1541, and 1551 HA pairs.

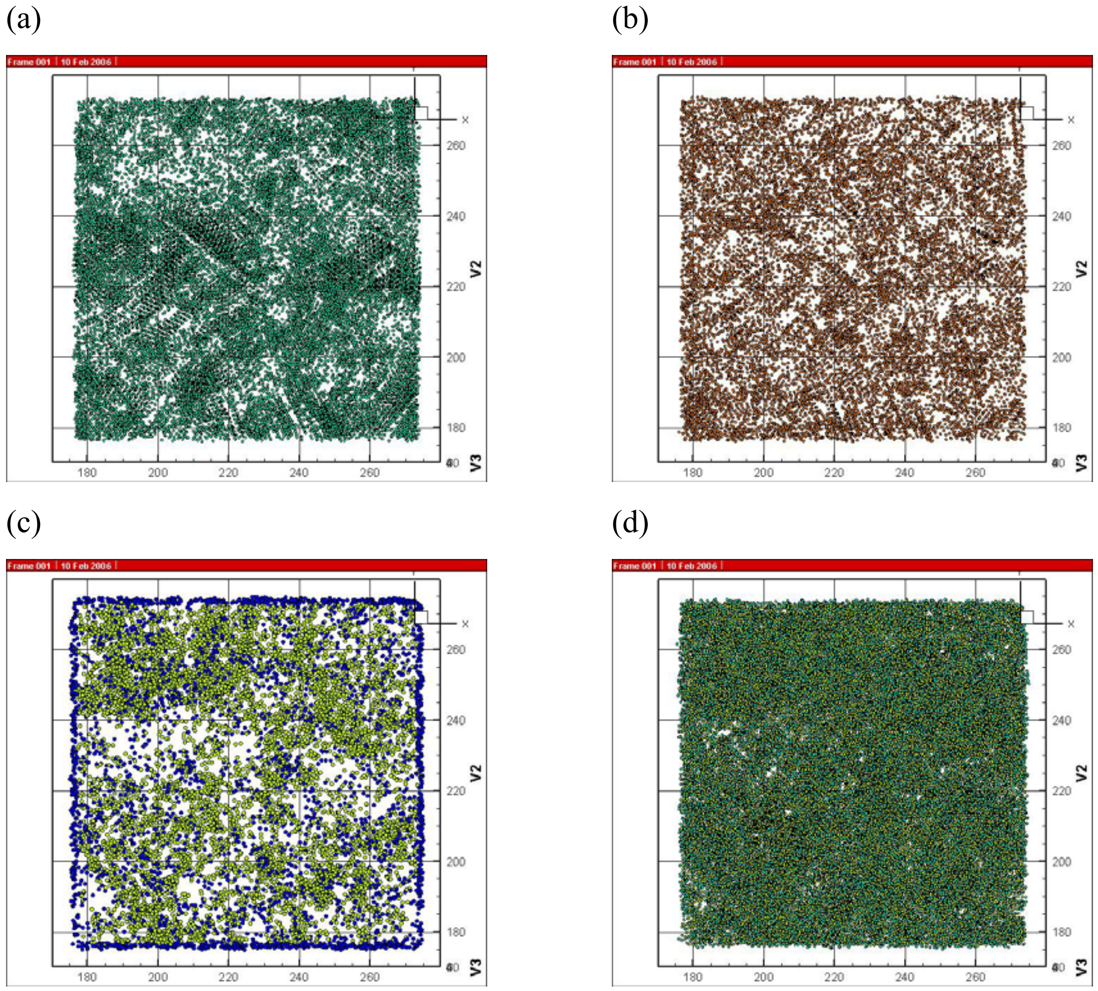

Fig. 5-9. Microstructures of pure Zr upon the end of 13th cycle at the condition of strain rate at 9.25×10^{9} s^{-1}, (a) composed of 1421 HA pairs, (b) composed of 1422 HA pairs, (c) composed of 1321 and 1551 HA pairs (dominated in the icosahedrons), and (d) composed of 1431, 1541, and 1551 HA pairs.

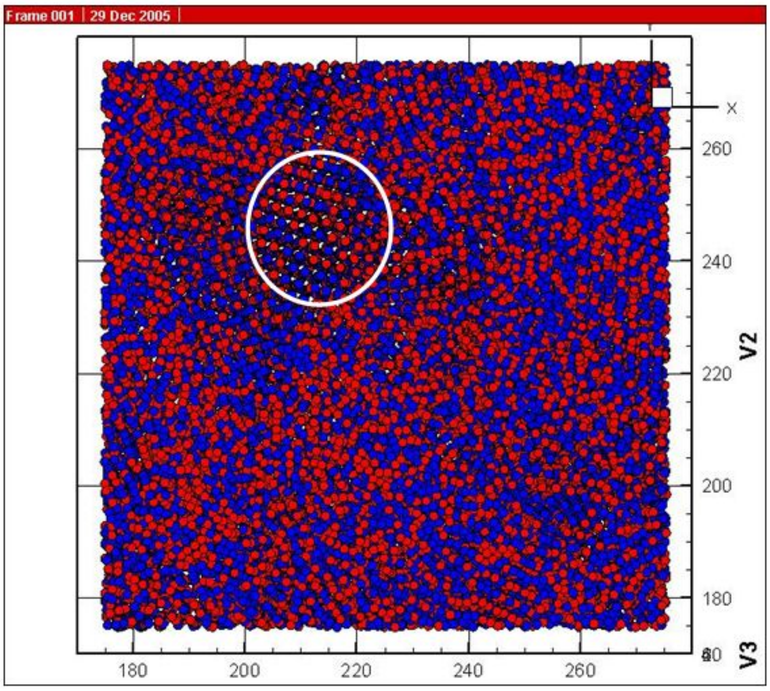

Fig. 5-10. An uncertain re-crystallized-like Zr phase whose size approach to 2 nm is identified in the matrix at the end of 14th cycle.

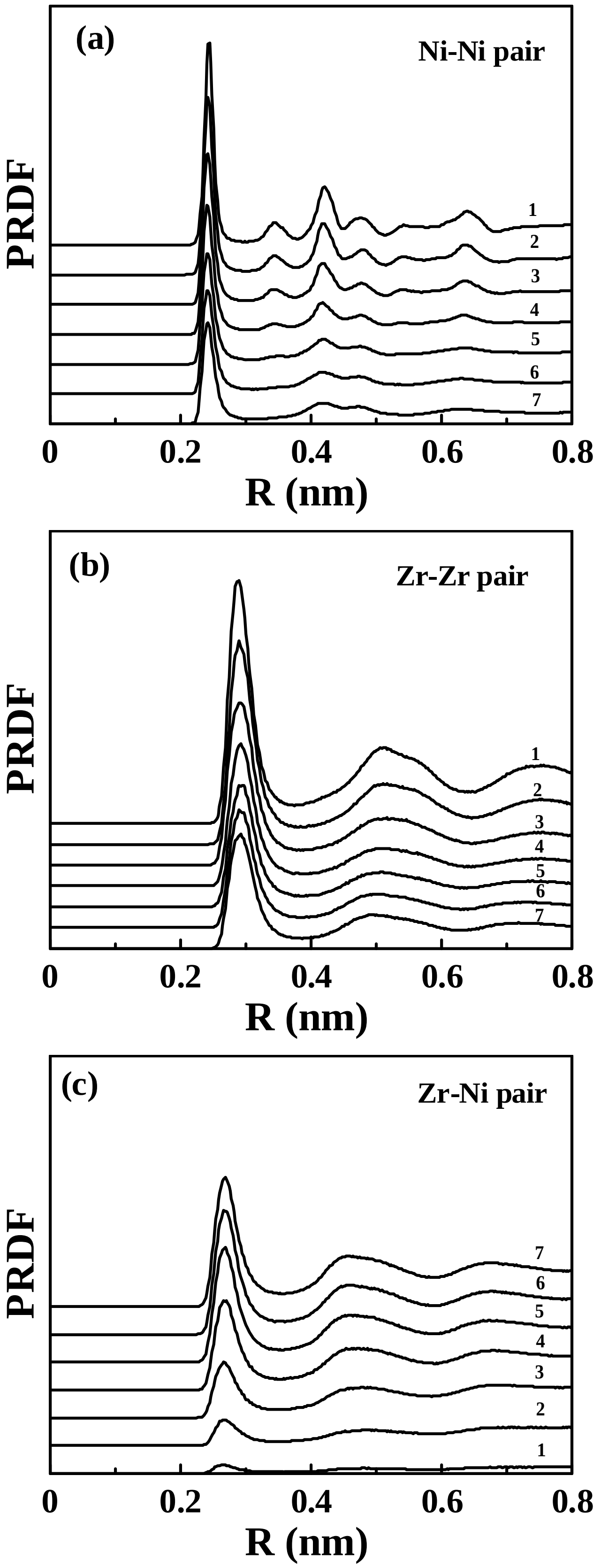

Fig. 5-11. PRDF of the Zr-Ni alloys during different ARB cycles: (a) Ni-Ni pair, (b) Zr-Zr pair, and (c) Zr-Ni pair. R is referred to the real-space atomic distance. The numbers in the figures are referred to the ARB cycle passes.

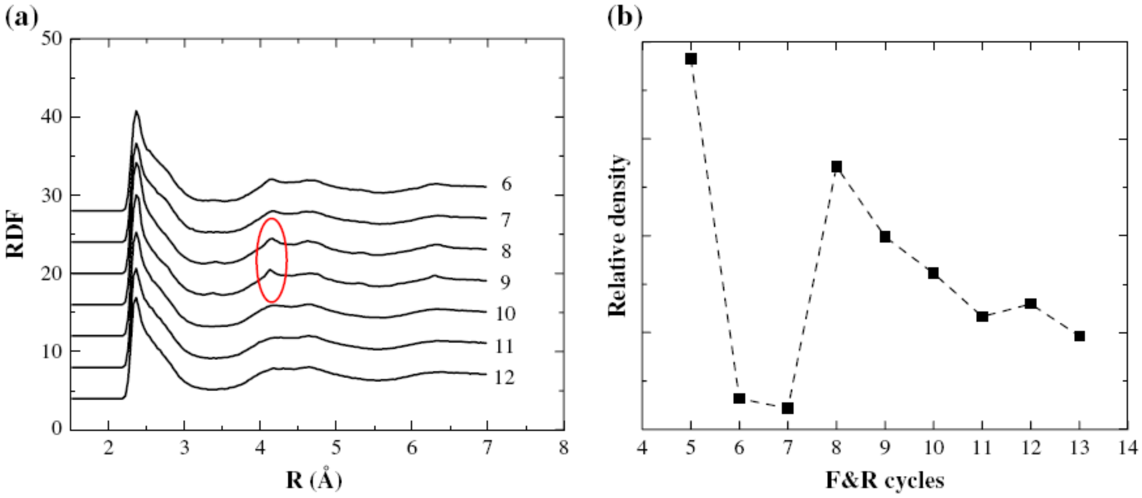

Fig. 5-12. The variation of (a) RDF and (b) volume-based number density distribution of the $Zr_{32}Ni_{68}$ alloy subjected to various F&R cycles.

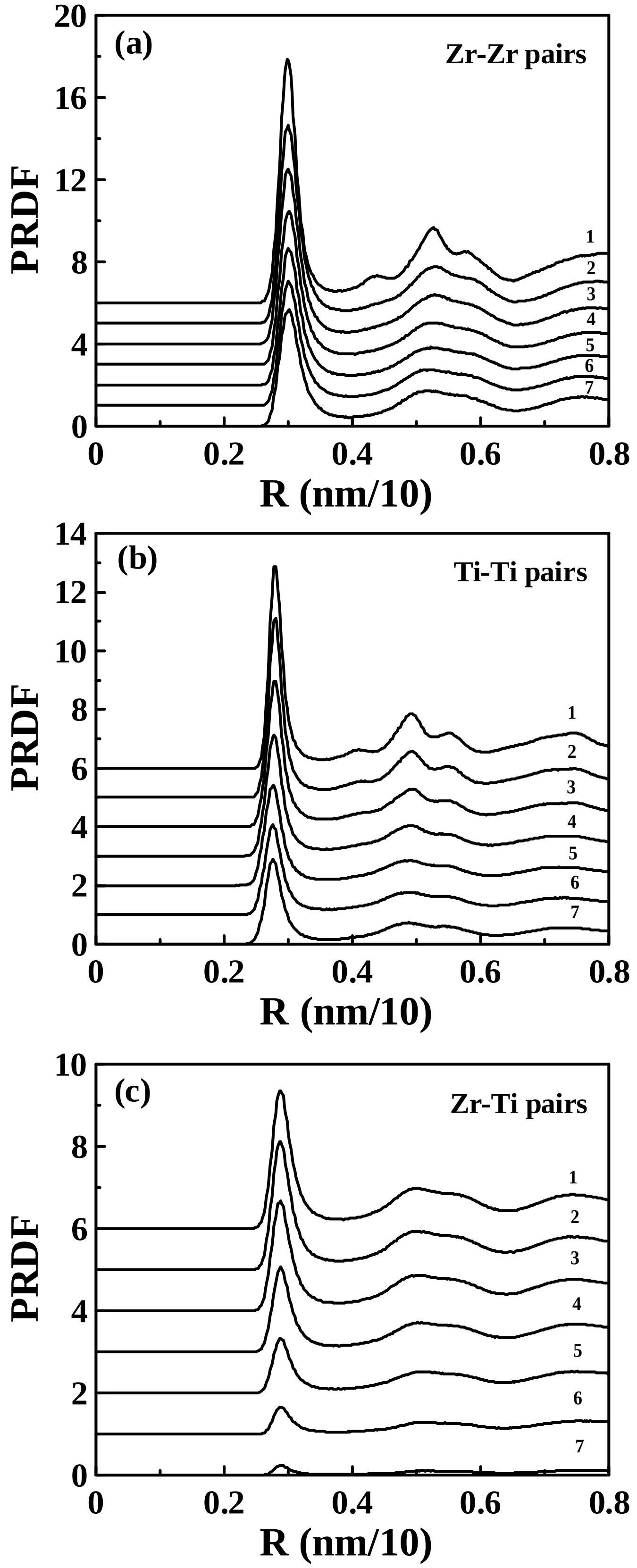

Fig. 5-13. The variations of the HA indices of the Zr-Ti alloys during different ARB cycles: (a) 1421 and 1422, (b) 1431, 1541, and 1551, and (c) 1441, 1661, and 1321.

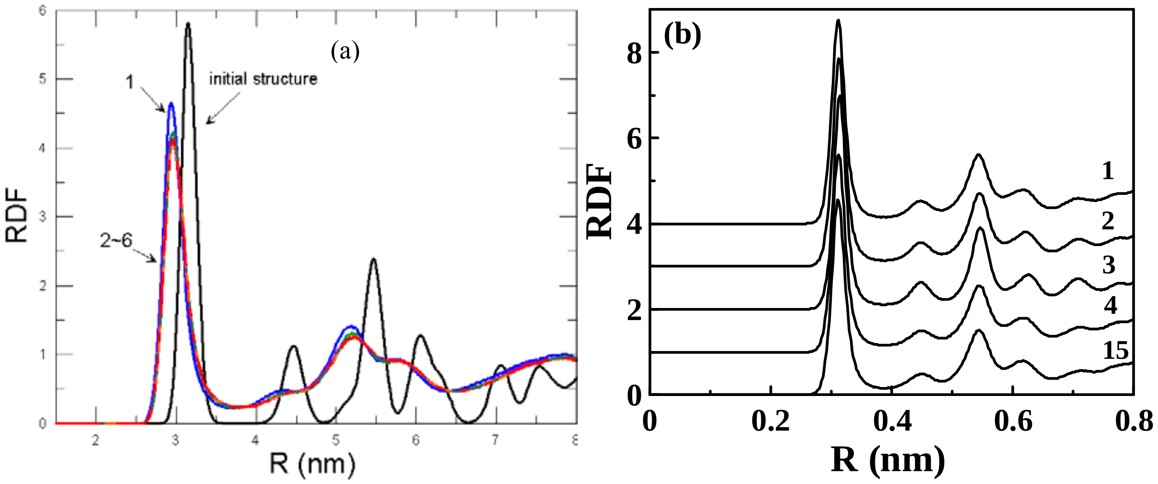

Fig. 5-14. The simulated RDF curves for the pure Zr bi-layers subjected to ARB with (a) a higher rolling speed of 0.025 nm/fs, and (b) a lower rolling speed of 0.001 nm/fs. The two layers of the front case become amorphous after 6 ARB cycles.

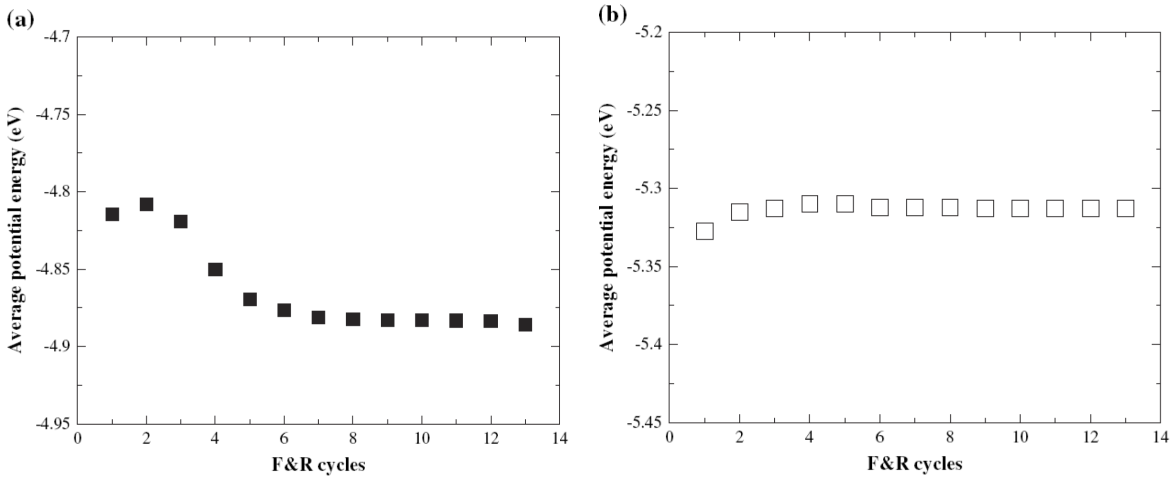

Fig. 5-15. The variation of potential energy of (a) $Zr_{32}Ni_{68}$ and (b) $Zr_{50}Ti_{50}$ alloys subjected to different F&R cycles.

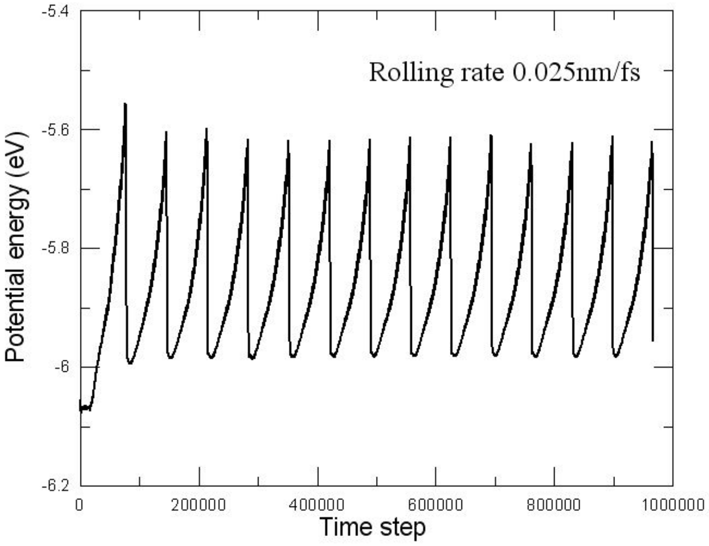

Fig. 5-16. The variation of potential energy of pure Zr alloys subjected to different F&R cycles.

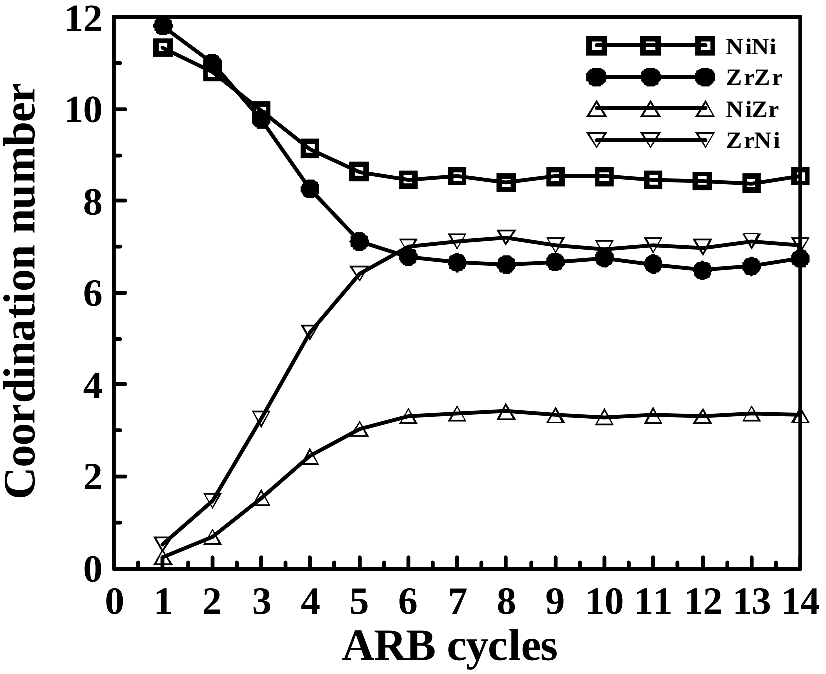

Fig. 5-17. The variation of average coordination number of the Zr-Ni alloy subjected to different ARB cycles.

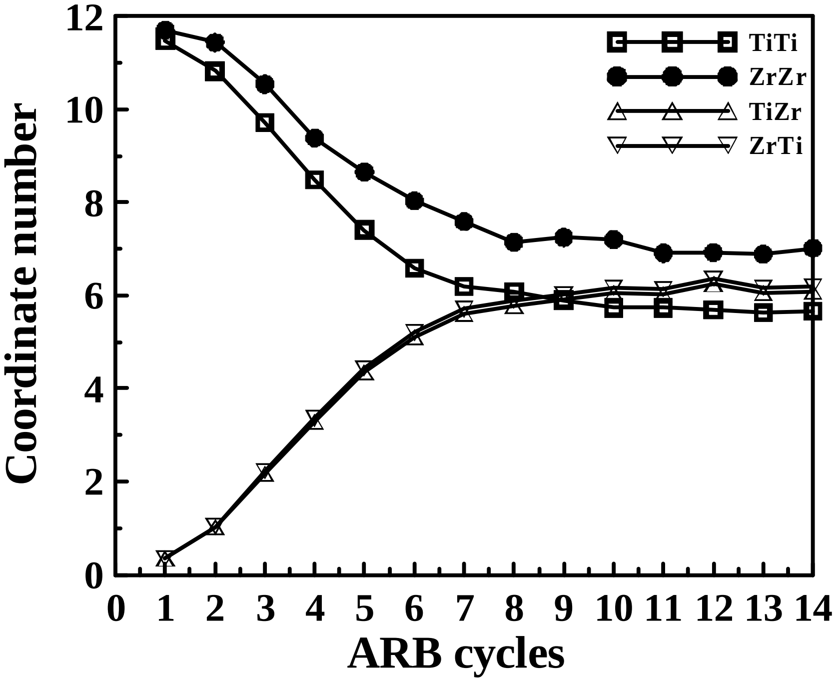

Fig. 5-18. The variation of average coordination number of the Zr-Ti alloys subjected to different ARB cycles.

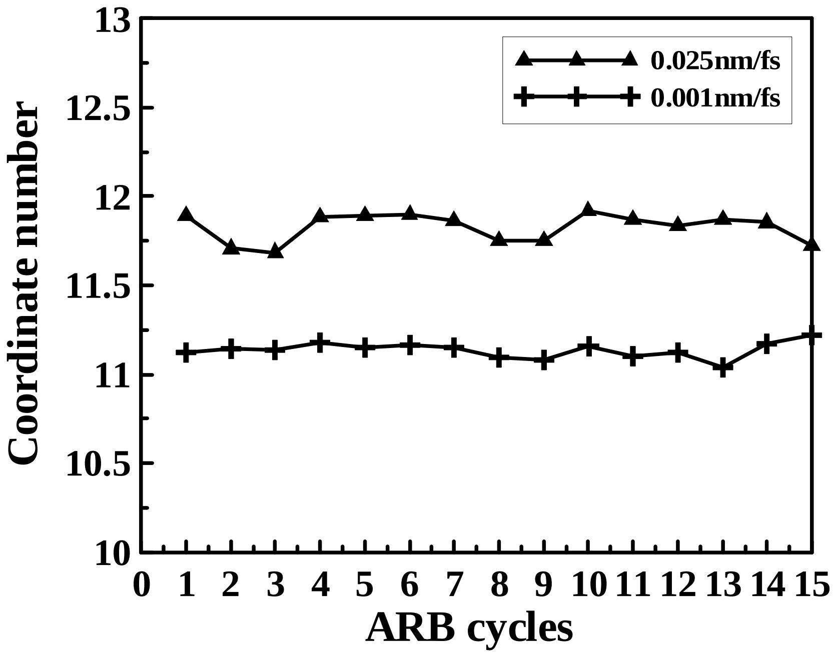

Fig. 5-19. The variation of average coordination number of the pure Zr alloys for the different rolling speed subjected to different ARB cycles.

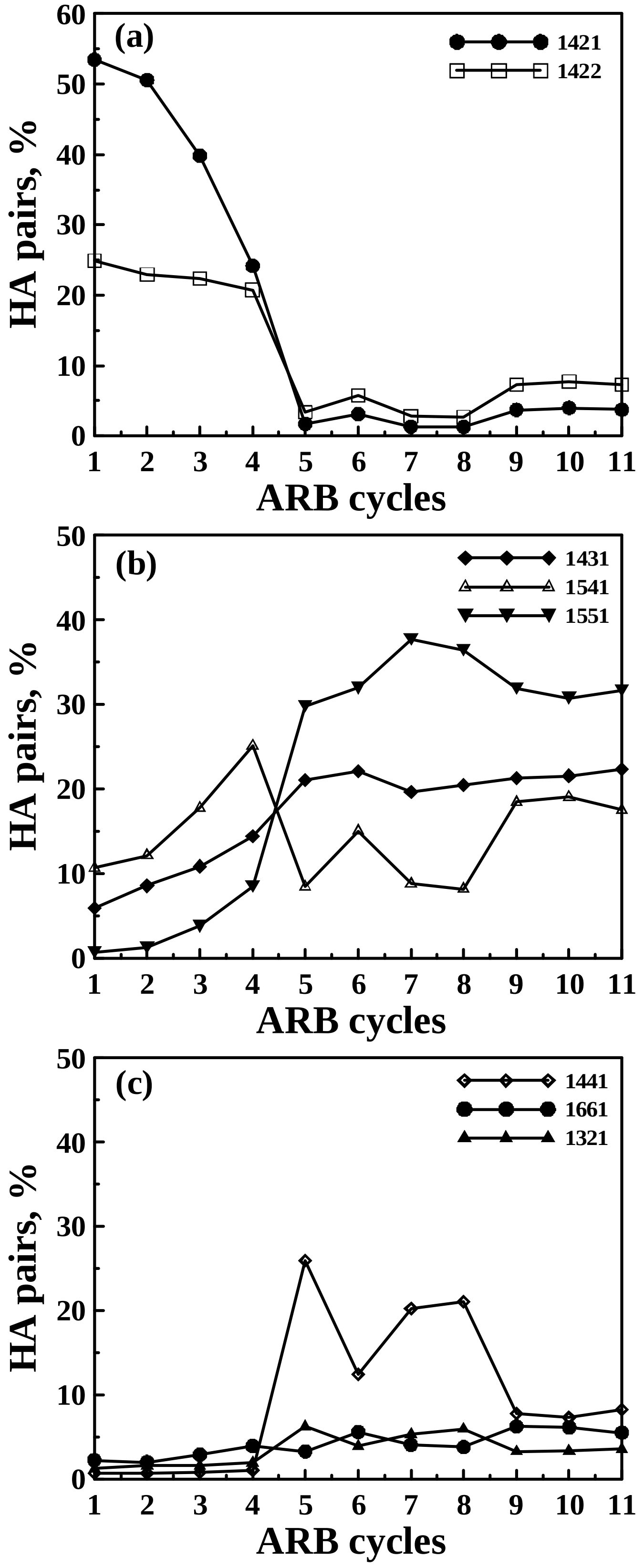

Fig. 5-20. Variations of the HA indices of the Zr-Ni alloys during different ARB cycles: (a) 1421 and 1422, (b) 1431, 1541, and 1551, and (c) 1441, 1661, and 1321.

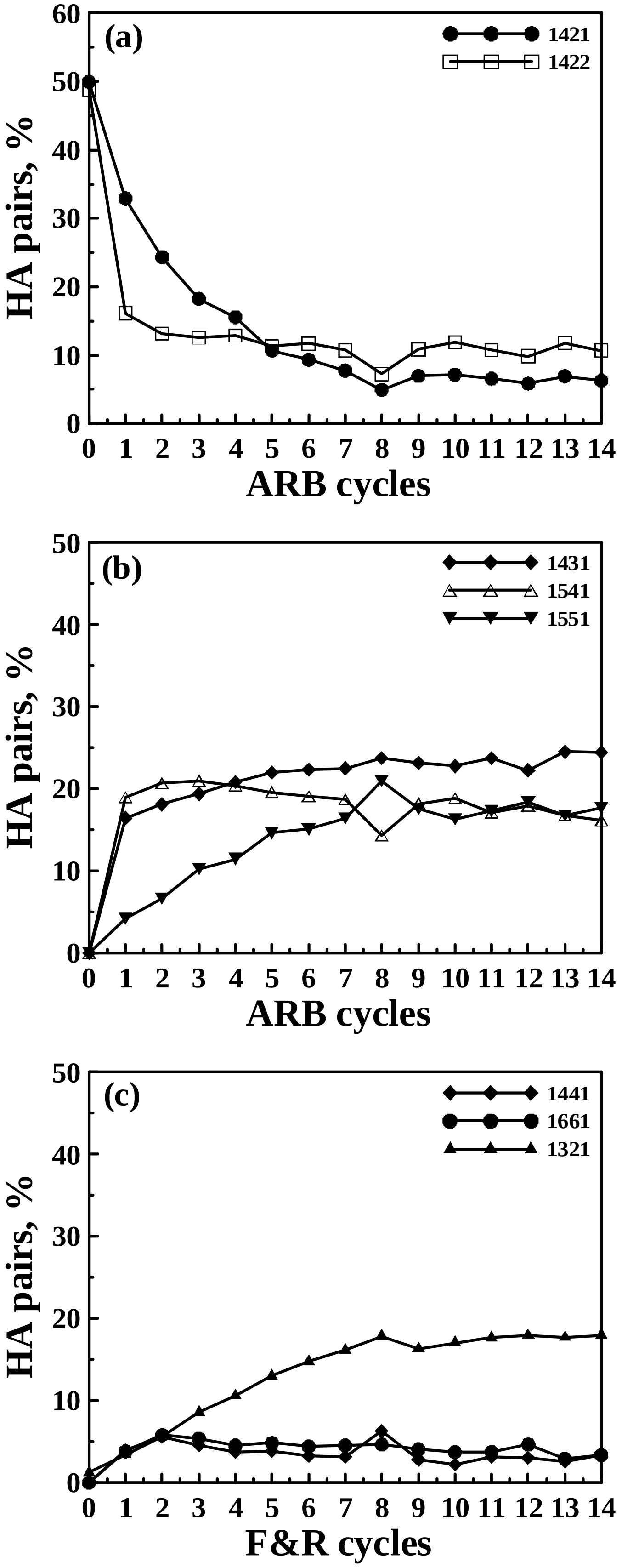

Fig. 5-21. The variations of the HA indices of the Zr-Ti alloys during different ARB cycles: (a) 1421 and 1422, (b) 1431, 1541, and 1551, and (c) 1441, 1661, and 1321.

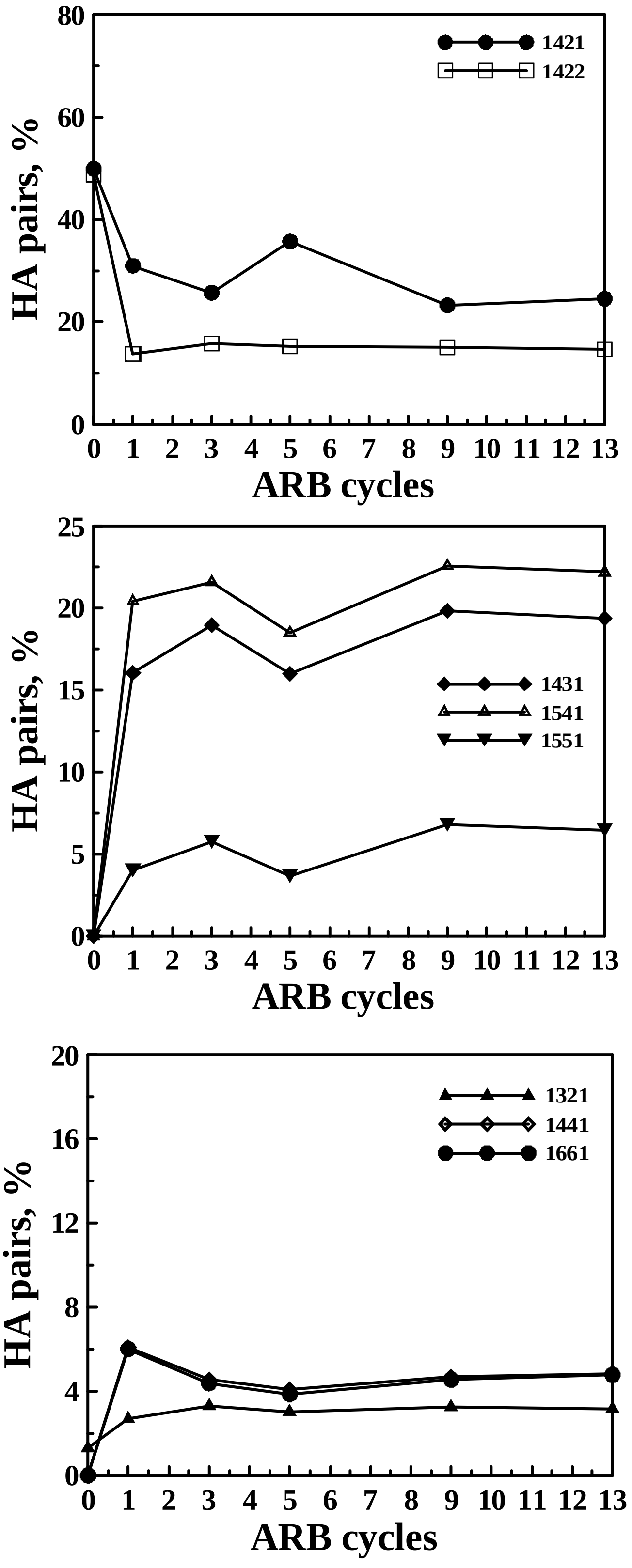

Fig. 5-22. The variations of the HA indices of the pure Zr during different ARB cycles at a higher speed of 0.025 nm/fs (strain rate of 9.25×10^{9} s^{-1}): (a) 1421 and 1422, (b) 1431, 1541, and 1551, and (c) 1441, 1661, and 1321.

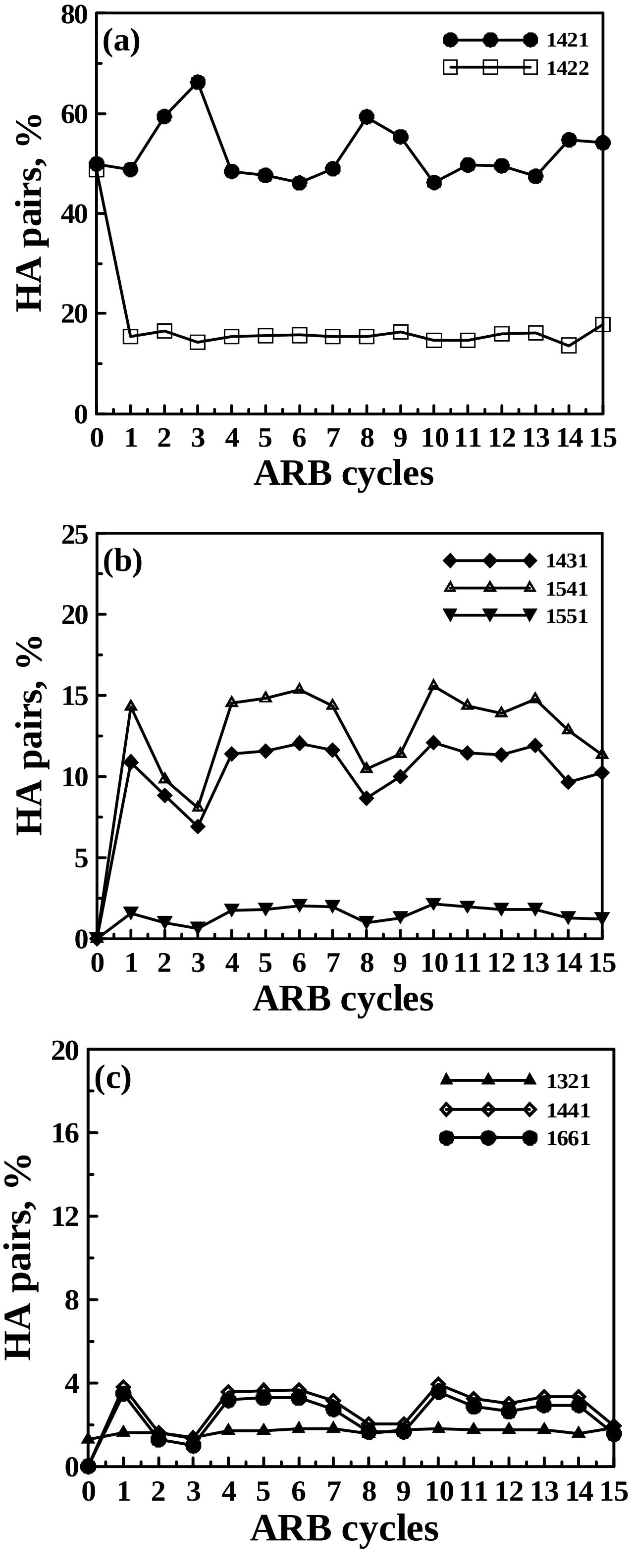

Fig. 5-23. The variations of the HA indices of the pure Zr during different ARB cycles at a lower speed of 0.001 nm/fs (strain rate of 8.35×10^{8} s^{-1}): (a) 1421 and 1422, (b) 1431, 1541, and 1551, and (c) 1441, 1661, and 1321.

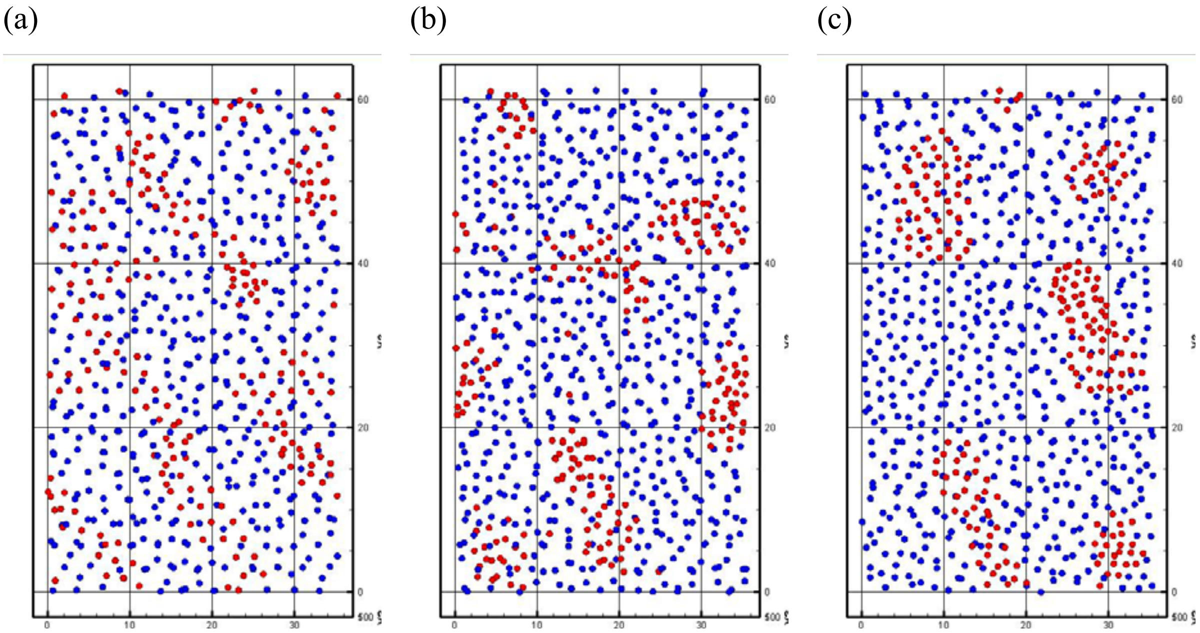

Fig. 5-24. The schemes of the projections of atomic positions annealed at (a) 300 K, (b) 413 K, and (c) 500 K. The red circle represents Cu and blue circle represents Mg.

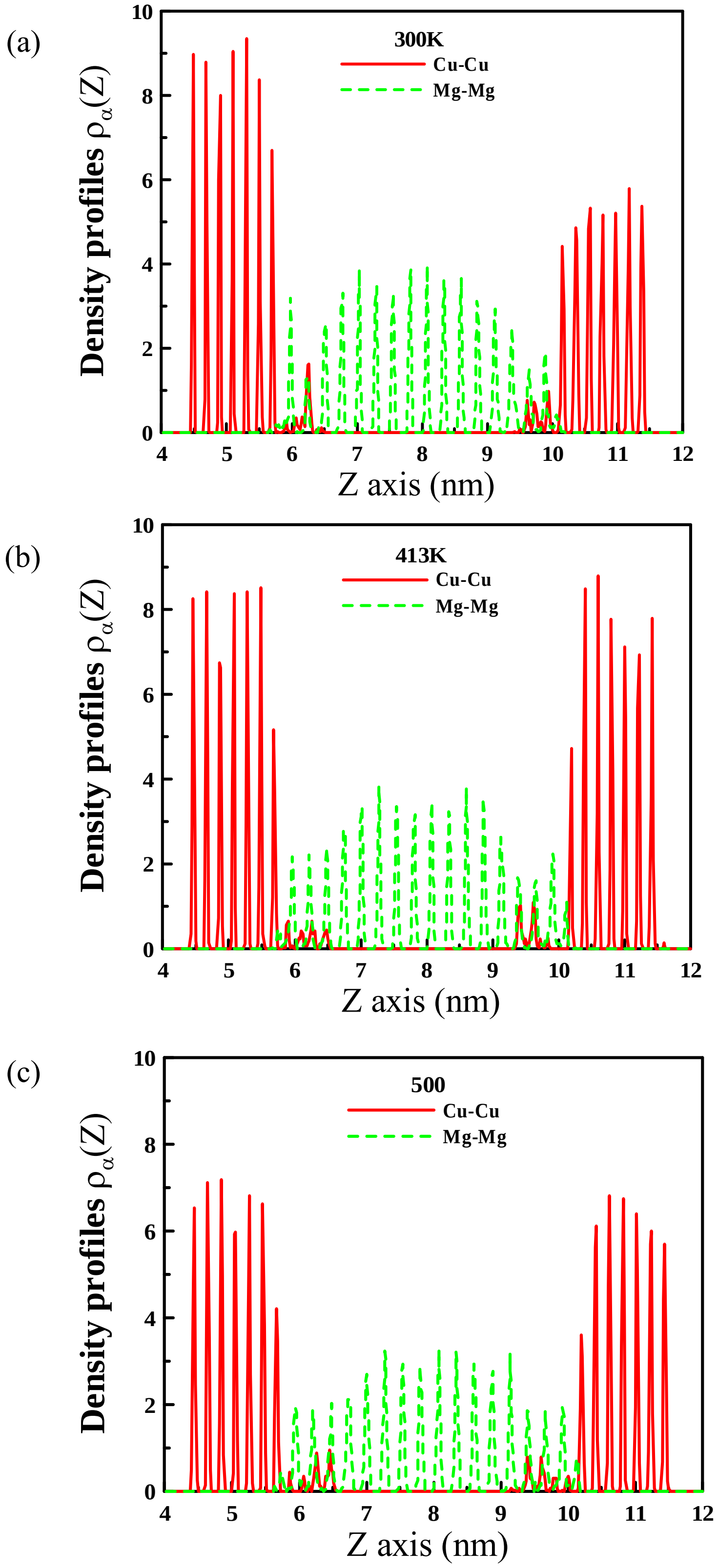

Fig. 5-25. The density profiles $\rho_{Mg}(z)$ of Mg species (green line) and $\rho_{Cu}(z)$ of Cu (red line) along the *z* axis at three temperature conditions corresponding to Fig. 5-24 (a), (b), and (c), respectively.

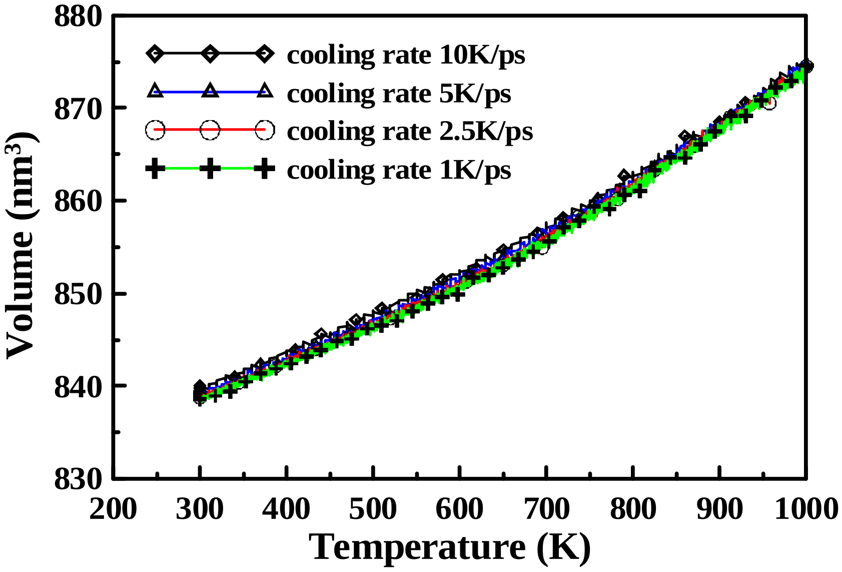

Fig. 5-26. Volume versus temperature curves for $Zr_{50}Cu_{50}$ obtained by quenching the sample model at four cooling rates from 2,000 down to 300 K.

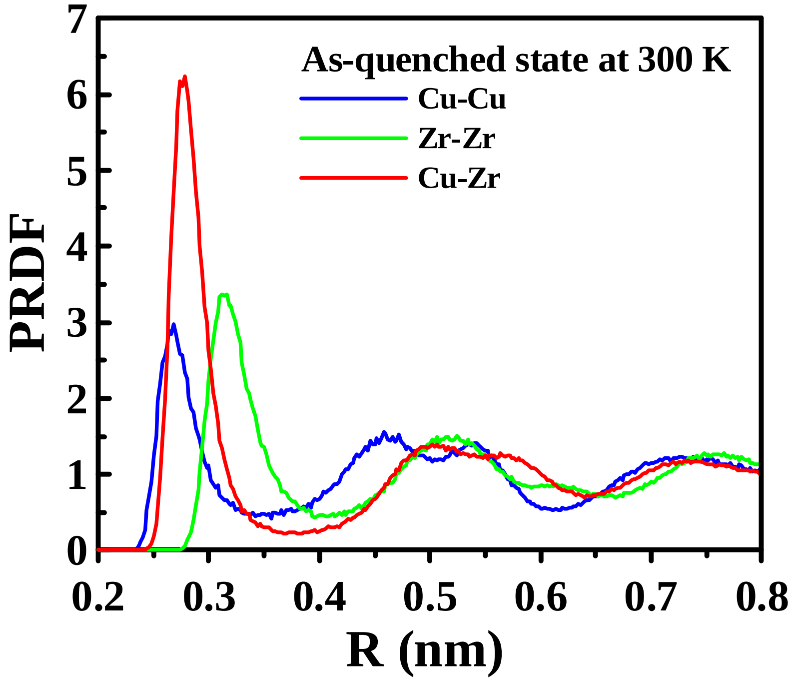

Fig. 5-27. The curves of different bond pairs of PRDF for the $Zr_{50}Cu_{50}$ amorphous alloy as quenched before fatigue loading at 300 K.

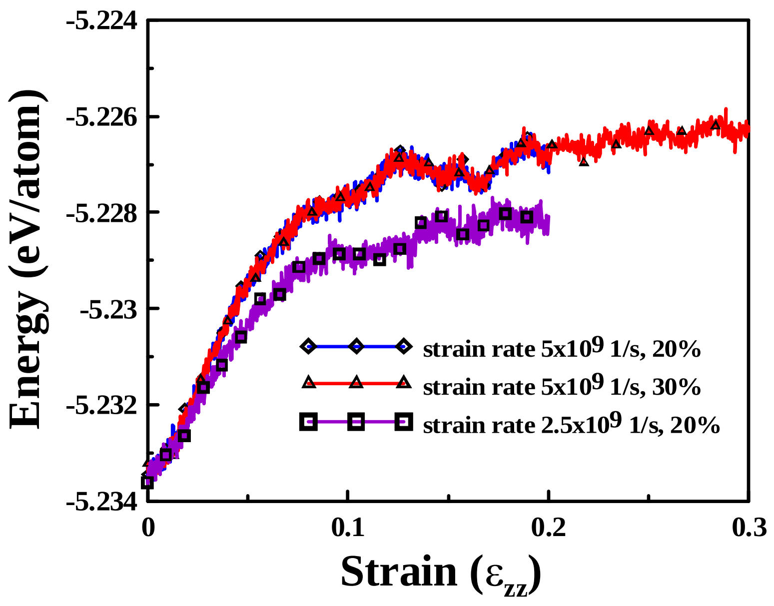

Fig. 5-28. Potential energy versus strain curves for the three different strain conditions during the monotonic deformation tests.

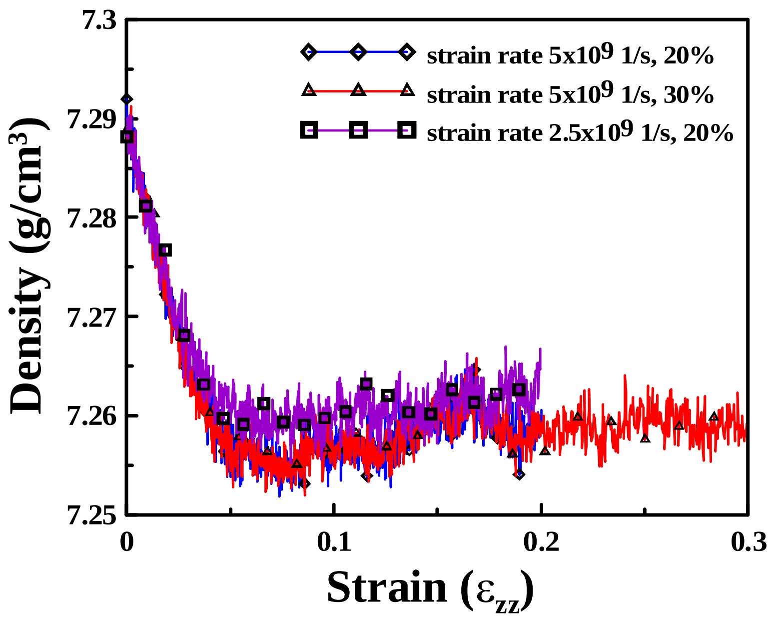

Fig. 5-29. Density versus strain curves for the three different strain conditions during the monotonic deformation tests.

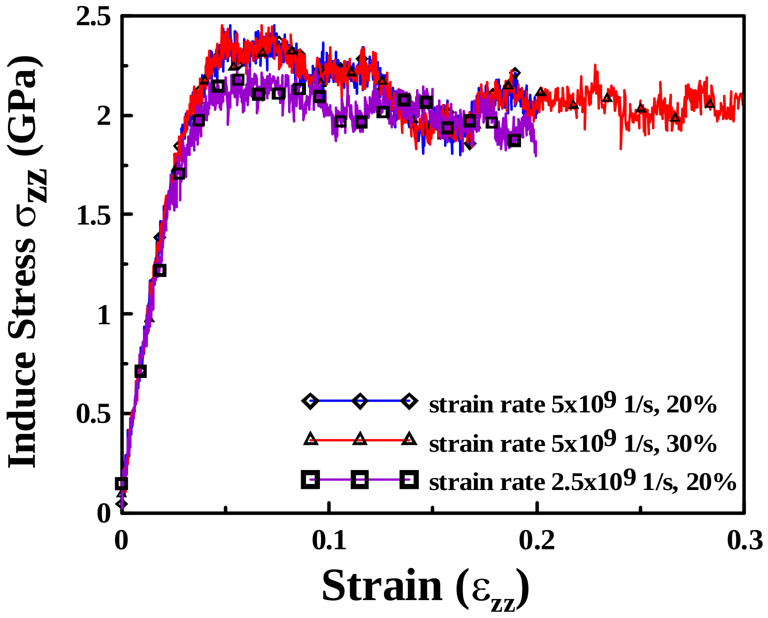

Fig. 5-30. The stress-strain curves for three strain control conditions during the monotonic test.

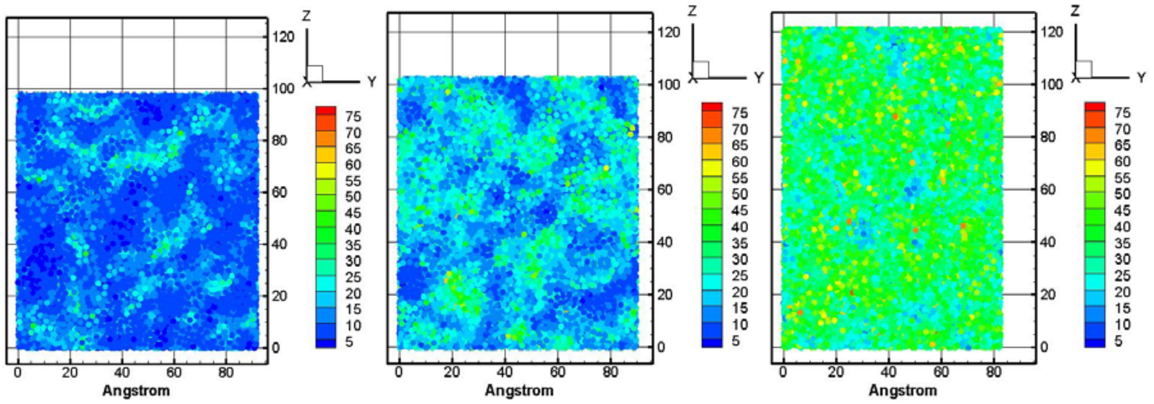

Fig. 5-31. 2D sliced plots extracting from the 3D simulated results for the local strain distribution of the monotonic strain-control at different strains (strain rate of 5 × 10^9 s^{-1}): (a) 5 %, (b) 10 %, and (c) 30 %. The color scheme represents the degree of the atomic-bond rotation, or shear strain. The numbers of the horizontal and vertical axes are in the unit of angstrom.

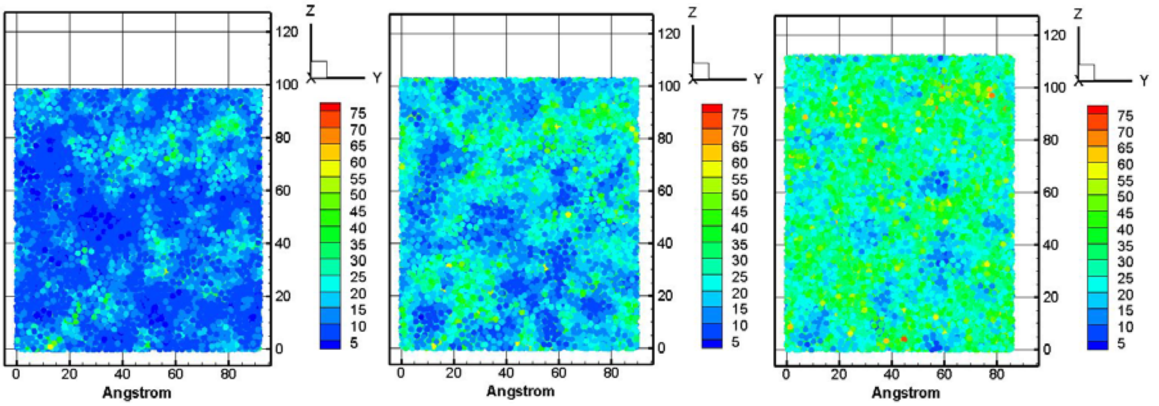

Fig. 5-32. 2D sliced plots extracting from the 3D simulated results for the local strain distribution of the monotonic strain-control at different strains (strain rate of 2.5×10^{9} s^{-1}): (a) 5 %, (b) 10 %, and (c) 20 %. The color scheme represents the degree of the atomic-bond rotation, or shear strain. The numbers of the horizontal and vertical axes are in the unit of angstrom.

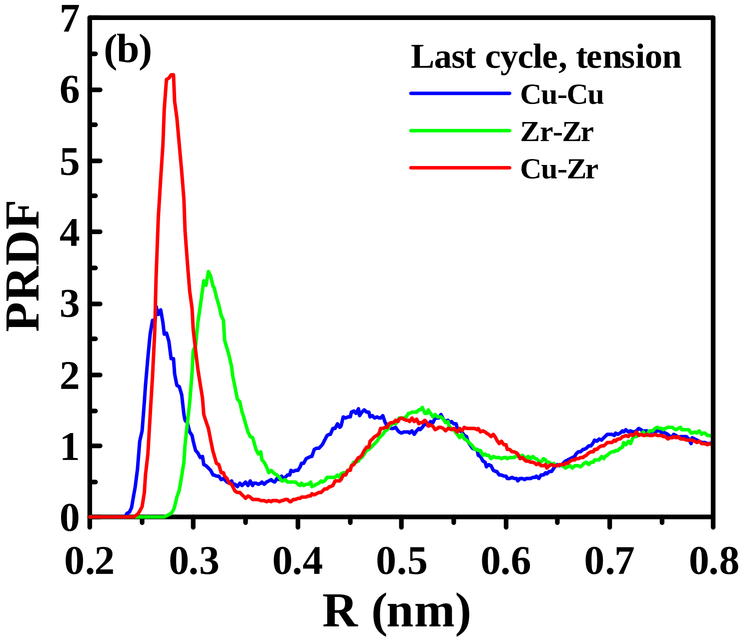

Fig. 5-33. The curves of different bond pairs of PRDF for the $Zr_{50}Cu_{50}$ amorphous alloy at 300 K after 100 cycles at $\sigma_{max} = 2$ GPa under the stress-control mode.

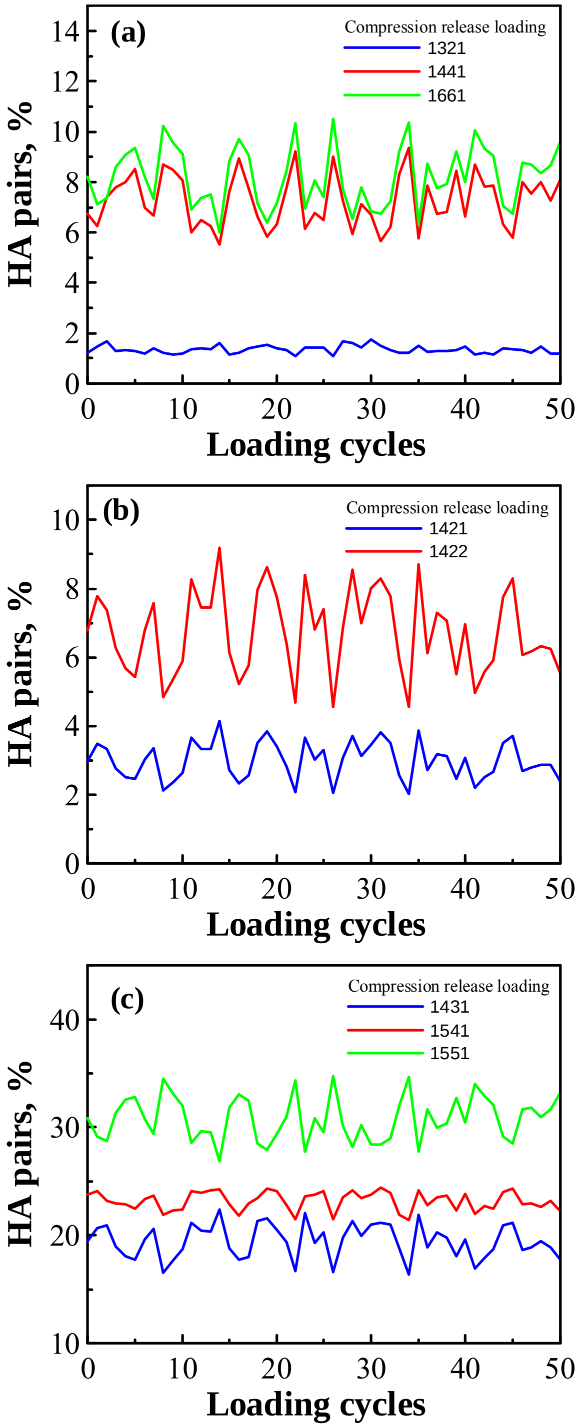

Fig. 5-34. Variations of the HA indices of the Zr-Cu amorphous alloy during different loading cycles: (a) 1421 and 1422, (b) 1431, 1541, and 1551, and (c) 1441, 1661, and 1321 under compression-compression stress-control at σ_{max} = 1 GPa.

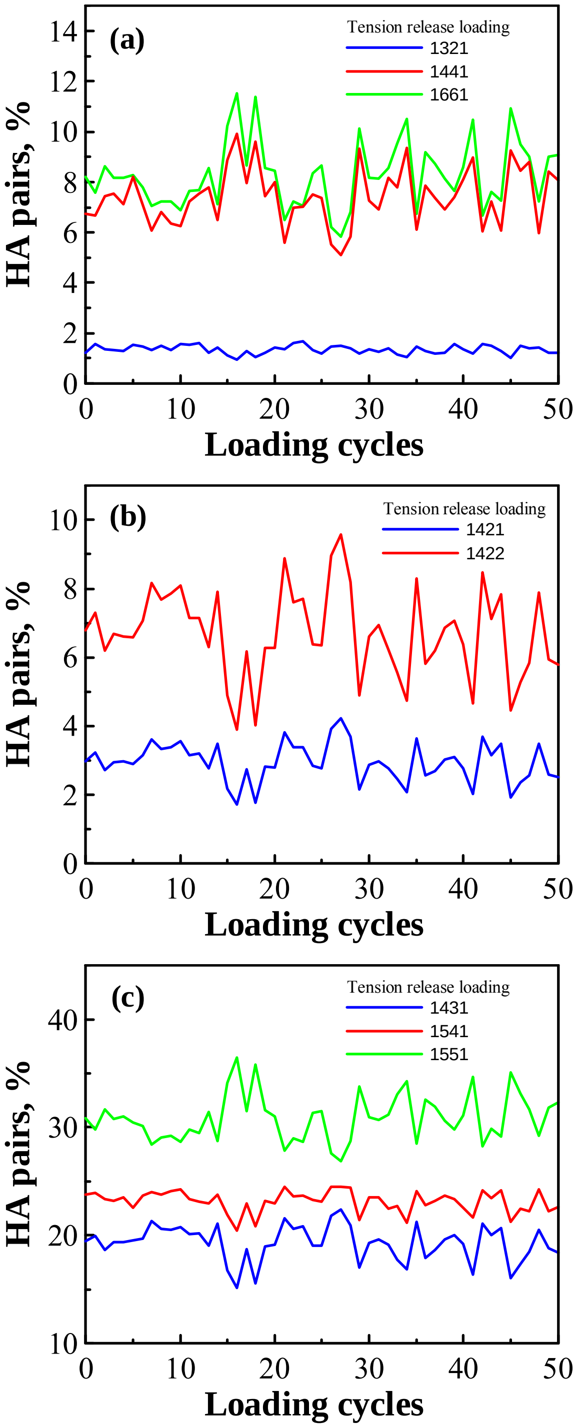

Fig. 5-35. Variations of the HA indices of the Zr-Cu amorphous alloy during different loading cycles: (a) 1421 and 1422, (b) 1431, 1541, and 1551, and (c) 1441, 1661, and 1321 under tension-tension stress-control at σ_{max} = 1 GPa.

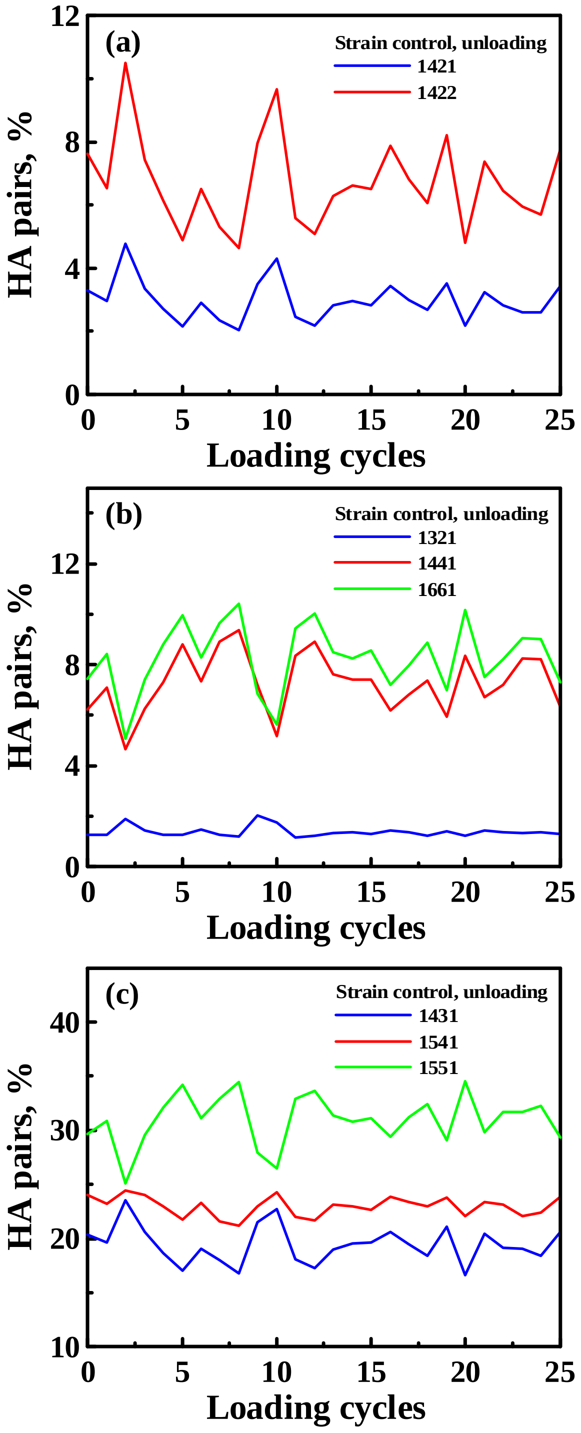

Fig. 5-36. Variations of the HA indices of the Zr-Cu amorphous alloy as a function of loading cycles: (a) 1421 and 1422, (b) 1321, 1441, and 1661, and (c) 1431, 1541, and 1551 under the cyclic strain-control mode at ε_{max} = 10%.

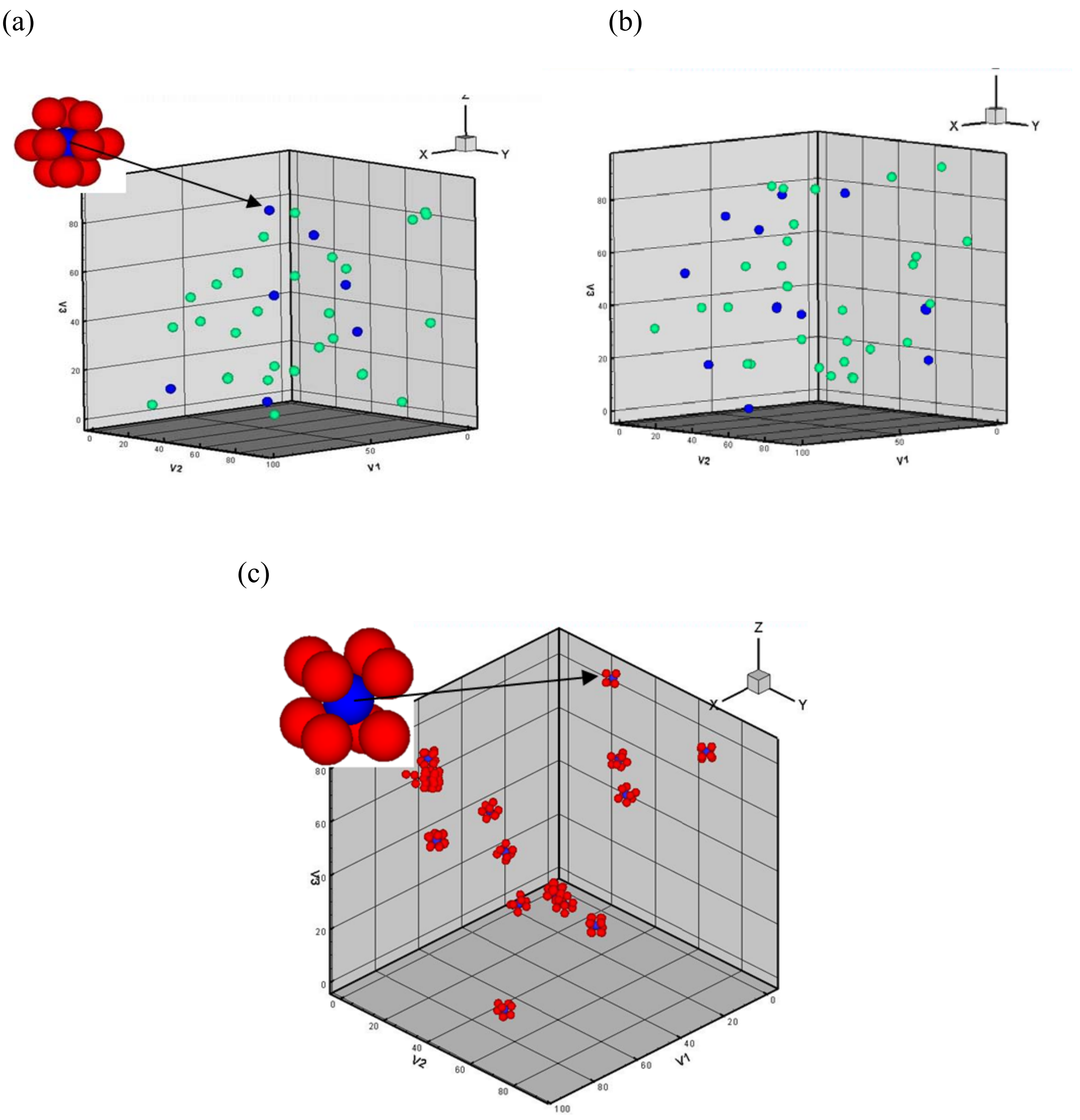

Fig. 5-37. The scheme of the superimposed projections of close-packed atoms at (a) compression-compression, (b) tension-tension at σ_{max} = 1 GPa, respectively. The blue circle represents FCC atoms and green circle represents HCP atoms. The superimposed projections of the B2 atoms during the stress-control tensile mode at σ_{max} = 2 GPa are shown in (c). The blue circles represent the central atoms, and red circles represent the surrounding atoms of a B2 structure. Note that this scheme represents the superimposition of all occurrences of those atoms that have occurred over the whole 50 cycles.

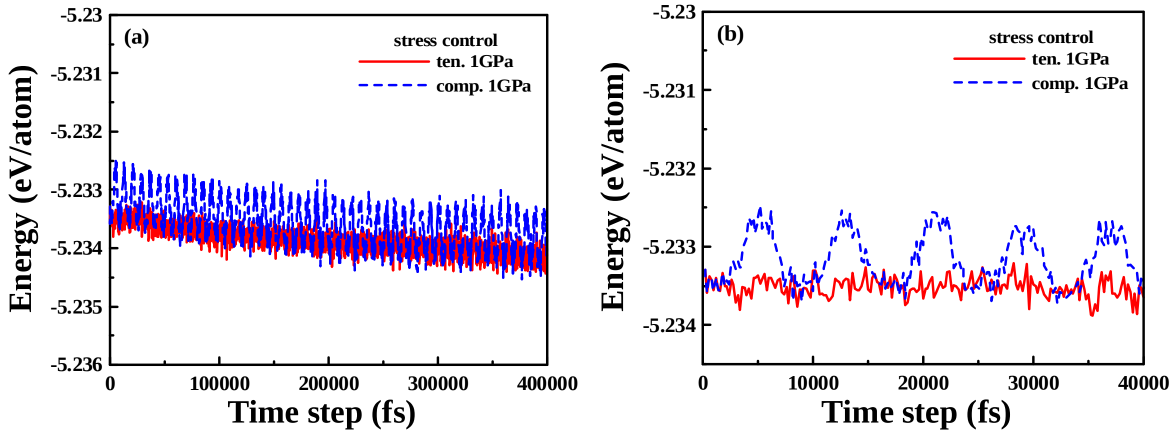

Fig. 5-38. The Comparison of potential energies between tension and compression of cyclic loading under stress-control at σ_{max} = 1 GPa.

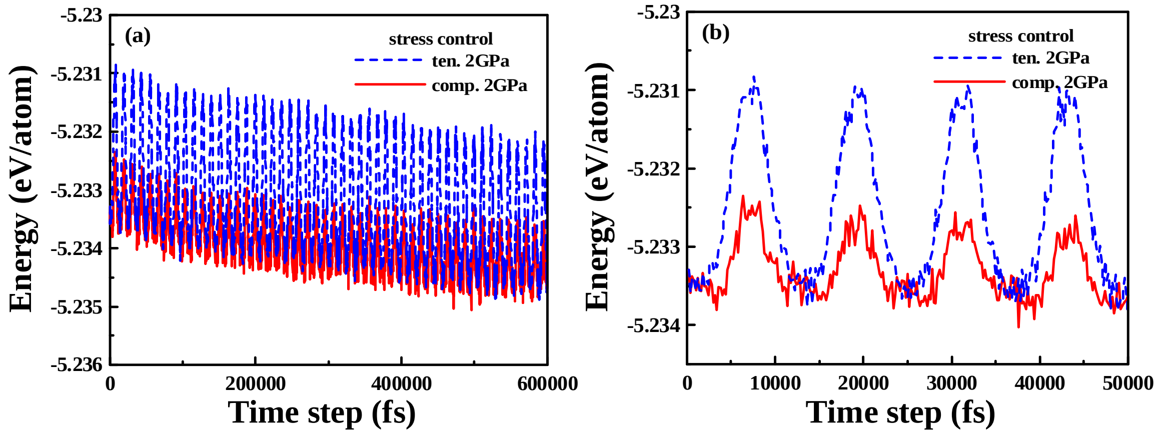

Fig. 5-39. The Comparison of potential energies between tension and compression of cyclic loading under stress-control at σ_{max} = 2 GPa.

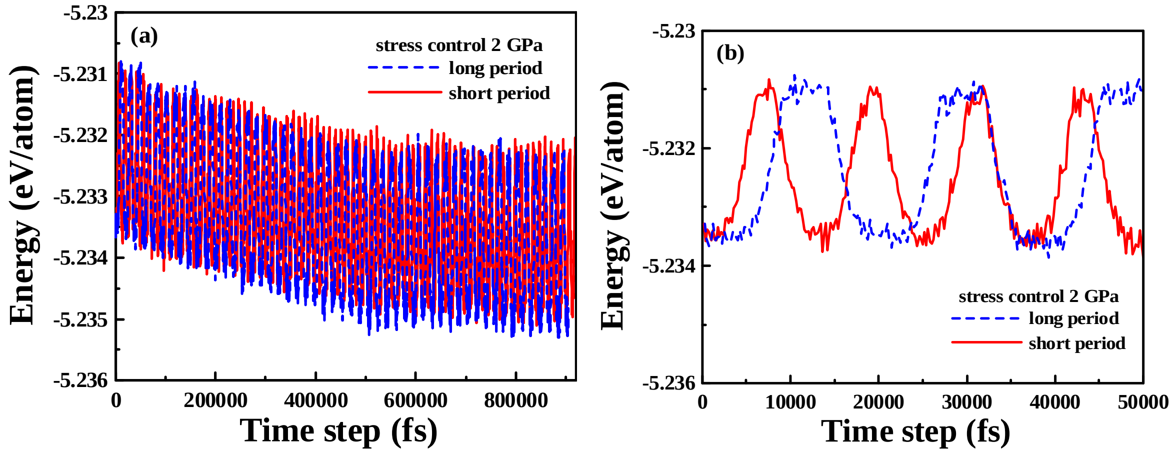

Fig. 5-40. The Comparison of potential energies between long and short periods for the cyclic stress-control at σ_{max} = 2 GPa. The equilibrium time for long period is twice as much as short one.

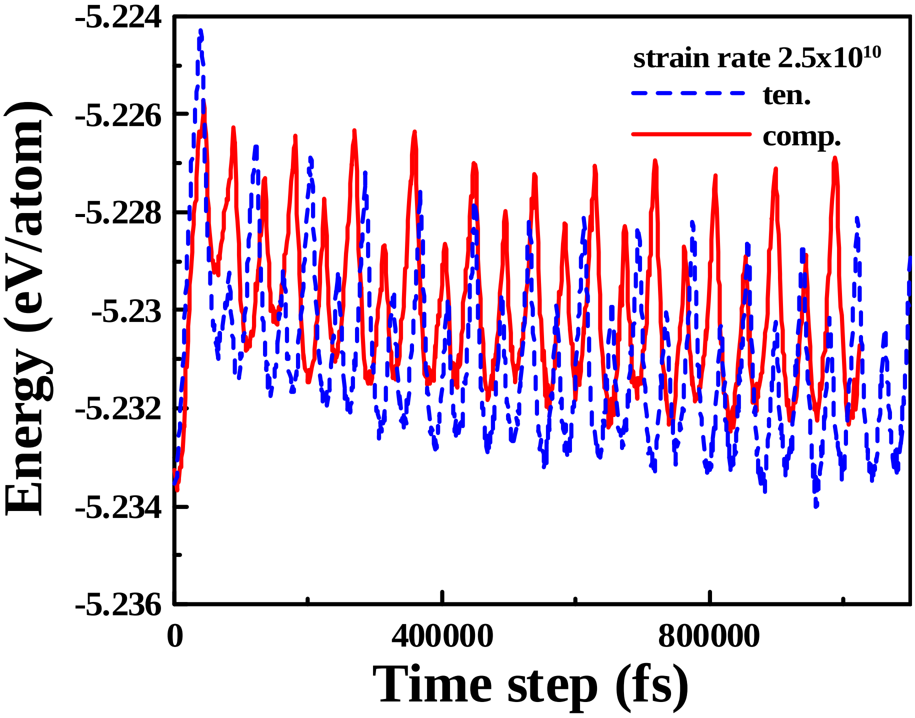

Fig. 5-41. The Comparison of potential energies between tension and compression of cyclic loading under strain-control at strain rate of 2.5 × 10^{10} s^{-1}.

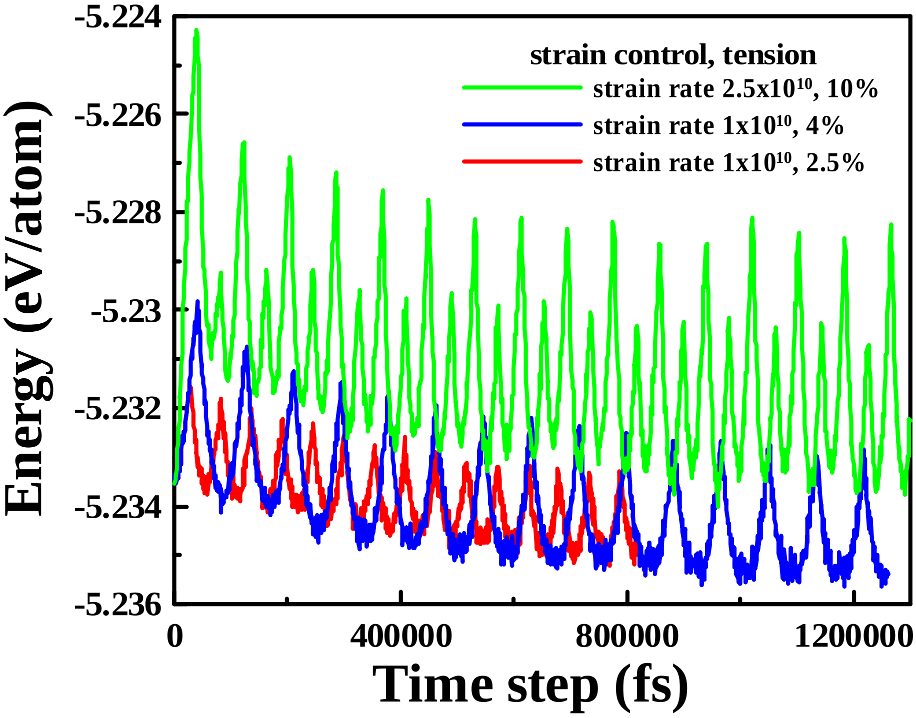

Fig. 5-42. The comparison of potential energies of cyclic loading under strain-control among three different strain ranges.

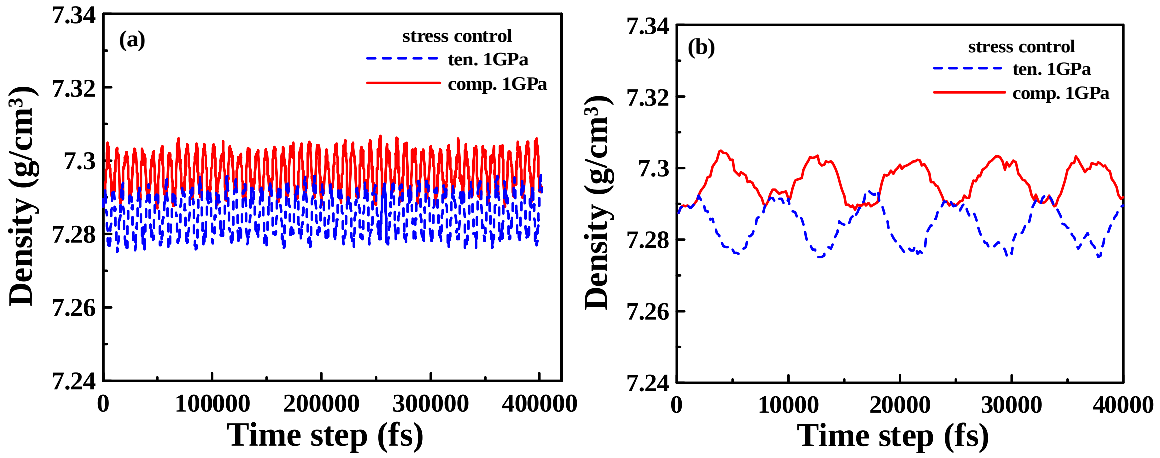

Fig. 5-43. Variations of the density as a function of the fatigue-time step at different loading modes for stress-control loading at $\sigma_{max} = 1$ GPa. The blue dotted line presents the density variation under tension and the red solid line presents the variation of density variation under compression.

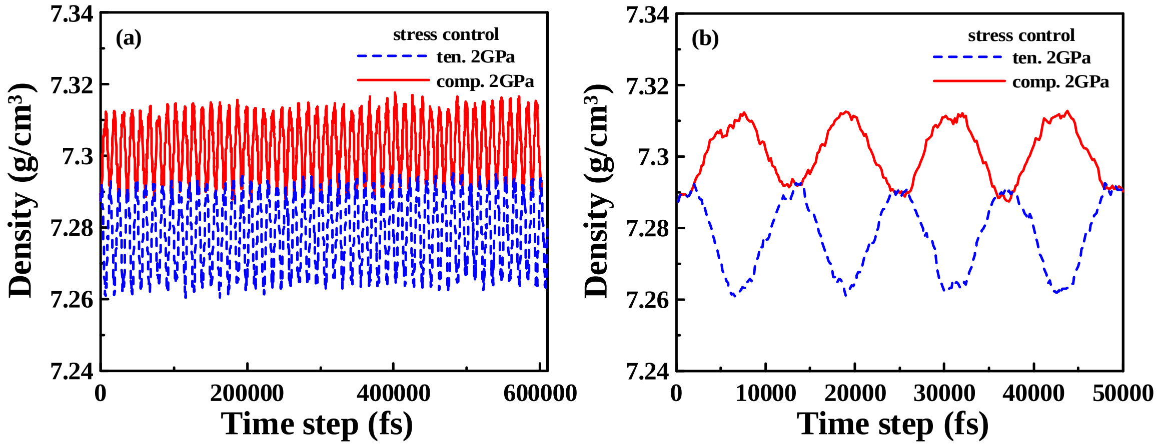

Fig. 5-44. Variations of the density as a function of the fatigue-time step at different loading modes for stress-control loading at $\sigma_{max} = 2$ GPa. The blue dotted line presents the density variation under tension and the red solid line presents the variation of density variation under compression.

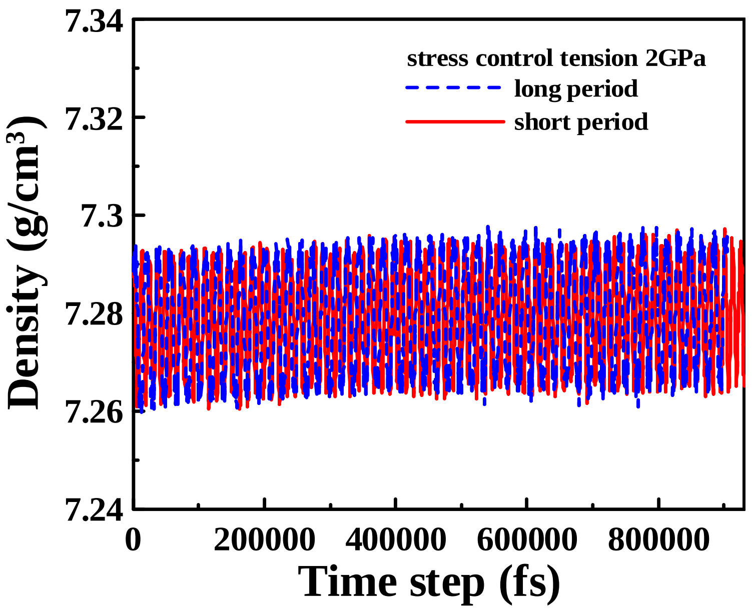

Fig. 5-45. Variations of the density as a function of the fatigue-time step at different loading periods for stress-control loading at $\sigma_{max} = 2$ GPa. The blue dotted line presents the density variation for long period and the red solid line presents the variation of density variation for short period.

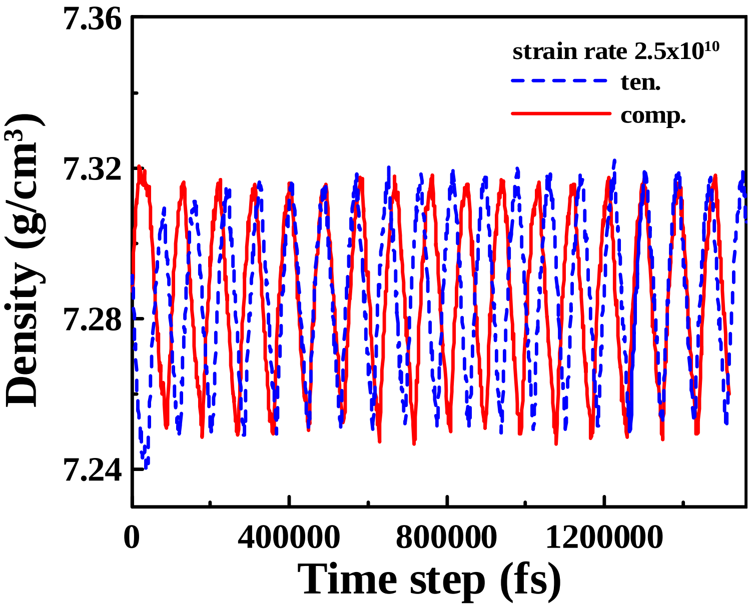

Fig. 5-46. Variations of the density as a function of the fatigue-time step at different loading modes for strain-control loading at $\varepsilon_{max} = 10$ % and strain rate at 2.5×10^{10} s^{-1}. The blue dotted line presents the density variation under tension and the red solid line presents the variation of density variation under compression.

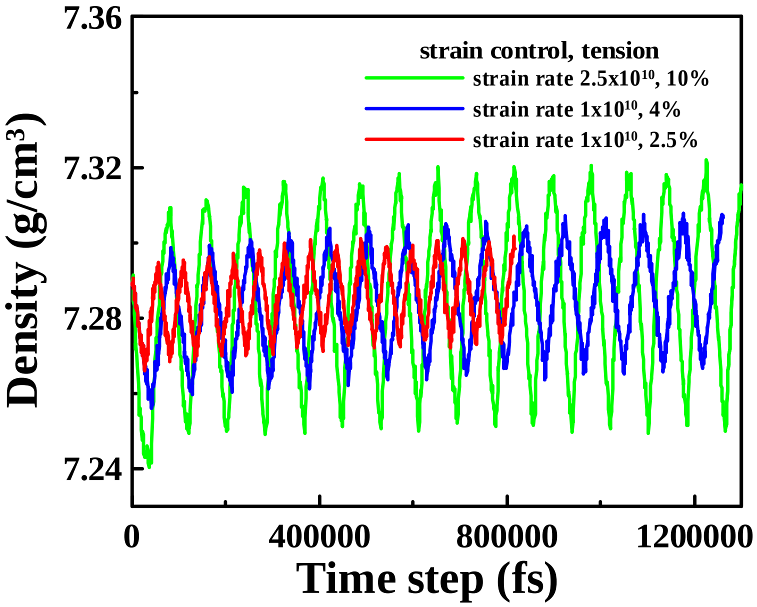

Fig. 5-47. Variations of the density as a function of the fatigue-time step at different three loading conditions under strain-control loading.

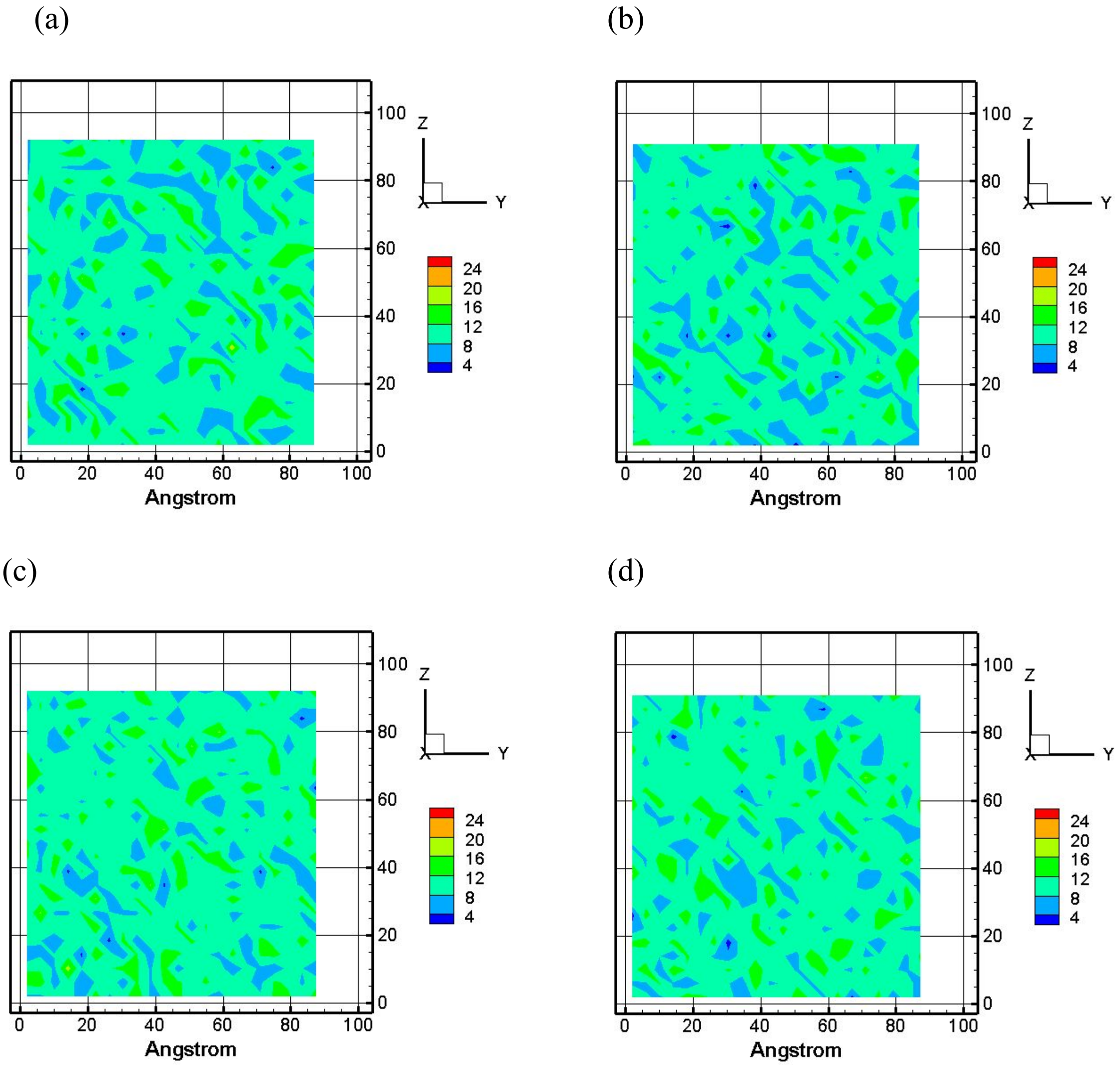

Fig. 5-48. Density profile of the strain-control fatigue at different cycles: (a) cycle twelve, loading, (b) cycle twelve, unloading, (c) cycle twenty-five, loading, and (d) cycle twenty-five, unloading. The blue color represents the lower density (as the regions with the free volume). The numbers of the horizontal and vertical axes are in the unit of angstrom.

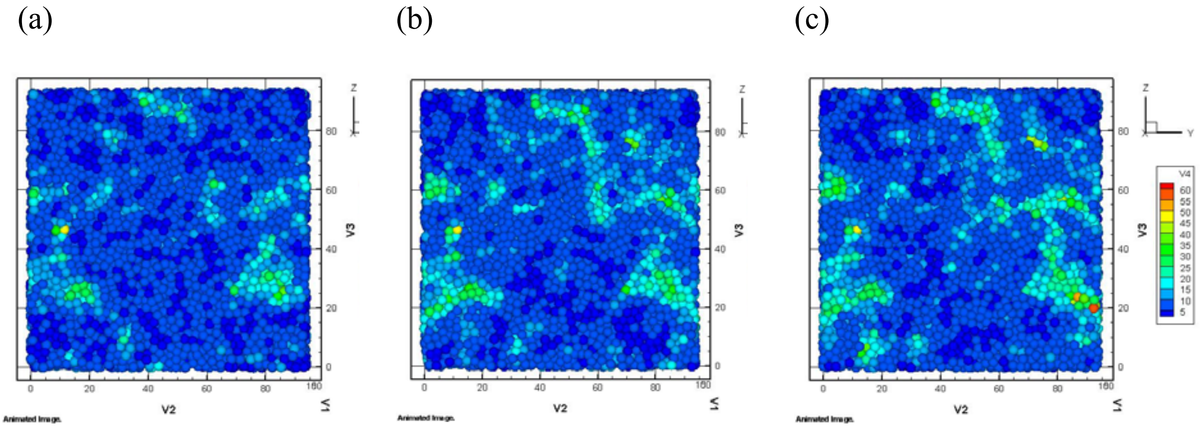

Fig. 5-49. 2D sliced plots extracting from the 3D simulated results for the local strain distribution of tension mode of the stress-control fatigue at different cycles at $\sigma_{max} = 1$ GPa: (a) Cycle ten, (b) Cycle thirty, and (c) Cycle fifty. The color scheme represents the degree of atomic bond rotation, or shear strain.

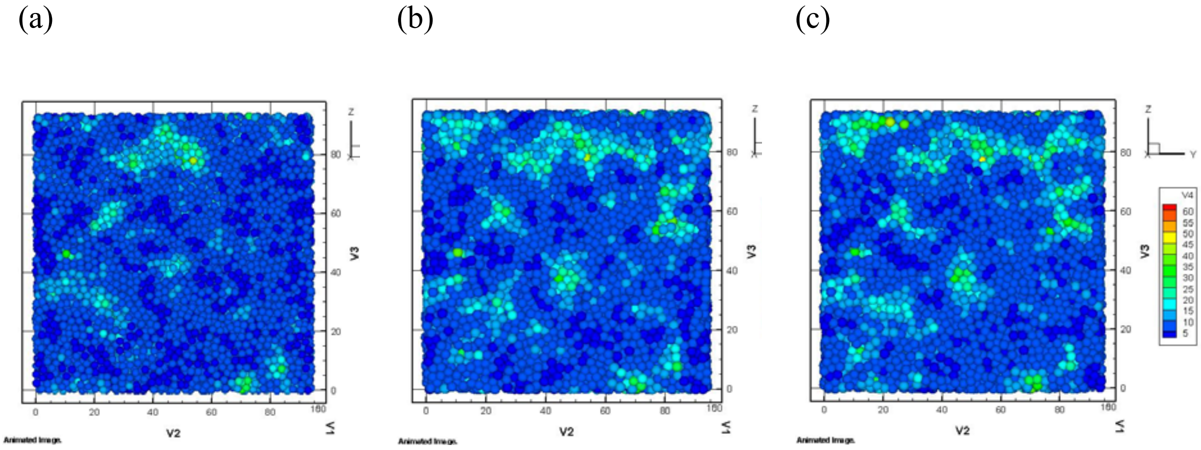

Fig. 5-50. 2D sliced plots extracting from the 3D simulated results for the local strain distribution of compression mode of the stress-control fatigue at different cycles at $\sigma_{max} = 1$ GPa: (a) Cycle ten, (b) Cycle thirty, and (c) Cycle fifty. The color scheme represents the degree of atomic bond rotation, or shear strain.

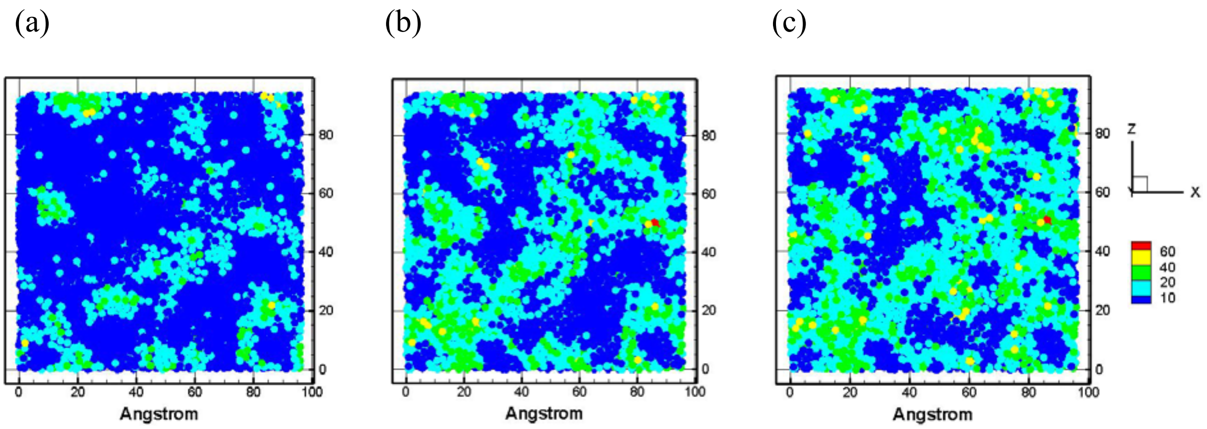

Fig. 5-51. 2D sliced plots extracting from the 3D simulated results for the local strain distribution of the stress-control fatigue at different cycles at $\sigma_{max} = 2$ GPa: (a) cycle ten, (b) cycle fifty, and (c) cycle one hundred. The color scheme represents the degree of the atomic-bond rotation, or shear strain. The numbers of the horizontal and vertical axes are in the unit of angstrom.

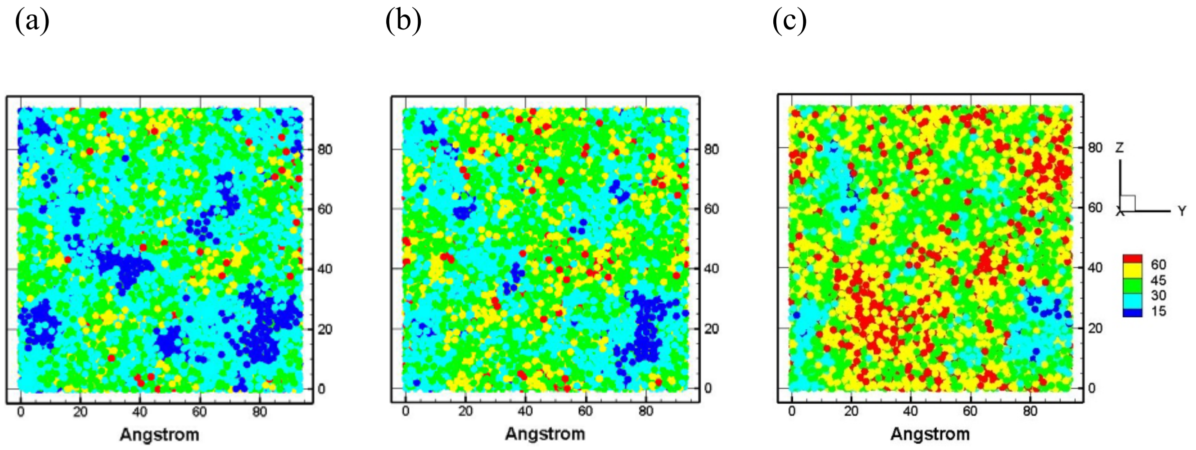

Fig. 5-52. 2D sliced plots extracting from the 3D simulated results for the local strain distribution of the strain-control fatigue at different cycles: (a) cycle five, (b) cycle ten, and (c) cycle twenty-five. The color scheme represents the degree of atomic-bond rotation, or shear strain. The numbers of the horizontal and vertical axes are in the unit of angstrom.

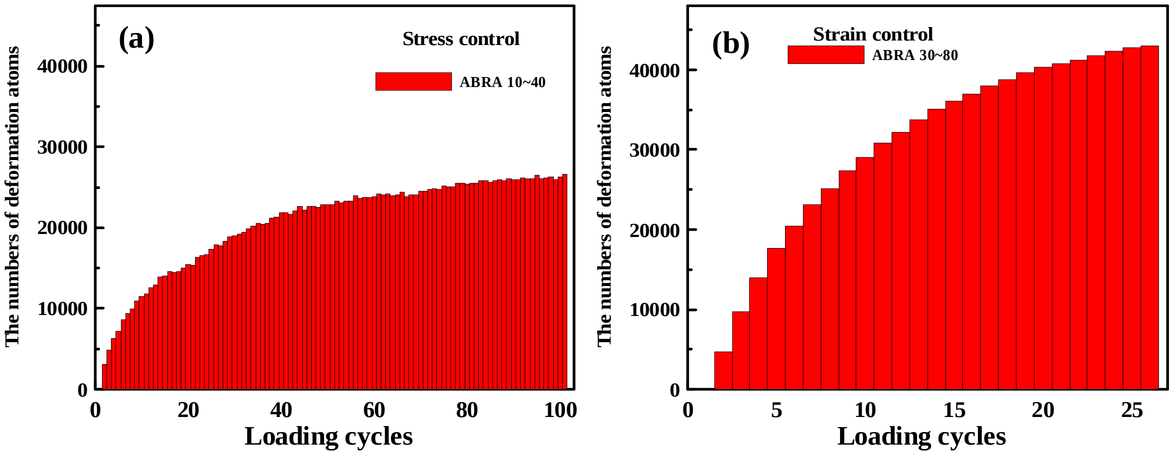

Fig. 5-53. The accumulation numbers of deformation atoms as a function of loading cycles: (a) the stress-control mode in the Fig. 5-50 and (b) the strain-control mode in the Fig. 5-51, respectively. The change of growth rate of plastic flows implies a resistance against the sustained development of STZ groups occurs when accumulation deformations reach a specific amount during the cyclic loading.

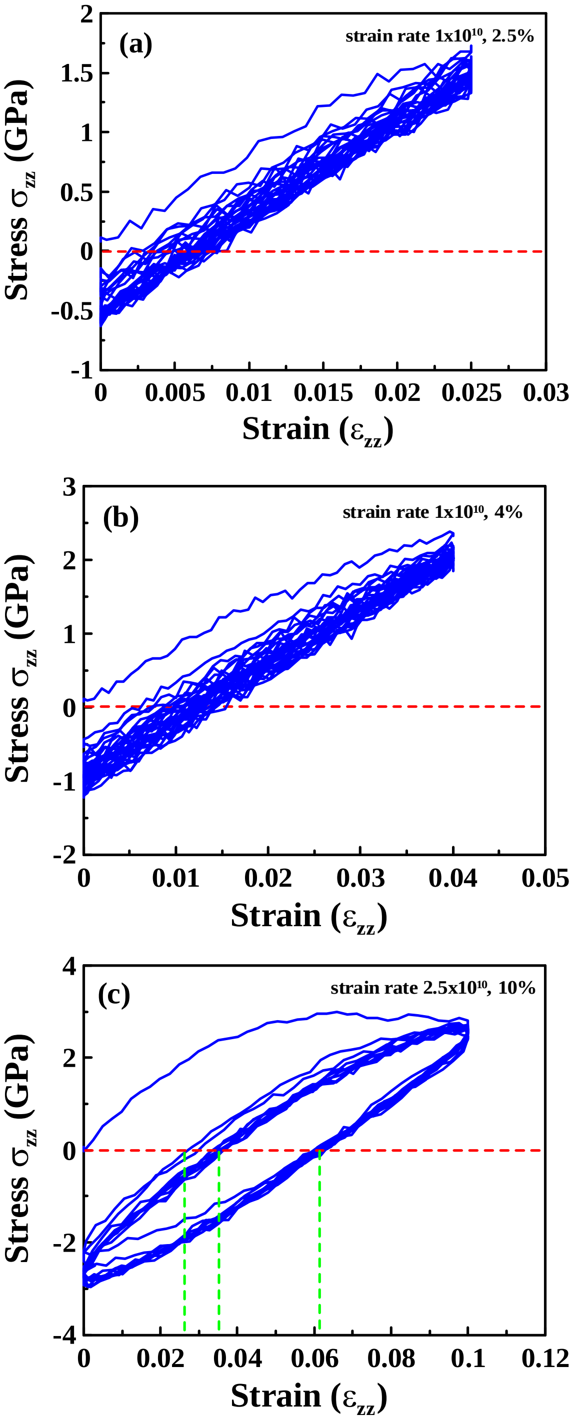

Fig. 5-54. The stress-strain curves for (a) 2.5%, (b) 4% (both nearly in elastic regime) and (c) 10% strain (highly plastic regime), respectively.

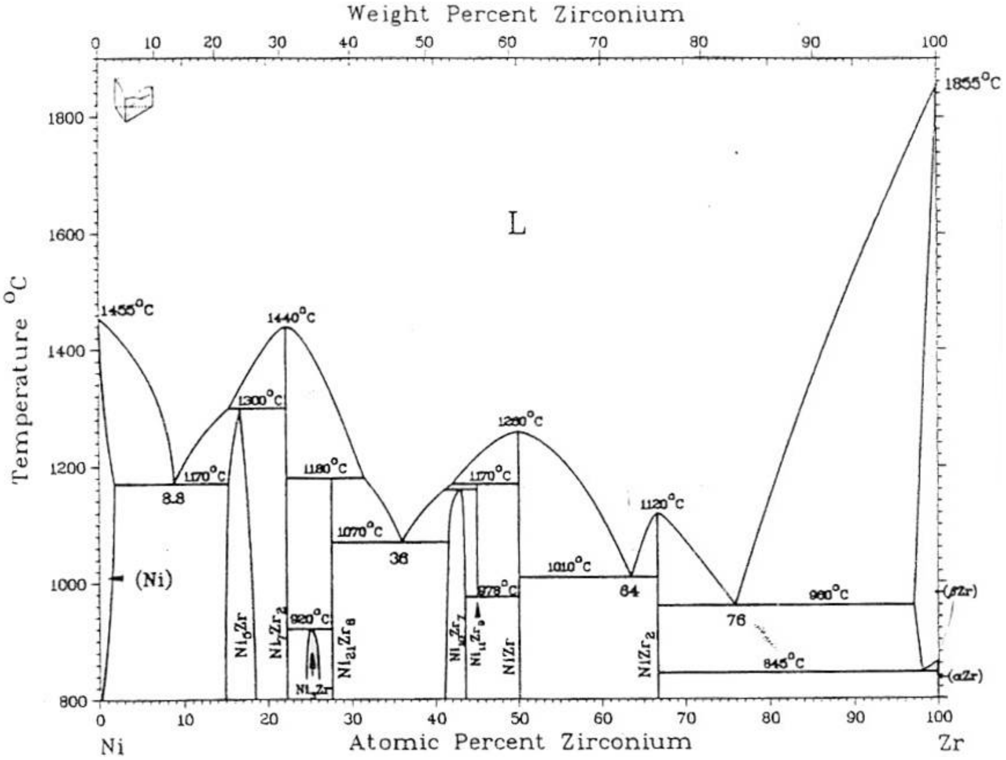

Fig. 6-1. Equilibrium phase diagram of Zr-Ni [180].

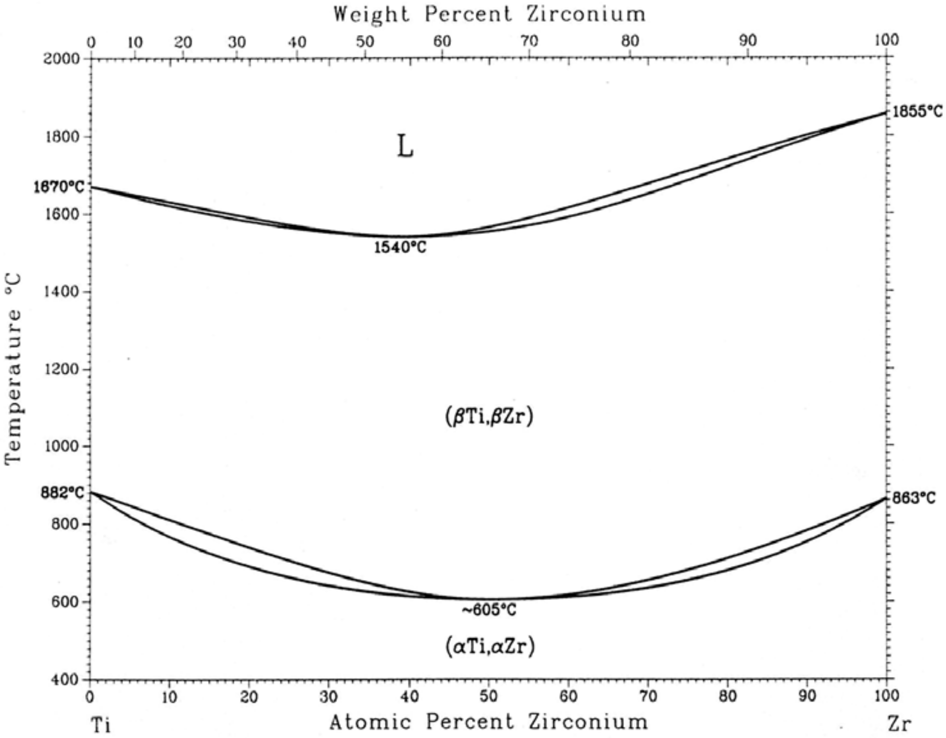

Fig. 6-2. Equilibrium phase diagram of Zr-Ti [181].

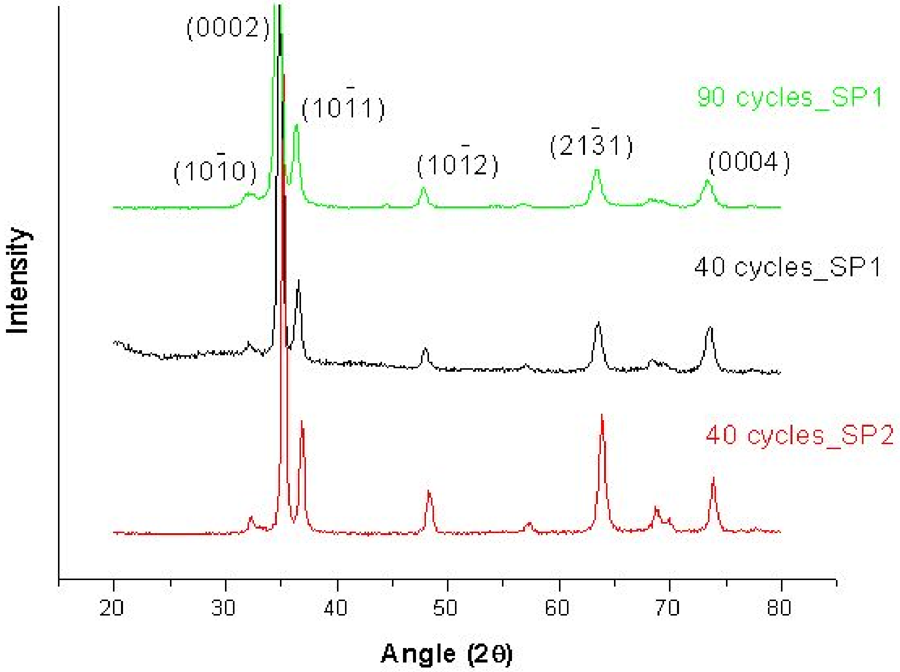

Fig. 6-3. XRD patterns of pure Zr specimen after different roll bonding cycles at room temperature.

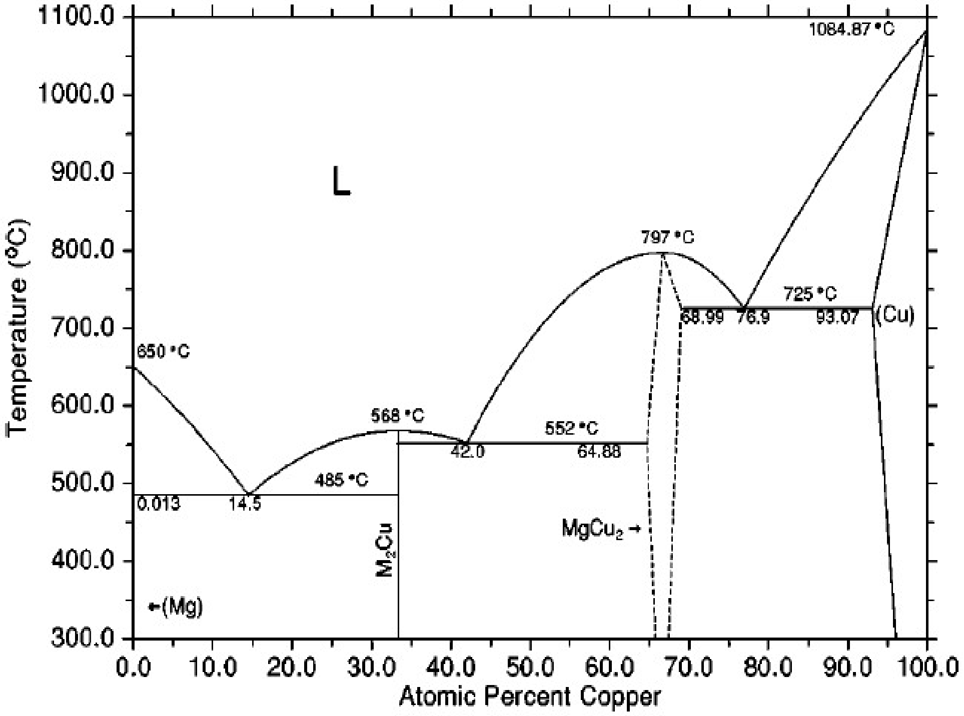

Fig. 6-4. Equilibrium phase diagram of Mg-Cu.

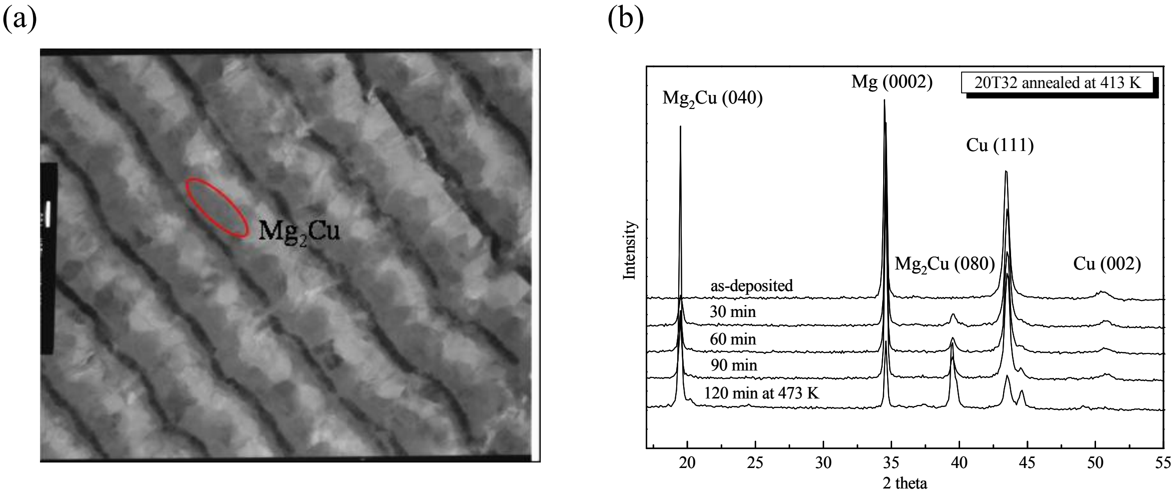

Fig. 6-5. (a) TEM image and (b) XRD pattern showing the structural transformation of the Mg-Cu multilayer system annealed at 413 K.

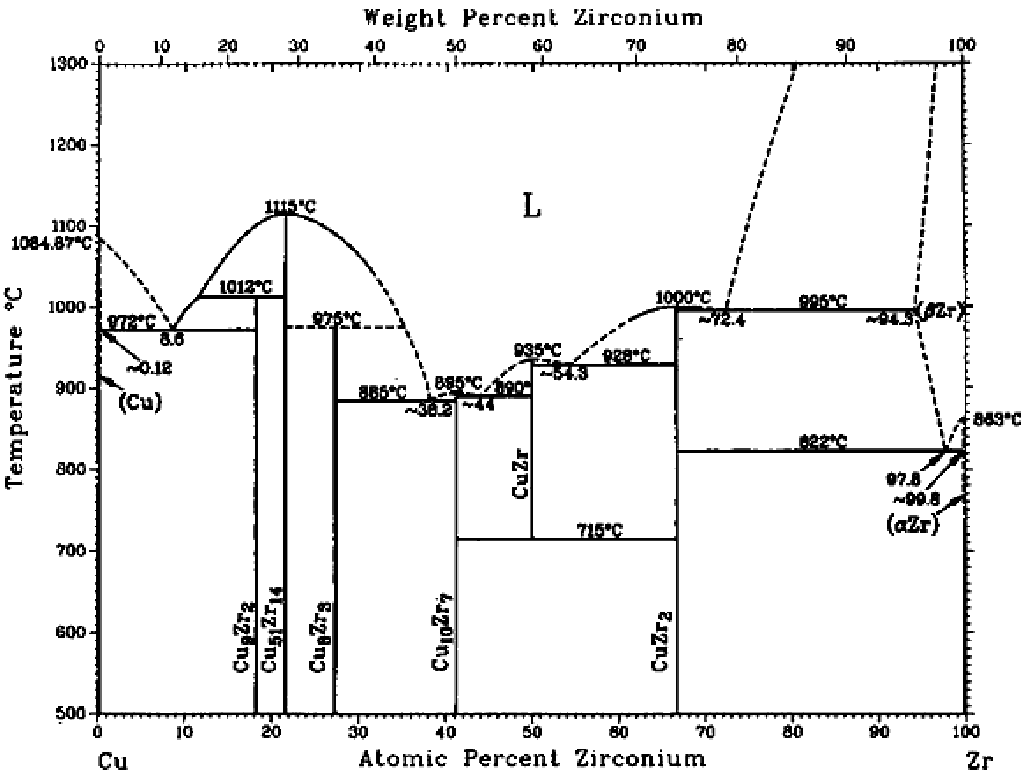

Fig. 6-6. Equilibrium phase diagram of Zr-Cu [186].

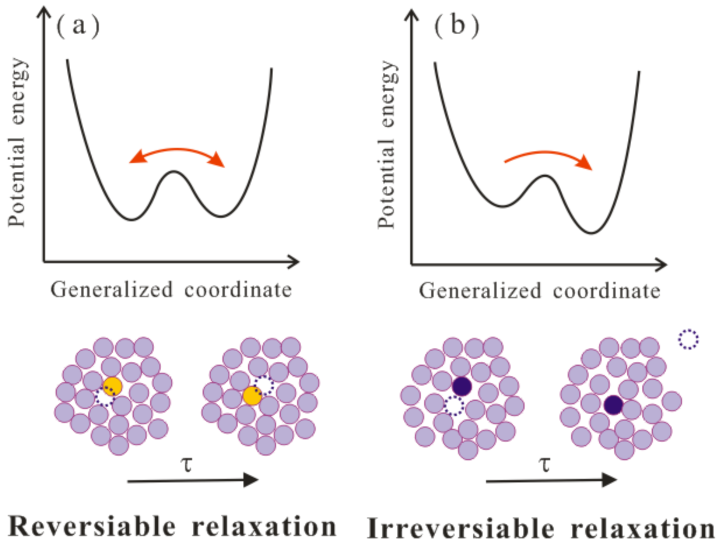

Fig. 6-7. The schematic drawings of metallic glass showing the models of dynamics recovery during cyclic loading: (a) the dynamic recovery model of reversible relaxation centers (RRCs) with a symmetry potential barrier which causes the local elastic events during the cyclic loading process, (b) the dynamic recovery model of irreversible relaxation centers (IRRCs) with an asymmetry potential barrier which causes the local plastic events during the cyclic loading process.

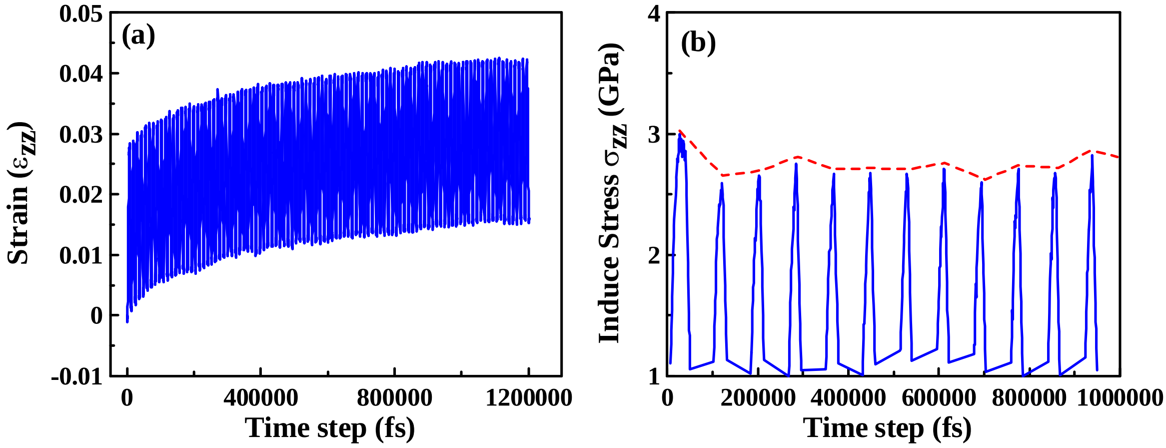

Fig. 6-8. Variation of (a) the induced strain as a function of the fatigue cycle for the stress-control mode at $\sigma_{max} = 2$ GPa, and (b) the induced stress as a function of fatigue cycle for the strain-control mode at $\varepsilon_{max} = 10\%$.